

NAVIER STOKES SOLUTION FOR
CHEMICAL LASER FLOWS:
STEADY AND UNSTEADY FLOWS

by
Ajay Prasannajit Kothari

Dissertation submitted to the Faculty of the Graduate School
of the University of Maryland in partial fulfillment
of the requirements for the degree of
Doctor of Philosophy
1979

COPY 1

APPROVAL SHEET

Title of Thesis: Navier Stokes Solutions for Chemical Laser Flows:
Steady and Unsteady Flows

Name of Candidate: Ajay Prasannajit Kothari
Doctor of Philosophy, 1979

Thesis and Abstract Approved: John D. Anderson, Jr.
Dr. John D. Anderson, Jr.
Professor and Chairman
Department of Aerospace Engineering

Date Approved: August 10, 1979

ABSTRACT

Title of Dissertation: Navier Stokes Solutions for Chemical Laser Flows:
Steady and Unsteady Flows

Ajay Prasannajit Kothari, Doctor of Philosophy, 1979

Dissertation directed by: John D. Anderson, Jr.
Professor and Chairman
Department of Aerospace Engineering

This work consists of an overall effort to apply a detailed and accurate computational fluid dynamic technique to the solution of practical high energy laser flows. In particular, a third generation of supersonic diffusion chemical laser analysis is introduced, namely, the complete solution of the Navier-Stokes equations for the laminar, supersonic mixing flow fields fully coupled with chemical kinetics for both the hot and cold reactions for HF. Multicomponent diffusion is treated in a detailed fashion.

Solutions are obtained, firstly, for "cold flows", where the effects of chemical reactions and vibrational relaxation are not included. Although such a situation is purely artificial, the results do isolate some of the fluid dynamic aspects of chemical laser flows, and provide a set of data to be compared later with hot flow calculations. A set of numerical experiments using four different time dependent finite difference schemes show that relatively minor changes in the differencing procedure can lead to major variations in the results. A modification of the well-known MacCormack approach appears to be the best suited for

mixing flows associated with chemical lasers.

A comparison is next made between cold flows and hot flows (with fully coupled chemical kinetics). The results show that temperature distributions are affected the most and velocity distributions the least by chemical energy heat release. The results have an impact on the interpretation of cold flow aerodynamic experiments in the laboratory, and their proper extrapolation to the real chemical laser flows. Also, comparisons between the present Navier Stokes results and other, more approximate, existing calculations are made. Gradients are calculated as a natural part of the Navier Stokes solutions. Results are given for steady flows with large pressure gradients where advantages of the Navier Stokes solutions are delineated.

In addition, the effect of unsteady fluctuations intentionally introduced at the cavity inlet are studied. Specifically, sinusoidal fluctuations in one stream and then both streams (primary and secondary) in various quantities e.g. pressure, density, u velocity and v velocity were simulated. Of these, the oscillations in v velocity with appropriate frequency and amplitude produced a remarkable improvement in mixing. Such unsteady fluctuations also yielded peak laser gain which were larger by almost a factor of two compared to the steady case.

The flow at the upstream boundary has so far, in the above mentioned cases been assumed to be uniform with real effects like Boundary Layer and Base Flow having been neglected. For comparison purposes these effects are next included.

A boundary layer profile in velocity at the inlet is shown to impede production of gain substantially. Base flow calculations were attempted but were not successful,

To My Uncle
Dr. Ramesh Patwa
And
To My Parents

ACKNOWLEDGMENTS

The author has received much help during his program towards his Ph.D., and is happy to have this opportunity to acknowledge the debts he has incurred.

The author's advisor, Dr. John D. Anderson, Jr., deserves a special space for gratitude. Dr. Anderson's attentive guidance, a keen perception of solutions to problems encountered and an unequivocal as well as immutable encouragement over these years elevates him to excellence which is difficult to equal, if not impossible to do so. His circumspectiveness in selecting problems of potential significance in the future is indeed highly valuable. In the author's opinion Dr. Anderson has achieved successfully the hard to obtain combination of excellent teaching talents and far reaching research competency not to mention excellent administrative capabilities. Frankly, without his gentle yet tenacious push much of the extent of this work might have remained at the horizon.

Just a simple thanks is not sufficient to acknowledge the help received from the author's co-advisor, Dr. Everett Jones, over the past years. It has been surely the author's good fortune to work under someone whose clear understanding of the basics of the problems is only compounded by his intellectual capacities to deal with them later. His unending friendliness has made for an easy access to both these talents for all around him. His early guidance in methodizing the attack of the problem and an almost continuous helping hand in later years is deeply appreciated.

The author would also like to take this opportunity to express his extreme appreciation to Dr. Walter Glowacki of the Naval Surface Weapons Center (at White Oak, MD) for his taking the trouble and time to run the LAMP code for the purposes of comparison between present results and an existing, proven program for chemical laser.

A major part of this work was supported by the Air Force Office of Scientific Research under Grant No. 74-2575 with Capt. Lloyd R. Lawrence as Project Manager and by the Office of Naval Research under contract N00014-77-C-0257 with Mr. Morton Cooper as contract monitor. The author would like to thank both Capt. Lawrence and Mr. Cooper for the encouraging ideas and views shown. Acknowledgment is also given to the Minta Martin Fund for Aeronautical Research, an endowment fund given to the College of Engineering by the late Glenn L. Martin. Support of the extensive computer time donated by the University of Maryland Computer Science Center is also gratefully acknowledged.

The author's colleagues and friends, Messrs. K. N. Parthasarathy, R. Diwakar, Mike Griffin and Suresh Babu deserve thanks for lending various opportunities for many fruitful discussions of associating problems as well as their constant companionship and friendship.

A special thanks also to Ms. Sue Osborn for her dilligent effort in doing an expeditious yet excellent job of typing the manuscript; and to Peter Cheung for the fine drawings found in this dissertation.

TABLE OF CONTENTS

<u>CHAPTER</u>	<u>PAGE</u>
Dedication	ii
Acknowledgment	iii
List of Symbols	viii
List of Tables	xi
List of Figures	xii
I. INTRODUCTION	1
1.1 Some Background Information	1
1.2 Scope and Purpose of Present Work	4
1.2.1 Cold Flow (Steady)	5
1.2.2 Modified MacCormack Method	5
1.2.3 Hot Flow (Steady)	6
1.2.4 Unsteady Flow	7
II. OVERVIEW OF THE PROBLEM	9
2.1 Physical - Layout of the Nozzles	9
2.1.1 Two Dimensionality	9
2.1.2 Boundary Conditions	9
2.2 Chemical - Mechanism for Population Inversion	10
III. FORMULATION OF THE PROBLEM	12
3.1 Governing Equations	12
3.2 Calculation of Related Quantities	21
3.2.1 Calculation of h_k , E and H	21
3.2.2 Calculation of Species and Mixture Transport Properties	23
3.2.2a Viscosity	23
3.2.2b Thermal Conductivity	24

	<u>PAGE</u>
3.2.2c Diffusion Coefficients	25
3.2.3 Calculation of Chemical Production Term \dot{w}_i	27
IV. GAIN	30
V. THE NUMERICAL METHOD	37
5.1 The Time Dependent Approach	37
5.2 Differencing Scheme	38
5.3 Time Step	40
5.3.1 Fluid Dynamic Criteria	40
5.3.2 Chemical Kinetic Criteria	41
5.4 Grid Size and Convergence	41
VI. COLD FLOW	43
6.1 Inlet Conditions	43
6.2 Results and Discussion	44
6.3 Computational Experiments	45
6.3.1 Variation in Grid Size	45
6.3.2 Effect of a Continuous Velocity Profile	45
VII. HOT FLOW	47
7.1 Weakly Reacting Case	47
7.1.1 Inlet Conditions	47
7.1.2 Results and Discussion	47
7.2 Strongly Reacting Case	50
7.2.1 Inlet Conditions	50
7.2.2 Results and Discussion	50
7.3 Test Case with Higher Cavity Pressure	52
7.3.1 Inlet Conditions	52
7.3.2 Results and Discussion	52

	<u>PAGE</u>
VIII. UNSTEADY FLOW	55
8.1 Weakly Reacting Case	55
8.1.1 Inlet Conditions	55
8.1.2 Results and Discussion	56
8.1.2a Pressure	56
8.1.2b u Velocity	57
8.1.2c v Velocity	59
(I) Fluctuations in One Stream - F ₂ Stream	59
(II) Fluctuations in Both Streams	61
8.2 Test Case with Higher Cavity Pressure	61
8.2.1 Inlet Conditions	61
8.2.2 Results and Discussions	61
IX. MISCELLANEOUS EXPERIMENTS	64
9.1 Boundary Layer in Velocity	64
9.2 Base Flow	64
X. CONCLUSIONS AND RECOMMENDATIONS	67
Appendix A	70
Appendix B	83
References	88
Tables	93
Figures	98

LIST OF SYMBOLS

$B_{\ell \rightarrow u}$	Einstein absorption coefficient
c	speed of light
C_i	mass fraction of species i
C_p	specific heat for constant pressure
C_v	specific heat for constant volume
D_{ij}	binary diffusion coefficient ($D_{ij} = D_{ji}$)
D_{im}	multicomponent diffusion coefficient for species i
E	total internal energy of the mixture
$E(v, J)$	vibrational-rotational energy of level (v, J)
e	internal energy of the mixture
e_k	internal energy of the species k
$\text{erf}(n)$	error function
$F_{v, J}$	vibrational-rotational interaction parameter ≈ 1
G_0	small signal gain coefficient
$G_{0 \text{ av.}}$	averaged small-signal gain coefficient
g_ℓ, g_u	degeneracies of lower and upper vibrational levels respectively
H	total enthalpy of the mixture
h	width of the nozzle section; Planck's constant in Chapter 4 except in Eq. (55) where h is again width of the nozzle section
h_k	enthalpy of species k
I_ν	intensity of the radiation at frequency ν
J	rotational quantum number

k	thermal conductivity of the mixture; Boltzmann constant in Eq. (25) and in Chapter 4
M	molecular weight
N_A	Avogadro's number
N_l, N_u	number densities by lower and upper vibrational levels respectively
p	pressure
$Q(v)$	vibrational partitional function for level v
R	specific gas constant
\bar{R}	universal gas constant
$ R_v^{v+1} ^2$	vibrational contribution to the electric dipole moment
T	temperature
t	independent time coordinate
$\bar{U}, \bar{F}, \bar{G}, \bar{K}$	column matrices based on flow properties
u	x component of the velocity vector
U_r	reference velocity
v	y component of the velocity vector
$V(\eta)$	Voigt function
x, y	independent spatial coordinates
$\dot{\omega}_i$	species production term due to chemical reactions
$[i]$	concentration of species i

Greek Symbols

ϵ	characteristic energy of interaction between a pair of molecules
λ	species thermal conductivity

μ	mixture viscosity
η	species viscosity
ν	frequency of the radiation
ν_{kx}	x component of diffusion velocity for species k
ν_{ky}	y component of diffusion velocity for species k
ρ	density of the mixture
ρ_k	density of species k
σ	collision cross-section of molecules, \AA^2
τ	chemical relaxation time
$\phi_{C,D}$	line profile parameter - centerline value for Doppler line broadening
ω	angular velocity of the fluctuation

LIST OF TABLES

Table		Page
I	Wavelength of radiation for various P transitions	93
II	Molecular properties of various species	94
III	Rate coefficients for $H_2 - F_2$ chemical laser	95
IV	Mass conservation in flow-wise direction	97

LIST OF FIGURES

<u>Figure</u>		<u>Page</u>
1	Nozzle configuration and initial conditions	98
2	Population inversion-mechanism for laser action	99
3	Slab of gas emitting or absorbing radiation	100
4	Plot of a line shape function	100
5	Convergence behavior of the solution for various grids	101
6	Velocity profiles at various x locations for 13 x 13 grid size	102
7	Pressure profiles at $x/h = 0, 5$ and 10 for 13 x 13 grid	103
8	Temperature profiles at $x/h = 0, 5$ and 10 for 13 x 13 grid	103
9	Specific density profiles for F_2 at various x locations for 13 x 13 grid size	104
10	Specific density profiles for F at various x locations for 13 x 13 grid size	104
11	Specific density profiles for H_2 at various x locations for 13 x 13 grid size	105
12	Specific density profiles for H_e at various x locations for 13 x 13 grid size	105
13	Velocity profiles for various grids	106
14	Pressure profiles for various grids	107
15	Temperature profiles for various grids	108

<u>Figure</u>		<u>Page</u>
16	Specific density profiles for F_2	109
17	Specific density profiles for F	109
18	Comparisons of continuous and discontinuous velocity profiles at upstream boundary- -pressure @ $x/h = 10.0$ and $y/h = 0.5$ plotted versus time	110
19	Nozzle configuration and initial conditions - weakly reacting case	111
20	Plot of temperature versus time at $x/h = 10.0$, $y/h = 0.375$.	112
21	Velocity profiles at various x-wise locations	113
22	Steady state pressure profiles at various x-wise locations	114
23	Steady state temperature profiles at various x-wise locations	115
24	Density profiles for various HF vibrational levels at $x/h = 5.0$	116
25	Density profiles for various HF vibrational levels at $x/h = 10.0$	117
26	Growth of the reaction zone; comparison of present calculations with experiment	118
27	Plot of x-wise variation of populations of various HF vibrational levels	119
28	Variation of small signal gain in flow direction; 1-0 transition, $y/h = 0.375$	120

<u>Figure</u>		<u>Page</u>
29	Variation of small signal gain in flow direction; 2-1 transition, $y/h = 0.375$	121
30	Nozzle configuration and initial conditions - strongly reacting case	122
31	Pressure versus longitudinal distance; comparison between present results and methods of Refs. 20 and 29 - strongly reacting case	123
32	Temperature versus longitudinal distance; comparison between present results and methods of Refs. 20 and 29 - strongly reacting case	124
33	HF(0) density versus longitudinal distance; comparison between present results and methods of Refs. 20 and 29 - strongly reacting case	125
34	HF(0) and temperature profiles; comparison between present results and methods of Ref. 29 - weakly reacting case	126
35	Flow configuration and initial conditions - case with higher cavity pressure	127
36	Pressure surface; note different viewing angle	128
37	Temperature surface; note different viewing angle	129
38a	Global density surface	130
38b	u velocity surface	131
39	Species density - F_2	132
40	Species density - H_2	133

<u>Figure</u>	<u>Page</u>
41	134
Species density - H_2 . Note different viewing angle - $\theta = 60^\circ$ and $\phi = 150^\circ$	
42	135
HF(0) density surface	
43	136
HF(1) density surface	
44	137
HF(2) density surface	
45	138
Comparison plot of averaged small signal gains between steady and unsteady cases: 1 - 0 transitions	
46	139
Comparison plot of averaged small signal gains between steady and unsteady cases: 2 - 1 transitions	
47	140
Plot for sinusoidal variation in a variable and frequency calculation according to F_2 nozzle height	
48	141
Time wise plot for fluctuations in u velocity in F_2 stream	
49	142
Time wise plot for fluctuations in u velocity in F_2 stream	
50	143
Density and pressure at various phase angles	
51	144
Variations of species density in flow direction - comparison of steady and unsteady cases	
52	145
Density profiles for various HF vibrational levels	
53	146
Plot of x-wise variation of populations of various HF levels @ $y/h = 0.375$	

<u>Figure</u>		<u>Page</u>
54	Velocity vector diagram	147
55	F_2 density variation @ $x/h = 10.0$ and $y/h = 0.375$ for sinusoidal fluctuations in v velocity	148
56	Comparison plot of averaged small signal gains for steady and unsteady cases: 1 - 0 transition	149
57	Comparison plot of averaged small signal gains for steady and unsteady cases: 2 - 1 transition	150
58	Pathlines of inert particles inserted at inlet after repeatitive state is reached	151
59	Fluctuations in v velocity in both streams - a timewise plot for F_2 density @ $x.h = 10.0$ and $y/h = 0.375$	152
60 (a)&(b)	Pressure surfaces for unsteady flow with v velocity fluctuations at different phase angles δ	153
60 (c)&(d)	Temperature surfaces for unsteady flow with v velocity fluctuations at different phase angles δ	153
61 (a)&(b)	u velocity surfaces - plots at different phase angles δ of fluctuations	154
61 (c)&(d)	v velocity surfaces - plots at different phase angles δ of fluctuations	154

<u>Figure</u>		<u>Page</u>
62	HF(0) density surface at the instant described by phase angle $\delta = 0^{\circ}$	155
63 (a)&(b)	HF(1) density surfaces at different phase angles	156
63 (c)&(d)	HF(2) density surfaces at different phase angles	156
64	HF(1) density surface for $\delta = 180^{\circ}$ as seen from a different viewing angle - $\theta = 60^{\circ}$ and $\phi = 150^{\circ}$	157
65	Boundary layer profile (velocity)	158
66	Averaged small signal gain - a comparison plot	159
67	Description of the base region and some inlet profiles used	160
B-1	Plot of pressure versus time at $x/h = 10.0$ and $y/h = 0.5$	161
B-2	Plot of velocity at $x/h = 10.0$	162
B-3	Specific density profiles at $x/h = 10.0$	163
B-4	Steady state pressure profiles at $x/h = 10.0$	164

CHAPTER I

INTRODUCTION

1.1 SOME BACKGROUND INFORMATION

The past decade has initiated the age of high energy lasers; first starting in 1966 with gas-dynamic lasers and closely followed by breakthroughs in large chemical and electric discharge lasers. The gasdynamic laser, which generates its laser medium by means of a vibrational non-equilibrium nozzle expansion, is the subject of a recent book by Anderson¹ and papers by Glowacki et al² and Russel³. The electric-discharge laser, which generates its laser gas via electron-atom and/or molecule collisions in a glow discharge, has been reviewed by Reilly⁴. The supersonic diffusion chemical laser, which obtains a laser medium from the products of chemical reaction is nicely described in a review of Warren⁵. A thorough discussion of such continuous wave (cw) as well as pulsed chemical laser is also presented in a book by Gross and Bott⁶ called "Chemical Laser Handbook". This volume collects and critically reviews all available literature and the entire body of research work in chemical lasers which was published and performed between 1967 and 1974. All of the above lasers involve high speed flow of large amounts of gas; hence, they all involve the realms of aerodynamics and gasdynamics. (For example the HF or DF supersonic diffusion chemical laser involves the supersonic mixing of two dissimilar streams, as shown in Fig. 1).

Concurrently, the discipline of computational fluid dynamics has become a third-dimension in aerodynamics, complementing both laboratory experiments and pure analysis⁷⁻⁹. Work is advancing on both numerical methods and applications to practical engineering problems. The present

work is in the latter vein. Specifically it deals with the direct application of computational fluid dynamics to the solution of chemical laser flows.

The present work represents a new third generation of supersonic diffusion chemical laser analyses. First generation studies are exemplified by the RESALE computer program¹⁰ (which assumes one dimensional premixed flow) and the approximate flame-sheet model of Hofland and Mirels^{11,12}. In the flame sheet modeling the reaction zone is confined to the boundary of the region described by a parabola. The chemical pumping reactions, thus are assumed to take place in an infinitesimally thin region. In reality it takes a small but finite time for these reactions to occur and hence the actual pumping region has a finite thickness, and the regions of pumping and V - V, V - T deactivations overlap each other. Calculations of these regions require much more detailed formulations. Nevertheless such approximate modelings as flame sheet modeling have served a very important purpose in beginning the interim first-generation studies.

Second generation studies involve more detailed fluid dynamic calculations, such as the boundary layer solutions of King and Mirels¹³ and of Tripodi et al¹⁴. Unfortunately, none of these solutions are able to model and solve the complicated chemically reacting, recirculating and separated flow regions at the base of chemical-laser nozzles- an important aspect that affects chemical-laser performance as emphasized by Grohs¹⁵.

In King and Mirels report the streams of H₂ and F are assumed to be semi-infinite and hence pressure in the flow direction is assumed constant, being the same as the pressure outside the boundary layer i.e.

inside the inviscid core. In reality, in a chemical laser a large number of nozzles are stacked together side by side. Thus the H_2 and F streams are not semi-infinite but rather of a finite width. Assumption of constant pressure in the flow direction is hence invalid and, rather, some way of calculating the flow-wise pressure increase is absolutely necessary.

Therefore, the present investigation is the beginning of a third generation of studies, which incorporates the solution of the complete Navier Stokes equations¹⁶⁻¹⁹ for chemical-laser flows. The advantage of invoking the Navier Stokes equations is that such complicated separated flow fields as well as any lateral or longitudinal pressure gradients induced by the chemical heat release are modeled exactly. The apparent disadvantage is that numerical solutions of Navier Stokes solutions take long computer times. However, this can be reduced considerably per run, if, while doing parametric studies, the runs are made back to back and the final steady state of one run is used as the initial condition for the other run with slightly different inlet conditions.

From among the other existing chemical laser solutions one of the most versatile is the LAMP (Laser and Mixing Program) developed at Lockheed (at Huntsville, Alabama). The formulation assumes parallel mixing and constant lateral pressure with lasing due to single or multiple transitions. The program allows any chemical or vibrational reaction mechanism and associated rate constants to be prescribed as input data as long as thermodynamic properties are also available for all participating species. Transport properties are accounted for in terms of constant Prandtl and Lewis numbers in conjunction with a variety of viscosity options which include models for both laminar and turbulent flow. The set of parabolic partial differential equations which describes

the problem is integrated via application of a finite-difference technique. The output of the computer program gives detailed axial and lateral distributions of velocity, temperature, density, species mole fractions, laser transition gains and radiative intensities, and laser power output.

Of the other existing CL codes, BLAZE-II also deserves more than a mention. Two dimensional mixing and reacting flow analysis usually does not come cheaply in terms of computer time. And so, in it, a compromise between one- and two-dimensional treatments of the lasing problem was made by simplifying the multidimensional equations using boundary-layer integral methods. This approach also allows the nozzle boundary-layer influence to be considered.

1.2 SCOPE AND PURPOSE OF PRESENT WORK

The present work is part of a larger, overall research effort to apply detailed computational fluid dynamic techniques to the analysis of practical problems of gasdynamic and chemical lasers. In particular, Jones and Anderson²² have developed a time-dependent numerical solution of the complete Navier Stokes equations as applied to the supersonic laminar and turbulent mixing flows characteristic of downstream mixing gasdynamic lasers and supersonic diffusion chemical lasers. The numerical technique and sample solutions for non-reacting and non-relaxing mixing flows of air-into-air are given in detail in Ref. 22. This work extended in a very fine fashion as applied to the case of Downstream mixing Gasdynamic laser is described in detail by Parthasarathy et al²³.

In the present work, the basic approach of Ref. 22 is extended to chemical laser flows. Specifically, the complete Navier Stokes equations

are used to calculate the supersonic laminar mixing of two chemically reacting streams, one of Fluorine and the other of Hydrogen. As usual, Helium is used as a diluent in both the streams, to different extents. Multicomponent diffusion is treated in a detailed fashion.

1.2.1 Cold Flow (Steady)

The results are obtained, firstly, for the cold flows only, i.e., the chemical reactions and vibrational energy exchanges are assumed frozen. Obviously this is purely an artificial situation, contrary to nature, because H_2 and F_2 , being hypergolic, will automatically react when brought into physical contact with each other. However, the "switching off" of the kinetics has two purposes:

(1) To examine the purely fluid dynamic aspects of such flows with multicomponent diffusion. In this fashion, a set of cold flow calculations are produced which, when compared with similar calculations for hot flows (flows with chemical reaction and vibrational relaxation), will allow a direct qualitative and quantitative isolation of the effect of reactions on the fluid dynamics. This type of comparison should provide information on how results from cold flow laboratory experiments can be extrapolated to actual chemical laser performance.

(2) To simply provide an interim assessment without further complications due to chemical kinetic effects. In other words to serve as a first step towards the eventual solution of the entire problem.

1.2.2 Modified MacCormack Method

There was another major purpose served at this point which is fundamental to the aspects of computational fluid dynamics. Four numerical difference schemes with seemingly minor variations between them were found to produce major differences in the behavior of the solutions.

The Appendix B describes a series of numerical experiments which delineate these differences, and which help to identify one particular difference scheme which appears most suited for the analysis of viscous mixing flows characteristic of chemical lasers. This particular differencing scheme was termed the Modified MacCormack method.

1.2.3 Hot Flow (Steady)

A time dependent explicit finite difference scheme due to MacCormack²⁴ is employed. The Navier Stokes equations are used in order to develop an analysis valid for chemical laser flows taking into account possible large transverse and longitudinal pressure gradients in the reaction region caused by the heat release, as well as allowing for the possibility of separated and/or reverse flow in the base region of the nozzle bank. The boundary layer equations are not valid in such cases. A time dependent solution for the steady flow is employed, because such an approach is advantageous for solutions of mixed subsonic and supersonic flow fields which may be of interest. In this sense, a time-dependent finite difference solution of the Navier Stokes equations represents the "state-of-the-art" in computational fluid dynamics, and eventually leads to the best possible, most detailed calculations of chemical laser performance with minimum amount of modeling involved.

It was in this light, to assess the viability of Navier Stokes solutions for chemical laser flows, and to underscore the advantages as well as the present-day restrictions of such numerical solutions, that this work is done. The full chemical-laser kinetics, including both the cold and hot reactions for HF are now coupled with the Navier Stokes equations, and the numerical results are obtained for the detailed variations of velocity, pressure, temperature, chemical species

concentrations, and HF vibrational populations throughout the region shown in Fig. 1. Steady state values are approached asymptotically at large times. Small signal and integrated gain are also calculated from the steady state values already obtained now for the entire region of interest.

Further to illustrate graphically the effect of chemical heat release on the fluid dynamics of the adiabatic flow (cold flow), a comparison is made between the results obtained before and after the kinetics are switched on i.e. between cold and hot flows. Such considerations are important when extrapolating nonreacting supersonic mixing results obtained in the laboratory to the case of real chemical lasers.

During the course of the present investigation it was brought to the author's attention that Navier Stokes solutions are also being carried out by Butler et al at the Los Alamos Scientific laboratory²⁵⁻²⁷. Using the hydrodynamic code RICE,²⁷ various calculations involving principally DF chemical lasers with base relief nozzles have been made. This work to date has generally been unpublished. Because the present work deals with HF chemical lasers with purely tangential mixing, direct comparison with the Los Alamos work cannot be made. Instead, the present results are compared with the finite difference boundary layer solutions of the LAMP code^{20,28} and of King and Mirels²⁹. However the Los Alamos calculations and the present work both demonstrate the feasibility of Navier Stokes solutions for chemical lasers -- an important conclusion to help guide future analyses.

1.2.4 Unsteady Flow

So far the time dependent method has been used to calculate steady state chemical laser flow fields as the asymptotic result at large times;

the final steady state has been the desired result, and the time-dependent technique has been simply a means to that end¹⁶⁻¹⁸. A question now can be asked: what would be the effect of intentionally introduced fluctuations at the inlet on the overall performance of the chemical laser? The answer to this question was observed to be a real enhancement of mixing and increase in gain for some particular fluctuations at the inlet. Availability of the already existing time dependent technique was taken advantage of to study the transient effects of unsteady fluctuations in the flow properties at the cavity inlet on overall chemical laser performance downstream. In particular, the results show that intentional fluctuations in the inlet velocity vector can result in increased mixing and about a factor of two increase in HF chemical laser gain. This work presents the final results of such unsteady mixing phenomena in chemical lasers.

CHAPTER II

OVERVIEW OF THE PROBLEM

2.1 PHYSICAL: LAYOUT OF THE NOZZLES

2.1.1 Two Dimensionality

The axis y shown in Fig. 1 is the laser beam direction. Axis z is then perpendicular to the plane of the paper and $\partial/\partial z \equiv 0$ reducing the problem to a two dimensional one. Also in the beginning, for the steady flow calculations, parallel mixing is assumed for the following reasons:

- (a) it constitutes a reasonably straight forward test of the present Navier Stokes solutions;
- (b) other results exist for this model and hence can be used for comparison; and,
- (c) it is a relatively uncomplicated model to compare results for hot and cold flows.

2.1.2 Boundary Conditions

As already mentioned earlier the nozzles of chemical lasers are stacked together side by side, Hydrogen and Flourine nozzles placed alternatively. Supersonic flow of the fuel gas viz. Hydrogen and the oxydizer gas viz. Flourine issues from the nozzle exits. If, now we looked at the centerlines of any of the nozzles, it would be obvious that the properties on both sides of the centerlines are mirror images of each other. Thus symmetry conditions exist about the centerlines. Calculations, then, need to be made only in the section of the flow region enclosed between two adjoining centerlines, one of a Hydrogen stream and other of the adjoining Flourine stream, in order to know the properties at each point in the entire lasing region. Symmetry conditions

thus describe the natural boundary conditions on two sides of the region of computation. The boundary conditions at the upstream end of the test section (the region of computation will now be referred to as the 'test section') are also prescribed, being the same as the nozzle exit conditions. These conditions were so chosen as to represent a possible experimental situation. The conditions at the downstream end of the test section need not be prescribed.

2.2 CHEMICAL MECHANISMS FOR POPULATION INVERSION

As discussed earlier, the Fluorine and Hydrogen nozzles, appropriately diluted with Helium are stacked together alternatively. These supersonic streams when brought into contact with each other, react hypergolically in the mixing region downstream of the nozzle exits. In particular the following two reactions called the "pumping reactions" take place, designated respectively as the cold and hot reactions.



The cold reaction can populate HF in the vibrational levels 0, 1, 2 and 3; whereas the hot reaction can populate higher vibrational levels such as 0 through 8. Each one of these HF vibrational levels, from 0 through 8, can be and is treated as a separate species interlinked by chemical reactions and vibrational relaxation reactions.

These pumping reactions have a characteristic of producing vibrationally excited HF viz. $HF(v)^*$ wherein the populations of various

vibrational levels do not follow the Boltzman distribution for the local translational temperature. Population inversion is then said to exist if population of a higher level is greater than that of the lower level i.e. if $N_{\text{HF}(v+1)} > N_{\text{HF}(v)}$. An example of this is depicted in Fig. 2 along with the corresponding Boltzman distribution. It is this population inversion that makes the laser work (see Refs. 1 and 30 for background on laser properties). The vibrationally excited HF molecules give off their energy in excess of that prescribed by the Boltzman distribution and this energy is given off in the form of electromagnetic radiation. The energy differential between the HF vibrational levels up to about nine levels being approximately same, the frequency of the radiation²⁶ turns out to be approximately the same viz. 2.7 μ and thus the radiation is nearly coherent (see Table I for reference) chemical energy is thus available in the form of radiation energy through the mechanism of population inversion. In the chemical laser, this inversion may be total, as previously described, or partial, where the inversion is carried by the rotational distribution^{1,31}. Rotational levels are here assumed to be in equilibrium at the translational temperature.

CHAPTER III
FORMULATION OF THE PROBLEM

3.1 GOVERNING EQUATIONS

As already discussed earlier in the previous chapter, the flow in the test section region is two dimensional. The small characteristic sizes of the chemical laser, as well as small representative densities, render the characteristic Reynolds number of the order of 10^3 . Thus viscosity plays an important role in the flow region. The flow then is fully viscous as well as compressible. The two dimensional Navier Stokes equations are therefore used. Mass diffusion, thermal conduction and viscous dissipation are also incorporated. Diffusion due to pressure (Dufoure effect) and temperature gradients³² is negligible and hence is not included.

As mentioned earlier, the hot reaction is able to pump 0 through 8 vibrational levels of HF. Each one of these vibrational levels is treated as a separate species. Adding to these 9 species, the reactants H, H₂, F, F₂ and an inert gas (diluent) He make a total of 14 different species leading to the 14 species continuity equations.

These 14 species continuity equations in addition to (1) the global continuity equation, (2) x momentum equation, (3) y momentum equation and (4) energy equation make a system of 18 equations which are used to solve for the 18 unknowns. These unknowns are (1) mass density - ρ , (2) x component of velocity - u, (3) y component of velocity - v, (4) temperature - T and (5).....(18) species densities - ρ_k where $k = 1, 2, \dots, 14$. Pressure was obtained using the equation of state since the density and temperature would be calculated and the specific gas

constant R for the mixture of gas at any point can also be calculated.* Thus all the thermodynamic properties of flowing gas mixture can be calculated at every point.

The 14th species continuity equation is redundant since $\sum_{k=1}^{14} \rho_k = \rho$ where ρ is being calculated independently using the global continuity equation. Nevertheless all 14 of the species continuity equations were used since it was not apparent beforehand which species density should best be calculated as

$$\rho_n = \rho - \left[\sum_{k=1}^{n-1} \rho_k + \sum_{k=n+1}^{14} \rho_k \right] \quad (3)$$

rather than by the species continuity equation for ρ_n .

This approach, nevertheless, does not necessarily render the problem inconsistent unless a mistake exists somewhere within the program. It instead serves as a good check for the program making it more sensitive. Aposteriori the values of global densities obtained in both these ways (viz. $\rho = \sum_{k=1}^{14} \rho_k$ where ρ_k is calculated from species continuity equation and ρ as computed from the global continuity equation) were compared and were found to be in an excellent agreement.

In order to calculate the transport properties of the gas mixture at any point (viz. viscosity, thermal conductivity and diffusion coefficients), the transport properties of each of the constituent gases were

* Mass fractions c_i of each constituent gas i.e. ρ_i/ρ making up the mixture at any point as well as molecular weights of each component species are also known. From these, the specific gas constant can be calculated as,

$$R = \sum_{i=1}^{18} c_i R_i = \sum_{i=1}^{18} c_i \frac{R}{m_i}$$

calculated first, from various formulae available for individual species viscosity, thermal conductivity and binary diffusion coefficients. Once these are known, the mixture viscosity, thermal conductivity and multicomponent diffusion coefficients can readily be calculated as the constituents and their mass fractions are also known at each mesh point. A more detailed analysis of the calculation of these transport properties is presented elsewhere in this chapter.

The afore mentioned equations, for the case of two dimensional unsteady flow, in their dimensional form³³ are written below. They are,

Continuity:

$$\frac{\partial \rho}{\partial t} + \frac{\partial}{\partial x} (\rho u) + \frac{\partial}{\partial y} (\rho v) = 0 \quad (4)$$

x-Momentum:

$$\rho \frac{Du}{Dt} = - \frac{\partial p}{\partial x} + \frac{\partial}{\partial x} (\sigma_x) + \frac{\partial}{\partial y} (\tau_{yx}) \quad (5)$$

where σ_x is deviatoric normal stress and τ_{yx} is shearing stress.

$$\sigma_x = - 2/3 \mu \left(\frac{\partial u}{\partial x} + \frac{\partial v}{\partial y} \right) + 2 \mu \frac{\partial u}{\partial x}$$

$$\tau_{yx} = \mu \left(\frac{\partial v}{\partial x} + \frac{\partial u}{\partial y} \right)$$

y-Momentum:

$$\rho \frac{Dv}{Dt} = - \frac{\partial p}{\partial y} + \frac{\partial}{\partial x} (\tau_{xy}) + \frac{\partial}{\partial y} (\sigma_y) \quad (6)$$

again here σ_y is deviatoric normal stress and τ_{xy} is shearing stress.

$$\tau_{xy} = \mu \left(\frac{\partial v}{\partial x} + \frac{\partial u}{\partial y} \right) = \tau_{yx}$$

and,

$$\sigma_y = -2/3 \mu \left(\frac{\partial v}{\partial y} + \frac{\partial u}{\partial x} \right) + 2 \mu \left(\frac{\partial v}{\partial y} \right)$$

In both the above equations the body forces are neglected and bulk viscosity K is assumed to be negligible.

Energy:

$$\rho \frac{DE}{Dt} = -\nabla \cdot \dot{\bar{q}} - \nabla \cdot (p \bar{V}) \quad (7)$$

where,

$$\text{total energy } E = e + \frac{V^2}{2}$$

and $\dot{\bar{q}}$ is the heat flux vector including in general conduction, diffusion and radiation.

$$\dot{\bar{q}} = (\dot{\bar{q}}_c + \dot{\bar{q}}_d + \dot{\bar{q}}_r)$$

Species Continuity:

$$\frac{\partial \rho_k}{\partial t} + \frac{\partial}{\partial x} [\rho_k (u + v_{kx})] + \frac{\partial}{\partial y} [\rho_k (v + v_{ky})] = \dot{\omega}_k \quad (8)$$

where v_{kx} and v_{ky} are x and y components of the diffusion velocity for the species k and $\dot{\omega}_k$ is the rate of chemical production of the species k.

The subscripts 1 through 14 correspond to the various species as given in Table II.

On further simplification, after some algebraic manipulation, these equations can be reduced to the following form; the well known conservation form:

$$\frac{\partial \rho}{\partial t} + \frac{\partial}{\partial x} (\rho u) + \frac{\partial}{\partial y} (\rho v) = 0 \quad (9)$$

$$\begin{aligned} \frac{\partial}{\partial t} (\rho u) + \frac{\partial}{\partial x} [\rho u^2 + p + \frac{2}{3} \mu (\frac{\partial u}{\partial x} + \frac{\partial v}{\partial y}) - 2 \mu \frac{\partial u}{\partial x}] \\ + \frac{\partial}{\partial y} [\rho u v - \mu (\frac{\partial v}{\partial x} + \frac{\partial u}{\partial y})] = 0 \end{aligned} \quad (10)$$

$$\begin{aligned} \frac{\partial}{\partial t} (\rho v) + \frac{\partial}{\partial x} [\rho u v - \mu (\frac{\partial v}{\partial x} + \frac{\partial u}{\partial y})] \\ + \frac{\partial}{\partial y} [\rho v^2 + p + \frac{2}{3} \mu (\frac{\partial v}{\partial y} + \frac{\partial u}{\partial x}) - 2 \mu \frac{\partial v}{\partial y}] = 0 \end{aligned} \quad (11)$$

$$\begin{aligned} \frac{\partial}{\partial t} (\rho E) + \frac{\partial}{\partial x} \{ \rho u H - k \frac{\partial T}{\partial x} + \sum_{k=1}^{14} \rho_k h_k v_{kx} \\ + u [\frac{2}{3} \mu (\frac{\partial u}{\partial x} + \frac{\partial v}{\partial y}) - 2 \mu \frac{\partial u}{\partial x}] + v [-u (\frac{\partial v}{\partial x} + \frac{\partial u}{\partial y})] \} \\ + \frac{\partial}{\partial y} \{ \rho v H - k \frac{\partial T}{\partial y} + \sum_{k=1}^{14} \rho_k h_k v_{ky} + u [-\mu (\frac{\partial v}{\partial x} + \frac{\partial u}{\partial y})] \\ + v [\frac{2}{3} \mu (\frac{\partial u}{\partial x} + \frac{\partial v}{\partial y}) - 2 \mu \frac{\partial v}{\partial y}] \} = 0 \end{aligned} \quad (12)$$

$$\frac{\partial}{\partial t} (\rho_k) + \frac{\partial}{\partial x} [\rho_k (u + v_{kx})] + \frac{\partial}{\partial y} [\rho_k (v + v_{ky})] = \dot{\omega}_k \quad (13)$$

These equations are further nondimensionalized by the following appropriate parameters in order to facilitate computations.

$$t' = \frac{t}{L/U_r}, \quad x' = \frac{x}{L}, \quad y' = \frac{y}{L}$$

$$u' = u/U_r, \quad v' = v/U_r, \quad v'_{kx} = v_{kx}/U_r, \quad v'_{ky} = v_{ky}/U_r$$

$$\rho'_k = \rho_k/\rho_r, \quad \rho' = \rho/\rho_r, \quad p' = p/\rho_r U_r^2, \quad T' = T/T_r$$

$$k' = k/k_r, \quad \mu' = \mu/\mu_r$$

$$h'_k = h_k/U_r^2, \quad h' = h/U_r^2, \quad H' = H/U_r^2, \quad E' = E/U_r^2$$

The non-dimensionalized set of these equations, after dropping the primes for convenience and still written in the conservation form, is,

$$\frac{\partial}{\partial t} (\rho) + \frac{\partial}{\partial x} (\rho u) + \frac{\partial}{\partial y} (\rho v) = 0 \quad (14)$$

$$\begin{aligned} \frac{\partial}{\partial t} (\rho u) + \frac{\partial}{\partial x} [\rho u^2 + p + \frac{2}{3} \mu (\frac{\partial u}{\partial x} + \frac{\partial v}{\partial y})/Re_r - 2 \mu (\frac{\partial u}{\partial x})/Re_r] \\ + \frac{\partial}{\partial y} [\rho uv - \mu (\frac{\partial v}{\partial x} + \frac{\partial u}{\partial y})/Re_r] = 0 \end{aligned} \quad (15)$$

$$\begin{aligned} \frac{\partial}{\partial t} (\rho v) + \frac{\partial}{\partial x} [\rho uv - \mu (\frac{\partial u}{\partial y} + \frac{\partial v}{\partial x})/Re_r] + \frac{\partial}{\partial y} [\rho v^2 + p \\ + [\frac{2}{3} \mu (\frac{\partial u}{\partial x} + \frac{\partial v}{\partial y}) - 2 \mu (\frac{\partial v}{\partial y})]/Re_r] = 0 \end{aligned} \quad (16)$$

$$\begin{aligned} \frac{\partial}{\partial t} (\rho E) + \frac{\partial}{\partial x} [\rho uH - \frac{1}{c_{prmg}} k \frac{\partial T}{\partial x} + \sum_{k=1}^{14} \rho_k h_k v_{kx}] \\ + \frac{u}{Re_r} [\frac{2}{3} \mu (\frac{\partial u}{\partial x} + \frac{\partial v}{\partial y}) - 2 \mu \frac{\partial u}{\partial x}] + \frac{v}{Re_r} [-\mu (\frac{\partial v}{\partial x} + \frac{\partial u}{\partial y})] \\ + \frac{\partial}{\partial y} [\rho uH - \frac{1}{c_{prmg}} k \frac{\partial T}{\partial y} + \sum_{k=1}^{14} \rho_k h_k v_{ky} + \frac{u}{Re_r} [- (\frac{\partial v}{\partial x} + \frac{\partial u}{\partial y})] \\ + \frac{v}{Re_r} [\frac{2}{3} \mu (\frac{\partial u}{\partial x} + \frac{\partial v}{\partial y}) - 2 \mu \frac{\partial v}{\partial y}] = 0 \end{aligned} \quad (17)$$

$$\frac{\partial}{\partial t} (\rho_k) + \frac{\partial}{\partial x} [\rho_k (u + v_{kx})] + \frac{\partial}{\partial y} [\rho_k (v + v_{ky})] = (\frac{L}{\rho_r^{14} r}) \dot{\omega}_k \quad (18)$$

where $Re_r = \frac{\rho_r U_r L}{\mu_r}$ reference Reynolds number and

$$c_{prmg} = \frac{1}{Pr_r \times Re_r \times (M_r)^2 \times (\gamma_r - 1)}$$

where $Pr_r = \frac{\mu_r c_{p_r}}{k_r}$ reference Prandtl's number

$$M_r = \frac{U_r}{\sqrt{\gamma_r R_r T_r}} \text{ reference Mach number}$$

$$\gamma_r = \frac{c_{p_r}}{c_{v_r}}$$

Equations (14) - (18) can also be rewritten as

$$\frac{\partial \bar{U}}{\partial t} + \frac{\partial \bar{F}}{\partial x} + \frac{\partial \bar{G}}{\partial y} = \bar{K} \quad (19)$$

where \bar{U} , \bar{F} , \bar{G} and \bar{K} are one dimensional tensors (vector) with 18 components each, namely,

$$\bar{U} = \begin{array}{l} 1 \quad \rho \\ 2 \quad \rho u \\ 3 \quad \rho v \\ 4 \quad \rho E \\ 5 \quad \rho_1 \\ 6 \quad \rho_2 \\ 7 \quad \rho_3 \\ 8 \quad \rho_4 \\ 9 \quad \rho_5 \\ 10 \quad \rho_6 \\ 11 \quad \rho_7 \\ 12 \quad \rho_8 \\ 13 \quad \rho_9 \\ 14 \quad \rho_{10} \end{array}$$

$$\bar{U} \text{ cont.} = \begin{array}{ll} 15 & \rho_{11} \\ 16 & \rho_{12} \\ 17 & \rho_{13} \\ 18 & \rho_{14} \end{array}$$

$$1 \quad \rho u$$

$$2 \quad [\rho u^2 + p + \frac{2}{3} \mu (\frac{\partial u}{\partial x} + \frac{\partial v}{\partial y}) / Re_r - 2 \mu (\frac{\partial u}{\partial x}) / Re_r]$$

$$3 \quad [\rho uv - \mu (\frac{\partial u}{\partial y} + \frac{\partial v}{\partial x}) / Re_r]$$

$$4 \quad \{ \rho u H - \frac{1}{c_{prmg}} k \frac{\partial T}{\partial x} + \sum_k \rho_k h_k v_{kx}$$

$$+ \frac{u}{Re_r} [\frac{2}{3} \mu (\frac{\partial u}{\partial x} + \frac{\partial v}{\partial y}) - 2 \mu \frac{\partial u}{\partial x}$$

$$+ \frac{v}{Re_r} [-\mu (\frac{\partial v}{\partial x} + \frac{\partial u}{\partial y})]$$

$$\bar{F} = \begin{array}{ll} 5 & \rho_1 (u + v_{1x}) \\ 6 & \rho_2 (u + v_{2x}) \\ 7 & \rho_3 (u + v_{3x}) \\ 8 & \rho_4 (u + v_{4x}) \\ 9 & \rho_5 (u + v_{5x}) \\ 10 & \rho_6 (u + v_{6x}) \\ 11 & \rho_7 (u + v_{7x}) \\ 12 & \rho_8 (u + v_{8x}) \\ 13 & \rho_9 (u + v_{9x}) \\ 14 & \rho_{10} (u + v_{10x}) \\ 15 & \rho_{11} (u + v_{11x}) \\ 16 & \rho_{12} (u + v_{12x}) \\ 17 & \rho_{13} (u + v_{13x}) \\ 18 & \rho_{14} (u + v_{14x}) \end{array}$$

$$1 \quad \rho v$$

$$2 \quad [\rho uv - \mu (\frac{\partial v}{\partial x} + \frac{\partial u}{\partial y}) / Re_r]$$

$$3 \quad [\rho u^2 + p + \frac{2}{3} \mu (\frac{\partial u}{\partial x} + \frac{\partial v}{\partial y}) / Re_r \\ - 2 \mu (\frac{\partial v}{\partial y}) / Re_r]$$

$$4 \quad \{ \rho v H - \frac{1}{c_{prmg}} k \frac{\partial T}{\partial y} + \sum_k \rho_k h_k v_{ky}$$

$\bar{G} =$

$$+ \frac{u}{Re_r} [-\mu (\frac{\partial v}{\partial x} + \frac{\partial u}{\partial y})]$$

$$+ \frac{v}{Re_r} [\frac{2}{3} \mu (\frac{\partial u}{\partial x} + \frac{\partial v}{\partial y}) - 2 \mu \frac{\partial v}{\partial y}] \}$$

$$5 \quad \rho_1 (v + v_{1x})$$

$$6 \quad \rho_2 (v + v_{2x})$$

$$7 \quad \rho_3 (v + v_{3x})$$

$$8 \quad \rho_4 (v + v_{4x})$$

$$9 \quad \rho_5 (v + v_{5x})$$

$$10 \quad \rho_6 (v + v_{6x})$$

$$11 \quad \rho_7 (v + v_{7x})$$

$$12 \quad \rho_8 (v + v_{8x})$$

$$13 \quad \rho_9 (v + v_{9x})$$

$$14 \quad \rho_{10} (v + v_{10x})$$

$$15 \quad \rho_{11} (v + v_{11x})$$

$$16 \quad \rho_{12} (v + v_{12x})$$

$$17 \quad \rho_{13} (v + v_{13x})$$

$$18 \quad \rho_{14} (v + v_{14x})$$

$$\bar{K} = \left(\frac{L}{\mu r^{\rho} r} \right)$$

1	0
2	0
3	0
4	0
5	$\dot{\omega}_1$
6	$\dot{\omega}_2$
7	$\dot{\omega}_3$
8	$\dot{\omega}_4$
9	$\dot{\omega}_5$
10	$\dot{\omega}_6$
11	$\dot{\omega}_7$
12	$\dot{\omega}_8$
13	$\dot{\omega}_9$
14	$\dot{\omega}_{10}$
15	$\dot{\omega}_{11}$
16	$\dot{\omega}_{12}$
17	$\dot{\omega}_{13}$
18	$\dot{\omega}_{14}$

3.2 CALCULATION OF RELATED QUANTITIES

The remaining unknowns in equations (14) - (18) were computed from the basic variables ρ , T and ρ_k using auxiliary equations.

3.2.1 Calculation of Static Enthalpy of Each Species, (h_k), Total

Energy of the Mixture (E) and Total Enthalpy of the Mixture (H):

$$h_k = e_k + R_k T \quad \text{where } k = 1, 2, \dots, 14 \quad (20)$$

where e_k is the species internal energy consisting of contributions from translational, rotational and vibrational energies and the heats of formation of the species k .

$$\text{i.e. } e_k = (e_{\text{tran.}})_k + (e_{\text{rot.}})_k + (e_{\text{vib.}})_k + (e_{\text{form.}})_k \quad (21)$$

for $k = 1, 2, \dots, 14$.

Expanding and writing for each species (subscript k corresponds to species as given in Table II),

$$e_1 = \frac{3}{2} R_1 T + R_1 T + (e_{\text{vib.}})_1 + \Delta H_{f_1}^0$$

$$e_2 = \frac{3}{2} R_2 T + R_2 T + (e_{\text{vib.}})_2 + \Delta H_{f_2}^0$$

$$e_3 = \frac{3}{2} R_3 T + \Delta H_{f_3}^0$$

$$e_4 = \frac{3}{2} R_4 T + \Delta H_{f_4}^0$$

$$e_5 = \frac{3}{2} R_5 T + \Delta H_{f_5}^0$$

$$e_k = \frac{5}{2} R_k T + (e_{\text{vib}})_k + \Delta H_{f_k}^0$$

where $k = 6, 7, \dots, 14$

Species 6 through 14 are various vibrational levels of HF. Therefore,

$$R_k = R_6 \text{ and } \Delta H_{f_k}^0 = \Delta H_{f_6}^0 \text{ for } k = 7, 8, \dots, 14.$$

For species F, H and He the rotational and vibrational modes are nonexistent.

Also since the gas static temperature is expected to remain relatively low, vibrational energies of F_2 and H_2 could be neglected i.e. $(e_{\text{vib.}})_1 = (e_{\text{vib.}})_2 = 0$. Heats of formation of F_2 , H_2 and He are zero by definition. Table II contains vibrational energies and heats of formation of various species.

Thus,

$$\begin{aligned} \rho e &= \sum_{k=1}^{14} \rho_k e_k \\ &= \frac{5}{2} T \left(\sum_{k=1}^{14} \rho_k R_k \right) - T(\rho_3 R_3 + \rho_4 R_4 + \rho_5 R_5) \\ &\quad + \sum_{k=6}^{14} \rho_k (e_{\text{vib.}})_k + \sum_{k=1}^{14} \rho_k (\Delta H_f^0)_k \end{aligned} \quad (22)$$

Then,

$$\rho E = \rho \left(\frac{u^2 + v^2}{2} \right) + \rho e \quad (23)$$

and,

$$\rho H = \rho E + \rho RT \quad (24)$$

3.2.2 Calculation of the Species and Mixture Transport Properties:

The transport properties are calculated first for each individual species at the given temperature and pressure, and then obtained for the complete mixture for given mole fractions.

3.2.2a Viscosity

Viscosity for each species can be given by³⁴

$$\eta = .000026693 \left[\frac{1}{\sigma^2} \sqrt{M \frac{\epsilon}{k}} \right] \left[\frac{\sqrt{kT/\epsilon}}{\Omega(2,2)^*} \right] \quad (25)$$

Here $\Omega(2,2)^*$ is a function of ϵ/kT and is related as

$$\frac{1}{\Omega(2,2)^*} = .697 (1 + .323 \ln T^*)$$

where $T^* = kT/\epsilon$

The values of σ and ϵ/k are also tabulated for various species in Table II.

The viscosity of the mixture μ , was then obtained using the Wilke estimation method for gases at low pressure.³²

$$\mu = \frac{6}{\sum_{i=1}^6} \left\{ \eta_i / \left[1 + \sum_{\substack{j=1 \\ j \neq i}}^6 \phi_{ij} \left(\frac{y_j}{y_i} \right) \right] \right\} \quad (26)$$

where

$$\phi_{ij} = \frac{\left[1 + \left(\frac{\eta_i}{\eta_j} \right)^{1/2} \left(\frac{M_j}{M_i} \right)^{1/4} \right]^2}{\sqrt{8} \left[1 + \left(\frac{M_i}{M_j} \right) \right]^{1/2}}$$

Here y_i and y_j are the mole fractions.

3.2.2b Thermal Conductivity

The thermal conductivity of an individual species is related to the viscosity of the species in the following manner.

For monoatomic species³⁴

$$\lambda' = \frac{15}{4} \frac{R}{M} \eta \quad (27)$$

and for diatomic species³⁴

$$\lambda = \lambda' \left[1 + 0.88 \left(\frac{2}{5} \frac{C_p}{R} - 1 \right) \right] \quad (28)$$

where λ and λ' are thermal conductivities in cal./cm. sec. $^{\circ}\text{K}$.

Equation (28) can be used for monoatomic gases as well since for monoatomic gases $C_p/R \approx 5/2$ and thus $\lambda \approx \lambda'$.

The thermal conductivity for a mixture of gases at low pressure can be shown to be given by³²

$$k = \sum_{i=1}^6 \left\{ \lambda_i^* / \left[1 + \sum_{\substack{j=1 \\ j \neq i}}^6 \left(\frac{M_{ij}}{M_i} \right)^{1/8} \phi_{ij} \left(\frac{y_j}{y_i} \right) \right] \right\} + \sum_{i=1}^6 \lambda_i^{**} / \left[1 + \sum_{\substack{j=1 \\ j \neq i}}^6 \phi_{ij} \left(\frac{y_j}{y_i} \right) \right] \quad (29)$$

where,

$$\lambda_i^* = \lambda_i \left\{ 1 + \left[1 + .35 \left((C_{p_i}/R) - 2 \right) \right] \right\}$$

for H_2 , F_2 and HF (diatomic species) and,

$$\lambda_i^* = \lambda_i \text{ for H, F and He.}$$

Also,

$$\lambda_i^{**} = \lambda_i - \lambda_i^* \text{ for } \text{H}_2, \text{F}_2 \text{ and HF}$$

$$= 0 \text{ for H, F and He}$$

$$M_{ij} = \left(\frac{M_i + M_j}{2} \right)$$

3.2.2c Diffusion Coefficients

Treating each vibrational level of HF as a separate species, the binary diffusion coefficients were first obtained for each of the 14 species yielding a total of 196 (14×14) binary diffusion coefficients. The (14×14) matrix is a symmetric matrix. Also the binary diffusion

coefficients are independent of their individual species concentrations but they do depend on the temperature and pressure.³²

$$D_{ij} = 0.001858 T^{3/2} [(M_i + M_j)/M_i M_j]^{1/2} / p \sigma_{ij}^2 \Omega_D \quad (30)$$

where

D_{ij} is the binary diffusion coefficient in cm^2/sec

p is pressure in atmospheres

T is temperature in $^{\circ}\text{K}$

$$\sigma_{ij} = \frac{\sigma_i + \sigma_j}{2} \text{ in } \text{\AA}$$

Ω_D is the thermal collision integral

$$\Omega_D = f(kT/\epsilon_{12})$$

where

$$\frac{\epsilon_{12}}{k} = \left(\frac{\epsilon_1}{k} \times \frac{\epsilon_2}{k} \right)^{1/2}$$

Variation of Ω_D with kT/ϵ_{12} was available in tabular form³², and was successively used to obtain a curve fit with a simple formula.

The 14 multicomponent diffusion coefficients D_{im} were obtained from the 196 binary diffusion coefficients by the following formula³²

$$D_{im} = \frac{1 - y_i}{14 \left[\sum_{\substack{j=1 \\ j \neq i}} (y_j / D_{ij}) \right]} \quad (31)$$

Species diffusion velocities (or diffusion mass flux) were related to concentration gradients by Fick's law.

$$\rho_i v_i = - \rho D_{im} \nabla C_i \quad (32)$$

3.2.3 Calculation of the Chemical Production Term $\dot{\omega}_i$:

The species chemical production term was calculated explicitly. Treating each vibrational level of HF as a separate species, 100 elementary reactions were obtained from the reactions and rate constants given in Table III³⁵. These reactions involve chemical pumping for HF, dissociation, V - V (vibrational - vibrational level) transfers and V - T (vibrational - translational) transfers. The chemical pumping is the cause of formation of various vibrational levels of HF whereas V - V and V - T transfers cause the destruction of population inversion and relaxation towards Boltzmann distribution causing a rise in translational temperature. The vibrational levels of H₂ were not treated separately as 3 different species, unlike in Ref. 35; rather H₂ was treated like a single species.

The equilibrium constants as a function of temperature were obtained from the JANAF Tables³⁶ for the dissociation reactions. For the other reactions viz. chemical pumping, V - V and V - T transfers, they were assumed to be of the form³⁷

$$k_{eq} = \exp[-(E_v - E_0)/RT] \quad (33)$$

Here the reaction is of the type,



where M is the collision partner.

$(E_v - E_0)$ is the energy of vth level above the ground state.

The backward rate constants can now readily be obtained since

$$k_b = k_f/k_{eq} \quad (35)$$

where k_f is the forward rate constant and k_{eq} the equilibrium constants for the elementary reaction in question.

Once all the rate constants are known, algebraic equations can be written for all the participating chemical components of each elementary reactions. Separating then the rates of production of each of the 14 species and adding them together from among all the algebraic equations the final rate equations can be written for each of the 14 species. One of these rate equations, namely for the chemical production of HF(1) is given below as an example.

$$\begin{aligned}
 \frac{d}{dt} [\text{HF}(1)] = & [k_{-31} [\text{H}][\text{F}] - k_{31} [\text{HF}(1)]] [\text{M}_6] \\
 & + (k_{4a} [\text{F}][\text{H}_2] - k_{4a} [\text{HF}(1)][\text{H}]) \\
 & + (k_{5b} [\text{H}][\text{F}_2] - k_{5b} [\text{HF}(1)][\text{F}]) \\
 & + (k_{-6a} [\text{HF}(0)] - k_{6a} [\text{HF}(1)]) [\text{M}_7] \\
 & + (k_{-6b1} [\text{HF}(0)] - k_{6b1} [\text{HF}(1)]) [\text{M}_8] \\
 & + (k_{6b2} [\text{HF}(2)] - k_{-6b2} [\text{HF}(1)]) [\text{M}_8] \\
 & + (k_{-6c1} [\text{HF}(0)] - k_{6c1} [\text{HF}(1)]) [\text{M}_9] \\
 & + (k_{6c2} [\text{HF}(2)] - k_{-6c2} [\text{HF}(1)]) [\text{M}_9] \\
 & + (k_{-6d1} [\text{HF}(0)] - k_{6d1} [\text{HF}(1)]) [\text{M}_{10}] \\
 & + (k_{6d2} [\text{HF}(2)] - k_{-6d2} [\text{HF}(1)]) [\text{M}_{10}]
 \end{aligned}$$

$$\begin{aligned}
& + (k_{6a2}[\text{HF}(2)] - k_{-6a2}[\text{HF}(1)])[M_7] \\
& + (k_{6f1}[\text{HF}(0)] - k_{-6f1}[\text{HF}(1)])[M_5] \\
& + (k_{6f2}[\text{HF}(2)] - k_{-6f2}[\text{HF}(1)])[M_5] \\
& + (k_{-6g1}[\text{HF}(0)] - k_{6g1}[\text{HF}(1)])[M_4] \\
& + (k_{6g2}[\text{HF}(2)] - k_{-6g2}[\text{HF}(1)])[M_4] \\
& + 2(k_{-7a1}[\text{HF}(0)][\text{HF}(2)] - k_{7a}[\text{HF}(1)]^2) \\
& + (k_{7a}[\text{HF}(2)]^2 - k_{-7a2}[\text{HF}(1)][\text{HF}(1)]^2) \\
& + (k_{-7b}[\text{HF}(3)][\text{HF}(0)] - k_{7b}[\text{HF}(1)][\text{HF}(2)]) \\
& + (k_{7b}[\text{HF}(2)][\text{HF}(3)] - k_{-7b2}[\text{HF}(1)][\text{HF}(4)]) \\
& + (k_{-7c1}[\text{HF}(0)][\text{HF}(4)] - k_{7c}[\text{HF}(1)][\text{HF}(3)]) \\
& + (k_{7c}[\text{HF}(2)][\text{HF}(4)] - k_{-7c2}[\text{HF}(1)][\text{HF}(5)]) \\
& + (k_{-7d1}[\text{HF}(0)][\text{HF}(5)] - k_{7d}[\text{HF}(1)][\text{HF}(4)]) \\
& + (k_{7a}[\text{HF}(2)][\text{HF}(5)] - k_{-7d}[\text{HF}(1)][\text{HF}(6)]) \tag{36}
\end{aligned}$$

The rate equations for all the remaining 13 species are given in Appendix A.

CHAPTER IV

GAIN

The small signal gain coefficient is an extremely important figure of merit for gas laser devices. It is a direct measurement of population inversion. Everything else being equal, the higher the small-signal gain, the easier laser action can be obtained in a gas.

Stimulated emission and absorption is considered and spontaneous emission is ignored because the characteristic test section temperature is small. Consider a slab of gas of geometric thickness dy , with radiation of intensity I_ν (per unit frequency) incident upon it as shown in Fig. 3. The radiative intensity absorbed in a given spectral line of the gas is dI_ν . Due to line broadening effect (natural, Doppler and Lorentz) dI_ν varies over a narrow frequency range as shown in Fig. 4, (this gives rise to the phenomena of line shape). The intensity of radiation between ν and $\nu + d\nu$ is $(dI_\nu)d\nu$. The integrated radiative intensity (total intensity absorbed by line) is³⁸

$$dI = \int_\nu (dI_\nu)d\nu \quad (37)$$

The spectral absorption coefficient α_ν is defined as

$$dI_\nu = -\alpha_\nu I_\nu dy \quad (38)$$

Examining Eq. (38) if I_ν decreases as the radiation traverses the slab of gas, then dI_ν is negative and α_ν is positive. On the other hand if I_ν increases as in the laser effect, then dI_ν is positive and α_ν is negative. Hence defining small signal gain coefficient $G_{0\nu}$ as

$$G_{O_v} = -\alpha_v \quad (39)$$

Eq. (38) can now be rewritten as

$$dI_v = G_{O_v} I_v dy \quad (40)$$

For a constant G_{O_v} along the path, the Eq. (40) integrates to Beer's law⁶

$$\frac{I}{I_0} = e^{G_{O_v} (y - y_0)} \quad (41)$$

For a single V - R transition, G_{O_v} can be written in terms of number densities N_u and N_l of the upper and lower states, the upper and lower degeneracies g_u and g_l , the transition wave number ω , a normalized line profile parameter $\phi(\omega - \omega_e)$ -- where ω_e is the centerline wave number -- and an Einstein absorption coefficient $B_{l \rightarrow u}$, as,⁶

$$\int_v G_{O_v} dv \equiv G_{O_v}(\omega) = \frac{h B_{l \rightarrow u}}{4\pi} \omega \left(\frac{g_l}{g_u} N_u - N_l \right) \quad (42)$$

where h is Planck's constant and 4π is the total solid angle about a point.

Introduce now mole mass ratio $n(v, J)$ for state (v, J) and $n(v)$ for vibrational level v . The number densities in Eq. (42) are replaced by⁶

$$N_l = N_A \rho n(v, J) \quad (43)$$

$$N_u = N_A \rho n(v+1, J-1) \quad \text{for P transitions}$$

Assuming equilibrium Boltzmann distribution for the rotational populations at the translation temperature T :

$$n(v, J) = n(v) \frac{g_v}{Q(v)} \exp \left[-\frac{hc}{k} \frac{E(v, J)}{T} \right] \quad (44)$$

Inserting Eqs. (43), (44) into Eq. (42) yields

$$\begin{aligned} G_0(v, J) &= \frac{h N_A}{4\pi} \omega_c(v, J) \phi_c \rho B(v, J)(2J+1) \\ &\times \frac{n(v+1)}{Q(v+1)} \exp \left[-\frac{hc}{kT} E(v+1, J-1) \right] \\ &- \frac{n(v)}{Q(v)} \exp \left[-\frac{hc}{kT} E(v, J) \right] \end{aligned} \quad (45)$$

where subscript c refers to centerline values.

The molecular quantities needed for calculating the gain for any vibrational/rotational transition are transition wave length, Einstein coefficients for spontaneous and stimulated emission and the line shape function.

The transition wave length is determined by the vibrational/rotational energy level spacing within the molecule. The rotational-vibrational energy is given by the following expression²⁹

$$\begin{aligned} E(v, J) &= B_e J(J+1) - D_e J^2(J+1) + H_e J^3(J+1)^3 \\ &- A_e J(J+1)(v + \frac{1}{2}) - \beta_e J^2(J+1)(v + \frac{1}{2}) \end{aligned} \quad (46)$$

where

$$\begin{aligned} A_e &= 0.796 \text{ cm}^{-1} & B_e &= 20.95 \text{ cm}^{-1} \\ D_e &= 4 B_e^3 / \omega_e^2 \\ H_e &= 2 D_e (12 B_e^2 - A_e \omega_e) / 3 \omega_e^2 \\ \beta_e &= D_e \left[(8 \omega_e x_e / \omega_e) - (5 A_e / B_e) - (A_e^2 \omega_e / 24 B_e^3) \right] \end{aligned}$$

where $\omega_e = 4.14 \times 10^3 \text{ cm}^{-1}$

and $\omega_e x_e = 90.0 \text{ cm}^{-1}$

The Einstein coefficients denote the probabilities for stimulated and spontaneous emissions. The Einstein coefficient for absorption is simply related to that for a stimulated emission. The probability of transition $(v+1, J-1)$ to (v, J) is given by the square of the matrix element $|R_v^{v+1}|$. The quantum mechanical calculation is described in Ref. 46. The Einstein coefficient in Eq. (45) is related to a matrix element by⁶

$$B(v, J) = \frac{16 \pi^4}{3 h^2 c} \left(\frac{2J+1+m}{2J+1} \right) |R_v^{v+1}|^2 \quad (47)$$

where $m = -1$ for P transitions

and $m = +1$ for R transitions

Line shape function is another important quantity in laser calculations. Einstein coefficients are determined by particle structure. They determine the total rate of emission and absorption integrated over the entire spectral line width. Because the Einstein coefficients represent integral values, the peak values of emission and absorption depend on the width and shape of the spectral lines. There are two major physical phenomena causing line broadening of the extremely small natural line width that would be observed from particles at rest. These two phenomena are frequency variations due to thermal motion of the particles (Doppler broadening), and those resulting from the interruption of radiative processes by particle collisions (Lorentz broadening).

According to Mitchell and Zemansky³⁹ and Emanuel et al¹⁰ the line shape function for combined Doppler and Lorentz broadening, assuming that

lasing occurs at the line center frequency, can be written as²⁰

$$\phi_c = \frac{2}{\Delta \nu_D} \left(\frac{\ln 2}{\pi} \right)^{1/2} V(\eta) \quad (48)$$

Here $V(\eta)$ is the Voigt function, given by⁶

$$V(\eta) = \exp(-\eta^2) [1 - \text{erf}(\eta)] \quad (49)$$

and η is essentially the ratio of the Lorentz line width to the Doppler line width.

Assuming now pure Doppler broadening, in the limit as $\eta \rightarrow 0$, $V(\eta) \rightarrow 1.0$ and

$$\phi_{c,D} = \frac{2}{\Delta \nu_D} \left(\frac{\ln 2}{\pi} \right)^{1/2} \quad (50)$$

Here $\Delta \nu_D$ is the Doppler line width at half the peak intensity.

According to Lengyel³⁰

$$\Delta \nu_D = \frac{2\omega_c}{c} \left(\frac{2RT \ln 2}{M_{HF}} \right)^{1/2} \quad (51)$$

where ω_c is transition wave number

M_{HF} is molecular weight of HF

and R is universal gas constant.

Substituting into Eq. (50)

$$\phi_{c,D} = \frac{c}{\omega_c} \left(\frac{M_{HF}}{2\pi RT} \right)^{1/2} \quad (52)$$

Assuming now that only the P-branch transitions occur (i.e. transitions proceeding from $(V+1, J-1)$ to (V, J)) and that rotational equilibrium also exists, and substituting Eqs. (47), (52) into Eq. (45) we obtain for Gain,

$$\begin{aligned}
G_0(v, J) &= \frac{h N_A}{4\pi} \omega_c \left[\frac{c}{\omega_c} \left(\frac{M_{HF}}{2\pi RT} \right)^{1/2} \right] \times \rho \\
&\times \left\{ \frac{16\pi^4}{3h^2 c} \left(\frac{2J+1-1}{2J+1} \right) |R_v^{v+1}|^2 \right\} (2J+1) \\
&\times \frac{1}{M_{HF}} \left\{ \frac{c(v+1)}{Q(v+1)} \exp \left[-\frac{hc}{kT} E(v+1, J-1) \right] \right. \\
&\left. - \frac{c(v)}{Q(v)} \exp \left[-\frac{hc}{kT} E(v, J) \right] \right\} \quad (53)
\end{aligned}$$

where $n(v) = \frac{c(v)}{M_{HF}}$

$c(v)$ being the mass fraction; and $m = -1$ has been substituted for P-transition.

Simplifying this expression algebraically we get, finally

$$G_0(v, J) = A [c(v+1) - \lambda c(v)] \quad (54)$$

where

$$A = \frac{8\pi^{5/2} N_A^{1/2}}{3h(2k M_{HF} T)^{1/2}} \frac{|R_v^{v+1}|^2}{Q(v+1)} \times \rho$$

$$\times \exp -[E(v+1, J-1)hc/kT]$$

$$\lambda = \frac{Q(v+1)}{Q(v)} \exp -[(E(v, J) - E(v+1, J-1))hc/kT]$$

$$c(v) = \frac{\rho_{HF}(v)}{\rho} \equiv \text{mass fraction}$$

$$Q(v) = \sum_{j=0}^{\infty} (2J+1) \exp -[E(v, J)hc/kT]$$

\equiv rotational partition function

$$E(v,J) \approx 20.95 J(J+1) - 0.796 J(J+1)(v + \frac{1}{2}) \text{ cm}^{-1}$$

\equiv vibrational-rotational energy

It should be noted that the expression for $E(v,J)$ given above is the same as that given earlier as Eq. (46) except that the higher order terms are neglected here.

$|R_v^{v+1}|^2$ is the vibrational contribution to the electric dipole moment. Population inversion is expected to exist only between the levels 1-0 and 2-1, and hence the necessary values of $|R_v^{v+1}|^2$ required for gain calculations are,

$$|R_0^1|^2 = 1.11 \times 10^{-38} \text{ erg-cm}^3$$

and

$$|R_1^2|^2 = 2.26 \times 10^{-38} \text{ erg-cm}^3$$

Small signal gain at every point in the flow field mesh can be calculated for various (v,J) transitions. The averaged small signal Gain in the y direction is just simply,

$$G_{0,av.}(v,J) = \frac{1}{h} \int_0^h G_0(v,J)(y) dy \quad (55)$$

CHAPTER V
THE NUMERICAL METHOD

5.1 THE TIME DEPENDENT APPROACH

Equation (19) can be rewritten in the following form,

$$\frac{\partial \bar{U}}{\partial t} = - \frac{\partial \bar{F}}{\partial x} - \frac{\partial \bar{G}}{\partial y} + \bar{K} \quad (56)$$

Here the vectors \bar{U} , \bar{F} , \bar{G} and \bar{K} consist, as discussed earlier, of the flow field properties and their first order derivatives. If the distribution of the flow field variables is specified everywhere in the test section at any instant of time t^n (i.e. after n time steps), then the vectors \bar{U} , \bar{F} and \bar{G} can be computed. Vector \bar{K} can also be computed explicitly since the temperature, rate constants and mole fractions of each of the species are known. Since \bar{F} and \bar{G} vectors are now known, $\frac{\partial \bar{F}}{\partial x}$ and $\frac{\partial \bar{G}}{\partial y}$ can also be computed using a finite difference scheme. In turn, then, the time derivative $\partial \bar{U} / \partial t$ can be calculated from Eq. (56).

For small enough time step i.e. Δt , then the Taylor series expansion of vector \bar{U} about the time instant t^n , could in principle yield the value of vector \bar{U} at time t^{n+1} by

$$\bar{U}^{n+1} = \bar{U}^n + \left(\frac{\partial \bar{U}}{\partial t} \right)_n \Delta t \quad (57)$$

The components of this new vector \bar{U}^{n+1} are enough to specify all the properties at any grid point one step ahead in time. From this, again, the vectors F , G and K and $\frac{\partial F}{\partial x}$, $\frac{\partial G}{\partial y}$ can be calculated at time t^{n+2} to eventually yield \bar{U}^{n+2} . This process then can be repeated until a steady state is reached, i.e. when $\partial \bar{U} / \partial t$ approaches zero.

However, Eq. (57) is of first order accuracy only. Therefore, a time dependent technique patterned after the MacCormack approach²⁴ was used to generate the steady state solution. (See Refs. 40 and 41 for further applications of this technique.) MacCormack uses a predictor-corrector method which is of second order accuracy. It involves the generation of intermediate predicted values at time t^{n+1} via Eq. (58) below. These predicted values are used again in the conservation equation in a "corrector" fashion to obtain values at time $(n + 2)$ as shown in Eq. (59) below. Averaging of these two steps leads to a higher accuracy (of second order) at time t^{n+1} as described in the following three equations,

$$\tilde{U}^{n+1} = \bar{U}^n + \left[-\frac{\partial \bar{F}}{\partial x} - \frac{\partial \bar{G}}{\partial y} + \bar{K} \right]_n \Delta t \quad (58)$$

$$\tilde{U}^{n+2} = \tilde{U}^{n+1} + \left[-\frac{\partial \tilde{F}}{\partial x} - \frac{\partial \tilde{G}}{\partial y} + \tilde{K} \right]_{n+1} \Delta t \quad (59)$$

and

$$\bar{U}^{n+1} = \bar{U}^n + \frac{\tilde{U}^{n+2} - \tilde{U}^n}{2} \quad (60)$$

Here n refers to the time step and tilde refers to the intermediate values.

5.2 DIFFERENCING SCHEME

The vectors \bar{F} and \bar{G} contain first order spatial gradients of temperature and velocities directly and of species concentrations indirectly through the diffusion velocities. In turn, spatial gradients of vectors \bar{F} and \bar{G} need also to be taken to first order to solve Eqs. (58) and (59). Thus effectively, second order spatial derivatives are needed for some of the thermodynamic quantities during both the predictor and

corrector step calculations. This offers a possibility of various combinations of the so called forward, backward and central differencing schemes to calculate the gradients. Several combinations were tried and results were compared. Appendix B contains a detailed discussion of such schemes tried for cold flows¹⁶⁻¹⁷. The scheme summarized below yielded the best results and was hence recognized as the most appropriate scheme for the mixing flows of present interest. This differencing scheme was termed the "Modified MacCormack" scheme.

During the predictor step calculations, forward differencing is used for computing the gradients of \bar{F} and \bar{G} , i.e.,

$$\frac{\partial \bar{F}}{\partial x}(2,j,k) = \frac{\bar{F}(3,j,k) - \bar{F}(2,j,k)}{\Delta x} \quad (61)$$

$$\frac{\partial \bar{G}}{\partial y}(i,2,k) = \frac{\bar{G}(i,3,k) - \bar{G}(i,2,k)}{\Delta y} \quad (62)$$

whereas for calculating the gradients of T , u , v and ρ_k which occur in \bar{F} and \bar{G} , a backward differencing scheme is used, i.e.,

$$\frac{\partial \bar{T}}{\partial x}(2,j,k) = \frac{\bar{T}(2,j,k) - \bar{T}(1,j,k)}{\Delta x} \text{ etc.} \quad (63)$$

Here i denotes the x-wise location and j denotes the y-wise location and k is the relative location in vector.

But during the corrector step calculations, the reverse combination is applied. $\frac{\partial \bar{F}}{\partial x}$ and $\frac{\partial \bar{G}}{\partial y}$ are now computed using backward differencing while gradients of T , u , v and ρ_k are calculated with forward differencing. Such a scheme is used for all the remaining cold and hot flow calculations.

5.3 TIME STEP

5.3.1 Fluid Dynamic Criteria

Let the grid spacing in the x and y direction (defined in Fig. 1) be given by Δx and Δy respectively. If u and v are the mass velocities in x and y directions and if 'a' is local speed of sound, then the time interval required for any disturbance to propagate in the x direction to the nearest grid point would be

$$(\Delta t)_x = \frac{\Delta x}{u + a} \quad (64)$$

Similarly for the y direction it would be

$$(\Delta t)_y = \frac{\Delta y}{v + a} \quad (65)$$

The criteria for selecting the magnitude of time step required to advance the solution in time is due to Courant, Fredrich and Levy⁴² and is hence called CFL criteria. It states that the time step should be smaller than the time required for the information from one grid point to reach its neighboring grid point. In other words all the grid points are discretized and the information at one grid point is reatted to the next and only through the gradients. The time step according to CFL criteria is then the minimum of $(\Delta t)_x$ and $(\Delta t)_y$ calculated at every grid point.

The time step used in the calculations is in general smaller though, then the CFL criteria time step and is given as,

$$\Delta t = k (\Delta t)_{CFL} \quad (66)$$

where,

$$0 < k < 1$$

The value of k used for the present calculation varied from 0.3 to 0.5.

5.3.2 Chemical Kinetic Criteria

The other time step criteria for problems with chemical kinetics is due to the chemical relaxation processes. The time step has to be smaller than the characteristic time required for the production of each species. The chemical relaxation time can be given as,⁴³

$$\tau_i = -1 / \frac{d[\dot{\omega}_i]}{d[\omega_i]} \quad (67)$$

where i refers to various species and $i = 1, 2, \dots, 14$.

In order to obtain expressions for τ_i , the species production term equations i.e. equations of the type given in Appendix A, are differentiated with respect to the species on the L.H.S. and the negative inverse of which is then calculated. This gives the characteristic chemical relaxation time τ_i for the species, the minimum of which dictates the time step.

Again the actual time step is a minimum of $(\Delta t)_{CFL}$ and $(\Delta t)_{chem}$. For the present calculation $(\Delta t)_{chem}$ was generally calculated to be greater than the $(\Delta t)_{CFL}$. Although some of the reactions are hypergolic, the $(\Delta t)_{CFL}$ is very small since the dimensions of the laser cavity are extremely small and velocities are large.

5.4 GRID SIZE AND CONVERGENCE

A 9×9 mesh (with 81 grid points) was used in general. Other mesh sizes such as 5×5 , 13×13 and 17×17 were also used. A few words about convergence are in order. The present time-dependent calculations

smoothly and regularly approach a steady-state solution as long as the requisite stability criteria are followed; i.e., the solutions are stable as long as the time increment is less than the CFL and chemical relaxation times. With regard to convergence, the question can be asked: Is enough accuracy obtained with the present 9×9 grid, which at first glance appears rather coarse? An answer is given in Fig. 5. Here, the final steady-state temperature at $x/h = 5$ and $y/h = 0.75$ is given for three different grid sizes: 5×5 , 9×9 and 13×13 . It appears that a 9×9 grid is sufficiently accurate, and that a further definition by more grid points is unnecessary. This is totally consistent with time-dependent solutions of other problems^{1,31,40,41} where sufficient accuracy has been obtained with seemingly very coarse grids. Apparently, the time-dependent mechanism is "self-correcting" at each time step, allowing the physics contained in the conservation equations to bear more strongly and accurately at each grid point. The philosophical point notwithstanding, experience has clearly proven that time-dependent solutions require fewer grid points than might be expected for steady-state analyses. The present results are a case in point. As long as the cell Reynolds number in the y direction is on the order of unity, the gradients are adequately accounted for, as in the present calculations. A 17×17 grid was used when a more definition of the flow field was needed for base flow calculations etc.

CHAPTER VI

COLD FLOW

6.1 INLET CONDITIONS

The initial conditions on thermodynamic variables were chosen to be the same as the inlet conditions which were held fixed in time for the majority of problems considered. The inlet conditions were calculated in the following manner so as to give pressure and temperature uniformity. The thermodynamic values of variables in the upper and lower streams in the test section at the start of solution are in general taken to be the same as those existing at the inlet. The solution is then advanced in time for the entire test section but the inlet conditions are held time invariant.

The inlet conditions chosen were representative of a typical chemical laser case. The dimensions of the nozzle exit given in Fig. 1 were also selected in the same manner from previous experimental results. The pressure at the inlet in both the nozzles was uniform at 500 N/m^2 and temperature at 150°K . Such cold temperatures and low pressures are typical of chemical lasers. The fluorine stream contained F , F_2 and He whereas the hydrogen stream contained H_2 and a minute quantity of diluent He . For known mole fractions (or partial pressures), then the densities of each individual constituent species can be calculated. The streams are presumed to be parallel mixing and hence y component of velocity in both inlet streams is also zero. The x component of velocity, viz. u , was also chosen to represent a typical chemical laser case. The ratio of u velocities in F_2 and H_2 streams was 2:1.

6.2 RESULTS AND DISCUSSION

In order to consolidate and summarize the solution of Navier Stokes equations for chemical laser "cold flows", Figs. 6 - 12 give steady state results for a case typical of conventional supersonic diffusion chemical lasers. These results were obtained using the modified MacCormack scheme discussed in Appendix B, and treated a discontinuity at the inlet. A 13 x 13 mesh was employed. Figure 6 shows the progressive development of the velocity profiles at three different stations in the flow direction. Note the stronger effect of mixing on the slower and lower molecular weight stream of H_2 . Figure 7 gives pressure profiles at the same three stations. Note that for the present cold flows, p is essentially constant across the flow, and tends to decrease slightly in the flow direction. The corresponding temperature profiles are given in Fig. 8. Note that, as expected, T increases in the laminar mixing region, and tends to "diffuse" outward as the flow moves downstream. Also note that commensurate with the slightly decreasing p , T also decreases in the wings of the profile as the flow moves downstream, i.e. the wings of the flow appear to be in a slight expansion region. Again here emphasis is made that cold flows of the type analyzed in this chapter are purely artificial and these results have a meaning only within the interpretation given in Chapter 1.

The profiles of species density for F_2 , F and H_2 and He are given in Figures 9 - 12 respectively. These results isolate the effects of multicomponent diffusion. When examining these figures, keep in mind that the flow velocity of the upper stream is twice that of the lower stream. Hence for example in Fig. 11, the mass flow of H_2 is preserved, even though the profiles seem to show at first glance more H_2 lost from

the lower stream than gained by the upper stream. However, on mass flow basis, H_2 is preserved, as it should be for this purely non-reacting flow.

6.3 COMPUTATIONAL EXPERIMENTS

6.3.1 Variation in Grid Size

A 9×9 grid and a 13×13 grid were tried with the modified MacCormack approach. Steady state results for both are plotted in Figs. 13 through 17. A discontinuous velocity profile at the upstream boundary was used to obtain both sets of results. (The discontinuity lies at the interface of two streams as shown in Fig. 1). Exact simulation of the conditions that might prevail in a laboratory experiment could not be attained because of the finite grid size. The computer "sees" a discontinuity as a "ramp" of steepness based on the grid sizes. Thus reducing the grid size tends to make the discontinuity more severe. On this basis, a 9×9 grid size presented a weaker discontinuity than a 13×13 grid. The effect of this steepness in the discontinuity of the inlet velocity profile on the downstream flow field variables is shown in Figs. 13 through 17; the most marked variation being in the pressure profile of Fig. 14, being 6% for 13×13 grid and only 2% for the 9×9 grid.

6.3.2 Effect of a Continuous Velocity Profile

In general, mixing of the two streams has been treated as being discontinuous at the inlet. However, for the sake of comparison a case where the velocity profile at the inlet is continuous was simulated (with a discontinuity in ρ and ρ_k at the inlet). The lack of velocity discontinuity was observed to yield smoother profiles at other locations in the test section. As is apparent from Fig. 18, the pressure at a

particular grid point is seen to reach its final steady state value faster and in a much smoother fashion for a continuous velocity profile than a discontinuous one for the same grid size. The steady state value of pressure is also different because of the different inlet velocity profiles.

CHAPTER VII

HOT FLOW

7.1 WEAKLY REACTING CASE

7.1.1 Inlet Conditions

In the cold flow case, discussed in the previous chapter, the H_2 stream contained only a minute quantity of He as diluent. The lack of a sufficient amount of He and presence of considerable amount of H_2 produced rather highly reacting flow, when the hot flow was turned on, i.e. when the kinetics were switched on. Hence a case was run wherein the He content was increased in the H_2 stream, considerably. The inlet conditions again had uniform pressure of 500 n/m^2 and temperature of 150°K in both the streams. However, the mole fractions of the constituent species in both streams were quite different, both streams now being heavily diluted with Helium. The initial conditions are again the same as the inlet conditions, given in Fig. 19. The solution is advanced in time from the initial conditions discussed above with the chemical kinetics switched off, i.e. for cold flows. This allows the streams to partially mix with each other and the gradients of concentrations then become less severe at the interface as they diffuse out. The chemical kinetics are then switched on and the asymptotically steady state obtained by advancing the solution in time until a dynamic equilibrium is obtained.

7.1.2 Results and Discussion

Consider the point defined by $x/h = 10.0$ and $y/h = 0.375$. The time history of the static temperature at this point is given in Fig. 20. Cold flow calculations are made through a non-dimensionalized time

of 24 to allow the two streams to mix partially. After this time, hot flow calculations are made. Note from Fig. 20 that the switch to a hot flow causes a discontinuous increase in dT/dt , and a subsequent approach to a higher steady-state temperature. For comparison the purely cold-flow case is carried out to a steady state, as shown in Fig. 20. Note that the combined effect of chemical reactions and vibrational relaxation lead to a 23% increase in static temperature in comparison to the purely artificial cold-flow case.

Steady state profiles of velocity, pressure and temperature with respect to y/h for this case are given in Figs. 21, 22, and 23 respectively. These are plotted, in each figure, for various longitudinal locations viz. $x/h = 0, 5$ and 10 . Note from Fig. 21 that, in contrast to temperature, velocity profiles downstream of the nozzle exits show little influence due to chemical reactions -- a result that is almost classical in most high temperature gasdynamic problems.⁴³ Also note that the slower moving stream of H_2 is accelerated more than the faster moving stream of F and F_2 is retarded, due to mixing process. The pressure variations which are plotted on an expanded scale in Fig. 22, show virtually a constant pressure in the y direction, except for a small variation in the middle of the mixing zone. For hot flow, there is an adverse pressure gradient in the flow direction; in contrast the net effect of the purely fluid dynamic mixing appears to be a slight favorable pressure gradient, at least for the first 10 nozzle heights downstream. The corresponding temperature profiles are shown in Fig. 23. Comparing the cold flow profiles it is apparent that the viscous shear action causes a larger local temperature rise in the mixing region at

$x/h = 5.0$ than at $x/h = 10.0$ because y gradients of velocity are larger near the nozzle exits. However, in going from $x/h = 5.0$ to $x/h = 10.0$, the mean temperature rise is more (averaged over the whole cross section) whereas the peak temperature of the faster stream seems to drop because the interface streamlines would bend towards the slower stream. The average pressure also decreases slightly as the flow moves downstream as noted in Fig. 22. In contrast the hot flow temperature profiles clearly show almost discontinuous increase in temperature in the mixing region, a fact already noted from Fig. 20.

Figures 24 and 25 illustrate density profiles of various HF vibrational levels at $x/h = 5.0$ and 10.0 respectively. The growth of the reaction zone can be seen clearly. Total population inversions existing between vibrational levels increase as the flow moves downstream. The small signal gain, though, does not necessarily increase since the absolute difference between the densities of HF(0), HF(1) and HF(2) does not always increase.

The calculated growth of the reaction zone as defined by the region where $\rho_{\text{HF}(0)}$ is greater than 10% of the maximum value, is shown in Fig. 26. This figure is taken from Ref. 15, and contains experimental data taken at TRW. The present results are marked on Fig. 26 and show the same laminar variation as the experimental data.

The existence of population inversions and hence laser action is best seen in Fig. 27, where densities of various HF vibrational levels at $y/h = 0.375$ are plotted with respect to x . Inversions exist between the 0-1 levels and 1-2 levels, which generate the small-signal gain $G_0(v,J)$ as calculated from Eq. 54. These gains are shown in Figs. 28 and 29. Figure 28 shows the variation of the small signal gain with respect

to x at $y/h = 0.375$ for the vibrational level transition 1-0 for various rotational levels (only P-branch transitions are considered). Figure 29 shows similar results for the 2-1 transition. The values of gain and the spatial extent of the lasing region as indicated on Figs. 28 and 29 are typical of conventional HF chemical lasers, as obtained from Refs. 28 and 29.

7.2 STRONGLY REACTING CASE

7.2.1 Inlet Conditions

The previous case was weakly reacting since the quantities of reactants were low and diluents high, in addition to a low translational temperature. For the purposes of comparison, though, a case was run with inlet conditions taken from the report by King and Mirels²⁹ of Aerospace Corporation. The same case was also run on LAMP code²⁰ of Lockheed Missiles and Space Company, Inc., (Huntsville, Alabama). King and Mirels, as discussed earlier in the Introduction assume two semi-infinite streams, with pressure in both x and y directions constant; whereas the LAMP code calculated a pressure gradient in x direction by means of a quasi-one-dimensional heat-addition approximation.

The inlet conditions used are given in Fig. 30. The velocities were also different from the previous case; 1400 m/sec for stream 1 and 2140 m/sec for stream 2.

7.2.2 Results and Discussion

This mixture is so strongly reacting that a large adverse pressure gradient is produced in the flow direction. Note from Fig. 31 that both the present calculation and LAMP predict approximately a factor of five pressure increase in a distance on the order of a centimeter.

King and Mirels on the other hand have no pressure gradient; an assumption valid for two semi infinite streams but invalid for the real life chemical lasers -- represented by the present case of stacked nozzles. Figures 32 and 33 denote the temperature and HF(0) concentration variations in x direction for all three methods in consideration. A comparison between King and Mirels and the other solution is, though, not entirely valid since the boundary conditions are different. Nevertheless it is also included for the sake of completeness. Although LAMP did not work beyond a certain distance, it should be emphasized that the pressure, temperature and concentration variations for the distance over which the solution was obtained, show a close resemblance to the present results. Due to a lack of time, no further effort was made to obtain a complete solution with LAMP using perhaps smaller grid sizes etc. Thus results of LAMP shown in these figures in no way reflect on the viability of LAMP, but rather the fact that both the solutions followed each other quite so closely is the point that should be emphasized.

Figure 34 shows the temperature and HF(0) density profiles at $x/h = 10.0$ as calculated by both the LAMP code and the present program for the dilute case discussed in previous section. Results of Figs. 20 - 29 apply to this case. Note that the LAMP results predict peak temperatures and HF densities which are 20% and 70% higher, respectively, than the present calculations. This is considered to be a reasonable agreement in the light of the different kinetic rates and transport properties which may exist in two programs. Also, the present results calculate detailed and variable transport properties at each point in the flow; LAMP assumes constant Lewis and Prandtl numbers.

7.3 TEST CASE WITH HIGH CAVITY PRESSURE

7.3.1 Inlet Conditions

Finally one more test case whose inlet conditions were obtained from Bell Aerospace Corporation⁴⁴ was simulated. The inlet conditions, given in Fig. 35 are also used as the initial conditions. The velocities in both the streams are different now with H_2 stream being much faster than the previous cases. A slight discontinuity in pressure also exists at the inlet. The dimensions of the nozzle combinations are also different, they being about 1/3 of the previous cases (compare $h = .5$ cm before to $h = .157$ cm now). Test section for which calculations are made is fifteen heights (15 h's) long. Discontinuities in temperature, density, species density, u velocity besides the pressure are evident. Parallel mixing is again assumed.

The most striking difference here from the previous cases is the higher inlet pressure (5 torrs earlier to about 13 torrs now). Mixing due to diffusion is therefore slower and hence the lasing region is longer in terms of the nondimensional distance x/h .

7.3.2 Results and Discussion

The final steady state results for this case are plotted as 3-D surfaces. This gives a very clear picture of fluid dynamics and reaction mechanisms involved during the development of flow in both x and y directions. The x axis again is the flow direction and y axis represents the lateral direction. z axis is the thermodynamic quantity plotted for the figure. All such plots are made as seen from a viewing angle defined by $\theta = 60^\circ$ and $\phi = 240^\circ$ where θ and ϕ have the same notations as in spherical coordinate axes (i.e. θ is measured from z axis and ϕ from x axis in x,y plane) unless otherwise noted.

Figure 36 is such a plot of pressure. The pressure is seen to increase in flow direction slightly (about 40%), whereas in y direction it is almost the same. Even the slight discontinuity in pressure that exist at the inlet almost vanishes by the next grid point in axial direction. Note here that although both x and y are plotted on the same scale, x actually goes from 0 to 15 h whereas y goes from 0 to h. Figure 37 is a temperature surface. Again the rise in temperature due to heat release in the mixing region is evident. Again note that a temperature discontinuity at the inlet is fed in as part of the problem. The temperature rise at $x/h = 15$ and $y/h = .5$ for this case is 45%. Figure 38 represents the density (global) and u velocity surfaces respectively. Figures 39 and 40 are F_2 and H_2 surfaces for this case. The F_2 content in primary nozzle is zero whereas H_2 content in secondary nozzles is zero. At the inlet the F_2 and H_2 are present only in the secondary and primary nozzles, respectively. As the flow moves downstream they diffuse into each other. Some of the diffused species combine to form HF. Figures 39, 40 and 41 - which is a rotated view of the same H_2 surface shown for a better clarity with $\theta = 60^\circ$ but $\phi = 150^\circ$ - clearly show the depleted F_2 and H_2 inside the mixing region, which have gone to form HF. Figures 42, 43 and 44 are the surfaces for vibrational levels HF(0), HF(1) and HF(2) respectively. Although they are not plotted to the same scale in z, their qualitative behavior towards attaining a Boltzman distribution in vibrational levels at the local translational temperature is evident. HF(0) is rapidly increasing as the flow moves downstream whereas HF(2) is reaching an asymptotic value. Although population inversion exists for the first few heights downstream, the rapid V - V transitions populate then the lower levels (viz. 0 and 1) at the

expense of higher levels (viz. 1 and 2 respectively) in 2 - 1 and 1 - 0 V - V deactivations.

The small signal gain, averaged over height h is plotted in Fig. 45 and 46 for 1 - 0 and 2 - 1 transitions respectively. The values of averaged small signal gain calculated for this case are higher than the weakly reacting case discussed in Section 7.1 because the densities are higher now than in the previous case.

CHAPTER VIII

UNSTEADY FLOW

8.1 WEAKLY REACTING CASE

8.1.1 Inlet Conditions

The flows discussed so far have been steady although the transient states that the solution goes through are obviously unsteady. The time dependent Navier Stokes equations are used simply as a means to an end -- the asymptotically approached steady state. Nevertheless the equations are time dependent and can be used to obtain solutions for flow fields where inlet conditions are now varying in time¹⁹ unlike the previous cases where they were held fixed in time¹⁶⁻¹⁸. This is yet another of the inherent advantages in using the time dependent scheme to obtain a solution. Other finite difference schemes are steady state solutions and thus the time history of flow cannot be embedded in the solutions. Whereas, the time dependent Navier Stokes solutions naturally would incorporate this behavior in their solutions.

This inborn ability of time dependent equations precipitated a whole new line of simulation experiments wherein the inlet conditions were given sinusoidal (as well as sine square) variations and their simultaneous effects on mixing examined. The quasi-steady solution is obtained when a repetitive state in the whole flow field is established, i.e. when the variables were observed to repeat themselves after each periodic time of fluctuations. The main thrust of the work in the present chapter is to answer what happens if one (or more) of the variables at the inlet in one of the streams (or both streams) is fluctuated in time, does it enhance or inhibit mixing and how eventually does it affect gain?

The inlet conditions were fluctuated about certain mean conditions which, for the most part, were taken to be the same as those for the dilute case discussed in Section 7.1. Different variables fluctuated about these mean values are outlined in the next section.

The frequency of the oscillations was selected in such a way as to have wavelength of the order of cavity length, with velocity given by the faster stream speed. Further parametric studies confirmed this hypothesis. The Strouhal number is of the order recommended in Ref. 45. The frequency of fluctuation is of the order 10^5 rad/sec.

Figure 47 is a plot of sinusoidal variation in any of the variables. The time taken for sound waves to travel in y direction from the interface streamline to the Fluorine stream centerline and back was also calculated as shown in the same figure. The frequency so calculated from this periodic time is also of the order of 10^5 rad/sec.

8.1.2 Results and Discussion

Different variables were chosen to be fluctuated at the inlet with different frequencies and amplitudes and their effect on mixing analyzed. All of these simulation experiments are outlined below. Cold flow solutions were obtained first and if any improved mixing was observed then the hot flow calculations were turned on.

8.1.2a Pressure

Pressure was fluctuated in the F_2 stream about the mean value of 500 N/m^2 (and hence the density too since temperature was kept constant). This failed to yield any improved mixing. Any variation in frequency and/or amplitude of the pressure fluctuation did not improve this situation.

8.1.2b u Velocity

In order to vary in time, the momentum of the incoming flow, the x-component of velocity was fluctuated in F_2 stream about the mean value of 2000 m/sec.

Figure 48 is a plot of timewise variation of nondimensionalized density of F_2 at a point in the flow for various frequency-amplitude combinations. Solid straight lines indicate the density of F_2 at the same point for the case of steady mixing cold flows discussed in section 7.1 which is $(\rho_{F_2})_N = 0.117$. It can be seen as easily that the time averaged density of F_2 at this point is less than the steady state value. It should be noted here that these runs are made back-to-back, i.e. the results of one are used as initial conditions to start the next simulation experiment with the frequency or amplitude of fluctuation now changed to the new value at inlet. This resulted in considerable saving of computer time. Figure 49 indicates the same result for the case of angular velocity $\omega = \pi \times 10^5$ and $\Delta u = \pm 25\%$ of u_R which is then ± 500 m/sec. This rather large fluctuation at the sympathetic frequency resulted in increased mixing. The time averaged density of F_2 now is .144 compared to the steady state value of .117. The x wise variation of F_2 density is plotted in Fig. 50 for a particular y value of $y/h = 0.375$ for different phase angles of the sinusoidal oscillation at the inlet. A better overall mixing is quite evident from this graph. The bottom half of the same figure gives x-wise variation of pressure for the same case for phase angle $\theta = 0$, i.e. when inlet velocity is u_R . The marked variation in pressure for cold flows due to acceleration and deceleration of the flow is evident.

The values obtained at any phase angle are instantaneous and do not give a clear picture in terms of better or worse mixing. Therefore when the repetitive state was established, they were time averaged over a periodic time by using a special subroutine. These time averaged values are a more useful indicator of the trend.

Another case with $\omega = 0.5 \pi \times 10^5$ rad/sec and $\Delta u = \pm 25\%$ was also run. Time averaged values for F_2 density versus x for this case and the previous case are plotted in Fig. 51. The case with $\omega = .5 \pi \times 10^5$ rad/sec shows inferior mixing. This was again an indication that the angular velocity $\omega = \pi \times 10^5$ rad/sec was indeed in the desirable range.

Hot flow results were obtained for the case $\omega = \pi \times 10^5$ but with amplitude $\Delta u = \pm 10\%$. Time averaged results of various HF vibrational level densities are plotted in Fig. 52 and 53. Figure 52 shows lateral profiles where it is obvious that production of HF does not markedly differ from the one for steady flow. In fact they pretty much fall on top of each other. The x -wise variation of the same, shown in Fig. 53 also shows a very similar behavior. Indeed this suggests that fluctuations with moderate amplitude like $\Delta u = \pm 10\%$ do not depart from the steady state values noticeably, but rather substantial amplitudes like $\Delta u = \pm 25\%$ produce noticeable changes. This behavior can be explained by the nonlinearity associated with large perturbances, for small perturbations the increase and decrease in mixing being about the same and hence nullifying each other when time integrated over a period.

Figure 54 is a velocity vector diagram, to scale, at an instant described by phase angle $\theta = 90^\circ$ and case with $\omega = \pi \times 10^5$ rad/sec and $\Delta u = \pm 25\%$. Large components of velocity produced in y direction due to momentum interlinking can be seen. The flow, besides slowing down or

speeding up due to x momentum changes in incoming flow, is also bending in positive and negative y directions. This is obviously not observed much for the steady state mixing, inspite of the fact that both these cases are parallel mixing at the inlet. Thus the flow is observed to actually mix physically.

8.1.2c v Velocity

(I) Fluctuations in one stream- F_2 stream

Presence of rather large v velocity components in the flow field for the u velocity fluctuation case outlined above prompted simulation of v velocity fluctuations themselves at the inlet. It was v velocity components shown in Fig. 54 that were responsible for the material intermingling and so question was asked as to why not artificially introduce v velocity fluctuations about the parallel mixing (with zero v velocity in mean) at the inlet?

Therefore, all subsequent cases were run wherein only the sinusoidal variation of y component of velocity was intentionally forced at the inlet.

Figure 55 shows time wise variation of F_2 density again at a point in the flow field for three different amplitudes of $v = \pm 5\%$, $\pm 10\%$ and $\pm 25\%$ of the u_R . These cases were again run back to back, yielding a saving of a considerable computer time. Amplitudes of $\pm 5\%$ and $\pm 10\%$ again lead to F_2 densities less than or of the same order as the steady state value; whereas amplitude $\pm 25\%$ yielded larger densities. This case was therefore pursued further. Time averaged values of the F_2 density were obtained next for this cold flow and plotted versus x . Figure 51 shows the comparison between various cases. Faster mixing for F_2 and also H_2 is seen. For all the x wise location shown, F_2 density

there is higher than and H_2 density lower than all the other cases, showing a much superior mixing. Hot flow was next turned on at the cold flow repetitive state. Time averaged values were again obtained at the establishment of repetitive state. Figure 52 shows HF vibrational level profiles for a particular x location. Again a larger and more spread out production of HF is clearly seen for the present case compared to all the other cases plotted. Ability of the oscillations to populate the region of the flow for $y/h > 0.5$, which did not occur for the other two cases, in general produced integrated gain larger by almost a factor of two, thus making it possible to increase gain by a substantial amount. Figure 53 again shows HF levels versus x for various cases. Here again a faster mixing and faster pumping is clearly seen, particularly at $x/h = 2.5$.

Averaged small signal gain is plotted in Fig. 56 and 57 versus the non-dimensionalized x -wise location, for both the above mentioned unsteady case and the steady mixing case. These figures clearly illustrate the superiority of unsteady over steady mixing in terms of gain. Figure 56 shows averaged gain for transition levels 1 to 0 whereas Fig. 57 shows the same for levels 2 to 1, re-emphasizing the same point of factor of two higher obtainable gains. In both these cases the gain is calculated from the various HF level species densities averaged over a time period of an oscillation.

As a final comment on the fluid dynamic aspects of unsteady mixing, note that there is a physical improvement in mixing due to the forced intermingling of the fluid elements. This can be seen from Figs. 58a and b, which shows the time history of the inert particles inserted at two different times (and hence different phase angles) in the flow.

The nonuniform particle paths clearly show the extent of material intermingling. These path lines were obtained as part of the computer results by means of a special subroutine.

(II) Fluctuations in both streams

v velocity fluctuations so far have been only in one stream viz. F_2 stream. They were introduced now in both the streams at different phase difference (angle) between the two, to explore the possibility of further increased mixing. Figure 59 shows various simulation experiments attempted. The runs were again made back-to-back and all the cases were run for the same frequency. No substantially better mixing was observed over the case of fluctuations in one stream only. Phase differences tried were $\Delta\phi = 0, \pi/2$ and π for fluctuation of amplitude $v = \pm 10\%$ and $\pm 25\%$.

8.2 TEST CASE WITH HIGHER CAVITY PRESSURE

8.2.1 Inlet Conditions

The inlet conditions were the same again as the one described in Section 7.3.1 except that now the y component of velocity (v velocity) was sinusoidally fluctuated at various frequencies and amplitudes about a mean value of zero. Frequency was again selected such that the wavelength associated with the greatest u velocity at the inlet was of the same order as the distance from the inlet to the peak gain for steady flow case of Section 7.3.

8.2.2 Results and Discussion

Three different cases were simulated. They are (1) $\omega = 2\pi \times 10^5$ rad/sec and $v = \pm 25\%$, (2) $\omega = 2\pi \times 10^5$ rad/sec and $v = \pm 15\%$ and, (3) $\omega = 1.5\pi \times 10^5$ rad/sec and $v = \pm 15\%$. Of these, only the second case

is presented here since it yielded the best results. All these cases were run back to back with the final repetitive state values of previous case being the initial conditions for the next case. The steady state values of case in Section 7.3 were used to start case 1 mentioned above. This resulted in a considerable saving of computer time.

Figures 60 through 64 have been plotted for this case after the repetitive state has been established. They are the instantaneous values of various thermodynamic variables at two different phase angles of sinusoidal variations in v i.e. at $\delta = 0^\circ$ and 180° . Figure 60 (a) and (b) are pressure surfaces, at phase angles $\delta = 0$ and 180° respectively. Unlike the steady case, the pressure in y direction is not preserved at all due to v velocity fluctuations in the flow. Existence of propagating waves can also be seen. Figure 60(c) and (d) are the temperature surfaces corresponding to the same phase angles. Although the mean temperature rises as the flow moves downstream, the fluid dynamic coupling with v velocity causes slight waves in the surfaces. Figure 61(a), (b), (c) and (d) are such u velocity and v velocity surfaces. The v velocity surfaces throw more insight into the fluid dynamics of the flow. It should be noted here that the zero of z axis (v axis) has been moved for the purposes of plotting. The scale on z axis has also been considerably expanded. Figure 62 is a plot of HF(0) density surface for $\delta = 0^\circ$. Figure 63(a), (b), (c) and (d) are again such surfaces for HF(1) and HF(2) densities at different phase angles 0° and 180° . Again the tendency towards reaching a Boltzmann distribution at local temperature can also be seen. Figure 64 is just the same surface as in Figure 63(b) as viewed from a different viewing angle ($\theta = 60^\circ$ and $\phi = 150^\circ$).

The averaged values of small signal gain were also obtained and are plotted in Fig. 45 and 46 for 1 - 0 and 2 - 1 transitions respectively. They are plotted on the same graphs as steady case for comparison purposes. Again these values are the ones obtained from time averaged values of densities, temperature, pressure etc. over a periodic time. It can be seen that again the peak gains are higher by 5% to 40%. Faster mixing due to the unsteady intentional fluctuations are considered the cause for this increase.

CHAPTER IX

MISCELLANEOUS EXPERIMENTS

The parallel mixing flows in the steady flow cases discussed in Chapter 7 and for all cases other than v velocity fluctuation experiments in unsteady flow are idealizations of kinds where existence of boundary layers in the nozzles and regions of circulation in the base of the finite thickness for adjoining nozzles are neglected. This is done to provide actually the interim results in almost the same light as the cold flow results.

In real nozzles, though, boundary layers exist in velocity and temperature. If catalytic recombination is assumed at the nozzle walls, there is also a species density boundary layer in F and F_2 . Flow simulation with just the velocity boundary layer in both nozzles was attempted and solution outlined in the next section.

The nozzle lip shown in Fig. 1 is drawn to have no thickness. Of course in real nozzles this is not the case and a region of recirculation is present between primary (F_2) and secondary (H_2) nozzles. This is obviously a subsonic region embedded inside the mostly supersonic region existing in the flow field. The treatment for obtaining solution for this case is given in Section 9.2 although this was not successful.

9.1 BOUNDARY LAYER IN VELOCITY

The profile of the velocity boundary layer fed in at the inlet in both the primary and secondary streams is shown in Fig. 65(a). Velocity profiles for the cold flow at various x -wise locations are also shown on the same figure at the steady state. It can be seen that although

by $x/h = 1.25$ (first grid point location from the inlet) the velocity profile is jagged, it becomes quite smoothly varying by $x/h = 10$. This is to be expected since the velocity profile at the inlet has large gradients for $.25 < y/h < .75$. Fig. 65(b) shows pressure variation in the x direction for $y/h = 0.5$ for cold flow. The pressure decreases considerably as flow moves downstream for the first few grid points as the highly viscous flow expands to fill the region of near zero velocity (near the inlet) by accelerating. This causes a dip in pressure at $x/h = 1.25$ as shown in Fig. 65(b). The marked acceleration of the flow is also apparent by comparing velocity profiles at the inlet to that at $x/h = 1.25$ in Fig. 65(a). Fig. 65(c) is a time wise plot of temperature at three different points in the flow field. Broken lines denote the hot flow temperature variation which is started after the cold flow steady state at 61 non-dimensional time and continued until a hot flow steady state is reached at 100 n.d.t. The rise in temperature is again seen for $x/h = 5.0$ and 10.0 . There is no rise in temperature for $x/h = 1.25$ since hardly any HF has formed and no heat release has taken place. On the contrary temperature drops in value from 150°K at the inlet to 118°K as the flow is accelerating from zero velocity at inlet to a supersonic speed for $y/h = 0.5$.

Small signal gain (for zero power) were also calculated at the hot flow steady state. Figure 66 is a comparison for several cases for transition 2, $0 \rightarrow 1, 1$. This example indicates the adverse effect that the real effects a boundary layer has on the laser performance. Indeed the gain at $x/h = 1.25$ is even zero for this case whereas for all the other three cases drawn it is positive although rather small. Boundary layer profiles in velocity are thus found to impede small signal

gain, a result that is to be expected. Boundary layers in temperature and species density are expected to further reduce gain and adversely affect the laser performance.

9.2 BASE FLOW

The other real effect taken into account is the finite thickness of nozzle lip at inlet. Figure 67 shows such a base of small thickness. Inlet conditions then are simply boundary layer profiles in velocity in the primary and secondary streams and no slip conditions at the base i.e. zero velocity (both u and v).

A cold flow solution was attempted with such inlet conditions but the final steady state was not achieved. The program "blew up" (e.g. pressure or temperature went negative) before this could be realized.

The inlet conditions were next changed to an arbitrary smooth velocity profile at the beginning of solution and then changed gradually to a profile which is similar but not quite the same as the actual (real life) velocity profile. This procedure yielded transient results which showed formation of vortices in the base region of the flow. The solution could, this way, be advanced much farther, by slowly "creeping up" on the discontinuous velocity profile at the inlet, but no steady state values were still obtained. The pressure again went very small and finally negative in the base region.

It was, therefore, concluded that substituting of initial conditions everywhere in the flow, which are close to what might be expected at steady state, might work. No further attempt was made to calculate such conditions due to lack of time. It should be emphasized here that the initial conditions should be such that the downstream end of the flow field regime is completely supersonic or goes and remains supersonic soon after the start of the solution.

CHAPTER X

CONCLUSIONS AND RECOMMENDATIONS

The work presented herein introduces a "third generation" of chemical laser analysis, i.e., Navier-Stokes solutions for the flow field coupled with the detailed chemical kinetics for both the hot and cold reactions of HF for both steady and unsteady flows. In particular, the present results show the following:

1. Navier Stokes solutions for supersonic diffusion chemical lasers are indeed feasible; however, computer times equivalent to about 30 minutes or longer on a UNIVAC 1108 are required for a single case. By stacking cases back-to-back such that the initial conditions for one are obtained from the solution of another, the net time per case can be substantially reduced.

2. The major potential for such Navier-Stokes solutions is in the analysis of recirculation zone and separated flow effects on laser performance for real nozzles with finite base width at the inlet.

3. A differencing scheme wherein the forward and backward differences are combined in the manner described as "modified MacCormack" yield the best results. This method is therefore recommended over other differencing schemes.

4. In a comparison between hot and cold flows, the chemical reactions markedly affect the temperature distributions, but have little effect on velocity distributions. The pressure increases in the flow direction due to chemical reactions, an effect to be expected from simple analogy with constant area heat addition in supersonic flows. In contrast,

for cold flows, the longitudinal variation is reasonably constant and may even decrease slightly.

5. The growth of the laminar mixing reaction zone compares favorably with experiment.

6. Navier Stokes calculations have the distinct advantage that the two dimensional pressure gradients (in both x and y directions) appear quite naturally and exactly. In strongly reacting cases, the proper accounting of these pressure gradients are absolutely necessary; the constant pressure boundary layer assumption is not adequate.

7. Considering the differences between the physical properties and fluid dynamic modeling of the present Navier Stokes analysis and LAMP, fairly reasonable agreement is obtained between the two. The constant pressure results of King and Mirels differ considerably since the boundary conditions are quite different. In real life chemical lasers, pressure gradients in x directions play a very important role -- a fact accounted for by the present program as well as by LAMP, which is probably one of the most versatile of the chemical laser codes.

8. It is the first numerical solution of the full Navier Stokes equations with fully coupled kinetics for both the cold and hot reactions for HF and multicomponent diffusion for the case of inherently unsteady supersonic mixing flows.

9. One of the intrinsic advantages of time dependent solution is its ability to obtain solutions for mixing flows with unsteady conditions at the inlet. This cannot be achieved by a program which uses finite difference schemes but is time independent; in other words a steady state formulation.

10. It shows that the averaged gain for HF chemical lasers can be increased substantially by intentionally fluctuating the y-component of velocity at the inlet. This leads to better mixing and also higher gain in general.

11. Unsteady mixing is especially important for chemical lasers with higher cavity pressures (of order 15 - 30 torrs or higher) wherein molecular diffusion mixing is less important and some external means of achieving faster mixing is necessary. In fact for such lasers a trip nozzle flow near the inlet has yielded⁴⁴ two to three times higher power results. This is attributed to the unsteadiness apparently present due to the vortices generated by the trip nozzles.

12. The presence of a velocity boundary layer at the inlet impedes mixing and hence reduce integral gain.

APPENDIX A

$$\begin{aligned}
 \frac{d[F]}{dt} = & 2\{k_{1a}[F_2][M_1] - k_{-1a}[F]^2[M_1] + k_{1b}[F_2][M_2] - k_{-1a}[F]^2[M_2]\} \\
 & + \{k_{30}[HF(0)] + k_{31}[HF(1)] + k_{32}[HF(2)] + k_{33}[HF(3)] \\
 & + k_{34}[HF(4)] + k_{35}[HF(5)] + k_{36}[HF(6)] + k_{37}[HF(7)] + k_{38}[HF(8)]\} \\
 & \cdot \{[M_6]\} + \{-k_{-30} - k_{-31} - k_{-32} - k_{-33} - k_{-34} - k_{-35} - k_{-36} - k_{-37} - k_{-38}\} \\
 & \{[H][F][M_6]\} + \{3k_{-4a0}[HF(0)] + 3k_{-4a}[HF(1)] + 3k_{-4b}[HF(2)] \\
 & + 3k_{-4c}[HF(3)] + k_{-4d}[HF(4)] + k_{-4e}[HF(5)] + k_{-4f}[HF(6)]\} \{[H]\} \\
 & + \{-k_{4a0} - k_{4a} - k_{4b} - k_{4c}\} \{[F][H_2]\} + \{k_{5a} + k_{5b} + k_{5c} + k_{5d} + k_{5e} \\
 & + k_{5f} + k_{5g} + k_{5h} + k_{5i}\} \{[H][F_2]\} + \{-k_{-5a}[HF(0)] - k_{-5b}[HF(1)] \\
 & - k_{-5c}[HF(2)] - k_{-5d}[HF(3)] - k_{-5e}[HF(4)] - k_{-5f}[HF(5)] \\
 & - k_{-5g}[HF(6)] - k_{-5h}[HF(7)] - k_{-5i}[HF(8)]\} \{[F]\}
 \end{aligned}$$

$$\frac{d[H_e]}{dt} = 0$$

$$\begin{aligned}
\frac{d[H]}{dt} = & 2\{k_{2a}[M_3] + k_{2b}[M_4] + k_{2c}[M_5]\}\{[H_2]\} + 2\{-k_{2a}[M_3] \\
& - k_{2b}[M_4] - k_{2c}[M_5]\}\{[H]^2\} + \{k_{30}[HF(0)] + k_{31}[HF(1)] \\
& + k_{32}[HF(2)] + k_{33}[HF(3)] + k_{34}[HF(4)] + k_{35}[HF(5)] + k_{36}[HF(6)] \\
& + k_{37}[HF(7)] + k_{38}[HF(8)]\}\{[M_6]\} + \{-k_{30} - k_{31} - k_{32} - k_{33} \\
& - k_{34} - k_{35} - k_{36} - k_{37} - k_{38}\}\{[H][F][M_6]\} + \{k_{4a0} + k_{4a} + k_{4b} \\
& + k_{4c}\}\{[F][H_2]\} + \{-3k_{4a0}[HF(0)] - 3k_{4a}[HF(1)] - 3k_{4b}[HF(2)] \\
& - 3k_{4c}[HF(3)] - k_{4d}[HF(4)] - k_{4e}[HF(5)] - k_{4f}[HF(6)]\}\{[H]\} \\
& + \{k_{5a}[HF(0)] + k_{5b}[HF(1)] + k_{5c}[HF(2)] + k_{5d}[HF(3)] \\
& + k_{5e}[HF(4)] + k_{5f}[HF(5)] + k_{5g}[HF(6)] + k_{5h}[HF(7)] \\
& + k_{5i}[HF(8)]\}\{[F]\} + \{-k_{5a} - k_{5b} - k_{5c} - k_{5d} - k_{5e} - k_{5f} - k_{5g} \\
& - k_{5h} - k_{5i}\}\{[H][F_2]\}
\end{aligned}$$

$$\begin{aligned}
\frac{d[F_2]}{dt} &= \{k_{-1a}[M_1] + k_{-1b}[M_2]\}[F]^2 + \{-k_{1a}[M_1] - k_{1b}[M_2]\}[F_2] \\
&+ \{k_{-5a}[HF(0)] + k_{-5b}[HF(1)] + k_{-5c}[HF(2)] + k_{-5d}[HF(3)] \\
&+ k_{-5e}[HF(4)] + k_{-5f}[HF(5)] + k_{-5g}[HF(6)] + k_{-5h}[HF(7)] \\
&+ k_{-5i}[HF(8)]\}[F] + \{-k_{5a} - k_{5b} - k_{5c} - k_{5d} - k_{5e} - k_{5f} - k_{5g} \\
&- k_{5h} - k_{5i}\}[H][F_2]
\end{aligned}$$

$$\begin{aligned}
\frac{d[H_2]}{dt} &= \{k_{-2a}[M_3] + k_{-2b}[M_4] + k_{-2c}[M_5]\}[H]^2 + \{-k_{2a}[M_5] - k_{2b}[M_4] \\
&- k_{2c}[M_5]\}[H_2] + \{3k_{-4a0}[HF(0)] + 3k_{-4a}[HF(1)] \\
&+ 3k_{-4b}[HF(1)] + 3k_{-4c}[HF(3)] + k_{-4d}[HF(4)] + k_{-4e}[HF(5)] \\
&+ k_{-4f}[HF(6)]\}[H] + \{-k_{4a0} - k_{4a} - k_{4b} - k_{4c}\}[F][H_2]
\end{aligned}$$

$$\begin{aligned}
\frac{d[\text{HF}(0)]}{dt} = & \{k_{-30}[\text{H}][\text{F}] - k_{30}[\text{HF}(0)]\}[M_6] + \{k_{4a0}[\text{F}][\text{H}_2] \\
& - 3 k_{-4a0}[\text{HF}(0)][\text{H}]\} + \{k_{5a}[\text{H}][\text{F}_2] - k_{-5a}[\text{HF}(0)][\text{F}]\} \\
& + \{k_{6a1}[\text{HF}(1)] - k_{-6a1}[\text{HF}(0)]\}[M_7] + \{k_{6b1}[\text{HF}(1)] \\
& - k_{-6b1}[\text{HF}(0)]\}[M_8] + \{k_{6c1}[\text{HF}(1)] - k_{-6c1}[\text{HF}(0)]\}[M_9] \\
& + \{k_{6d1}[\text{HF}(1)] - k_{-6d1}[\text{HF}(0)]\}[M_{10}] + \{k_{6f1}[\text{HF}(1)] \\
& - k_{-6f1}[\text{HF}(0)]\}[M_5] + \{k_{6g1}[\text{HF}(1)] - k_{-6g1}[\text{HF}(0)]\}[M_4] \\
& + \{k_{7a}[\text{HF}(1)]^2 - k_{-7a1}[\text{HF}(0)][\text{HF}(2)]\} + \{k_{7b}[\text{HF}(1)][\text{HF}(2)] \\
& - k_{-7b1}[\text{HF}(0)][\text{HF}(3)]\} + \{k_{7c}[\text{HF}(1)][\text{HF}(3)] - k_{-7c1}[\text{HF}(0)] \cdot \\
& \cdot [\text{HF}(4)]\} + \{k_{7d}[\text{HF}(1)][\text{HF}(4)] - k_{-7d1}[\text{HF}(0)][\text{HF}(5)]\}
\end{aligned}$$

$$\begin{aligned}
\frac{d[\text{HF}(2)]}{dt} &= \{k_{-32}[\text{H}][\text{F}] - k_{32}[\text{HF}(2)]\}[\text{M}_6] + \{k_{4b}[\text{F}][\text{H}_2] - 3k_{-4b}[\text{HF}(2)][\text{H}]\} \\
&+ \{k_{5c}[\text{H}][\text{F}_2] - k_{-5c}[\text{HF}(2)][\text{F}]\} + \{k_{-6a2}[\text{HF}(1)] - k_{6a2}[\text{HF}(2)] \\
&+ k_{6a3}[\text{HF}(3)] - k_{-6a3}[\text{HF}(2)]\}[\text{M}_7] + \{k_{-6b2}[\text{HF}(1)] \\
&- k_{6b2}[\text{HF}(2)] + k_{6b3}[\text{HF}(3)] - k_{-6b3}[\text{HF}(2)]\}[\text{M}_8] + \{k_{-6c2}[\text{HF}(1)] \\
&- k_{6c2}[\text{HF}(2)] + k_{6c3}[\text{HF}(3)] - k_{-6c3}[\text{HF}(2)]\}[\text{M}_9] + \{k_{-6d2}[\text{HF}(1)] \\
&- k_{6d2}[\text{HF}(2)] + k_{6d3}[\text{HF}(3)] - k_{-6d3}[\text{HF}(2)]\}[\text{M}_{10}] + \{k_{-6f2}[\text{HF}(1)] \\
&- k_{6f2}[\text{HF}(2)] + k_{6f3}[\text{HF}(3)] - k_{-6f3}[\text{HF}(2)]\}[\text{M}_5] + \{k_{-6g2}[\text{HF}(1)] \\
&- k_{6g2}[\text{HF}(2)] + k_{6g3}[\text{HF}(3)] - k_{-6g3}[\text{HF}(2)]\}[\text{M}_4] + \\
&+ k_{7a}\{[\text{HF}(1)]^2 + [\text{HF}(3)]^2 - 2[\text{HF}(2)]^2\} + k_{7b}\{-[\text{HF}(1)] \cdot \\
&\cdot [\text{HF}(2)] - [\text{HF}(2)\text{HF}(3)] + [\text{HF}(3)\text{HF}(4)]\} + \{k_{-7c2}[\text{HF}(1)\text{HF}(5)]
\end{aligned}$$

$$- k_{7c}[\text{HF}(2)\text{HF}(4)] + k_{7c}[\text{HF}(3)\text{HF}(5)] - k_{7c3}[\text{HF}(2)\text{HF}(6)]\}$$

$$+ \{k_{7d2}[\text{HF}(1)\text{HF}(6)] - k_{7d}[\text{HF}(2)\text{HF}(5)]\}$$

$$+ k_{7d}[\text{HF}(3)\text{HF}(6)] - k_{7d3}[\text{HF}(2)\text{HF}(7)]\}$$

$$\frac{d[\text{HF}(3)]}{dt} = \{k_{-33}[\text{H}][\text{F}] - k_{33}[\text{HF}(3)]\}[M_6] + \{k_{4c}[\text{F}][\text{H}_2] - 3k_{-4c}[\text{HF}(3)] \cdot$$

$$\cdot [\text{H}]\} + \{k_{54}[\text{H}][\text{F}_2] - k_{-54}[\text{HF}(3)][\text{F}]\} + \{k_{-6a3}[\text{HF}(2)]$$

$$- k_{6a3}[\text{HF}(3)] + k_{6a4}[\text{HF}(4)] - k_{-6a4}[\text{HF}(3)]\}[M_7] + \{k_{-6b3}[\text{HF}(2)]$$

$$- k_{6b3}[\text{HF}(3)] + k_{6b4}[\text{HF}(4)] - k_{-6b4}[\text{HF}(3)]\}[M_8] + \{k_{-6c3}[\text{HF}(2)]$$

$$- k_{6c3}[\text{HF}(3)] + k_{6c4}[\text{HF}(4)] - k_{-6c4}[\text{HF}(3)]\}[M_9] + \{k_{-6d3}[\text{HF}(2)]$$

$$- k_{6d3}[\text{HF}(3)] + k_{6d4}[\text{HF}(4)] - k_{-6d4}[\text{HF}(3)]\}[M_{10}] + \{k_{-6f3}[\text{HF}(2)]$$

$$- k_{6f3}[\text{HF}(3)] + k_{6f4}[\text{HF}(4)] - k_{-6f4}[\text{HF}(3)]\}[M_5] + \{k_{-6g3}[\text{HF}(2)]$$

$$- k_{6g3}[\text{HF}(3)] + k_{6g4}[\text{HF}(4)] - k_{-6g4}[\text{HF}(3)]\}[M_4] + k_{7a}\{[\text{HF}(2)]^2$$

$$- 2[\text{HF}(3)]^2 + [\text{HF}(4)]^2\} - k_{7a2}[\text{HF}(1)\text{HF}(3)] + k_{-7a3}[\text{HF}(2)\text{HF}(4)]$$

$$\begin{aligned}
& -k_{-7a4}[\text{HF}(3)\text{HF}(5)] + k_{7b} \{ [\text{HF}(1)][\text{HF}(2)] - [\text{HF}(2)\text{HF}(3)] \\
& - [\text{HF}(3)\text{HF}(4)] + [\text{HF}(4)\text{HF}(5)] \} - k_{-7b1} [\text{HF}(0)\text{HF}(3)] \\
& + k_{-7b2} [\text{HF}(1)\text{HF}(4)] + k_{-7b3} [\text{HF}(2)\text{HF}(5)] - k_{-7b4} [\text{HF}(3)\text{HF}(6)] \} \\
& + k_{7c} \{ -[\text{HF}(1)\text{HF}(3)] - [\text{HF}(3)\text{HF}(5)] + [\text{HF}(4)\text{HF}(6)] \} \\
& + k_{-7c1} [\text{HF}(0)\text{HF}(4)] + k_{-7c3} [\text{HF}(2)\text{HF}(6)] - k_{-7c4} [\text{HF}(3)\text{HF}(7)] \} \\
& + k_{7d} \{ -[\text{HF}(3)\text{HF}(6)] + [\text{HF}(4)\text{HF}(7)] \} + k_{-7d3} [\text{HF}(2)\text{HF}(7)] \\
& - k_{-7d4} [\text{HF}(3)\text{HF}(8)] \}
\end{aligned}$$

$$\begin{aligned}
\frac{d[\text{HF}(4)]}{dt} & = \{ k_{-34} [\text{H}][\text{F}] - k_{34} [\text{HF}(4)] \} [\text{M}_6] + \{ -[7.4 \times 10^{12} \exp(-500/\text{RT})] \cdot \\
& \cdot \text{HF}(4)] [\text{H}] \} + \{ k_{55} [\text{H}][\text{F}_2] - k_{-55} [\text{HF}(4)][\text{F}] \} + \{ k_{-6a4} \text{HF}(3) - k_{6a4} \text{HF}(4) \\
& + k_{6a5} \text{HF}(5) - k_{-6a5} \text{HF}(4) \} [\text{M}_7] + \{ k_{-6b4} \text{HF}(3) - k_{6b4} \text{HF}(4) \\
& + k_{6b5} \text{HF}(5) - k_{-6b5} \text{HF}(4) \} [\text{M}_8] + \{ k_{-6c4} \text{HF}(3) - k_{6c4} \text{HF}(4) + k_{6c5} \text{HF}(5) \\
& - k_{-6c5} \text{HF}(4) \} [\text{M}_9] + \{ k_{-6d4} \text{HF}(3) - k_{6d4} \text{HF}(4) + k_{6d5} \text{HF}(5) - k_{-6d5} \text{HF}(4) \} \\
& \cdot [\text{M}_{10}] + \{ k_{-6f4} \text{HF}(3) - k_{6f4} \text{HF}(4) + k_{6f5} \text{HF}(5) - k_{-6f5} \text{HF}(4) \} [\text{M}_5]
\end{aligned}$$

$$\begin{aligned}
& + \{k_{-6g4}HF(3) - k_{6g4}HF(4) + k_{6g5}HF(5) - k_{-6g5}HF(4)\}[M_4] \\
& + k_{7a}\{[HF(3)]^2 - 2[HF(4)]^2 + [HF(5)]^2\} - k_{-7a3}[HF(2)HF(4)] \\
& + 2k_{-7a4}[HF(3)HF(5)] - k_{-7a5}[HF(4)HF(6)]\} + k_{7b}\{[HF(2)HF(3)] \\
& - [HF(3)][HF(4)] - [HF(4)HF(5)] + [HF(5)HF(6)]\} - k_{-7b2}[HF(1) \cdot \\
& \cdot HF(4)] + k_{-7b3}[HF(2)HF(5)] + k_{-7b4}[HF(3)HF(6)] - k_{-7b5}[HF(4)HF(7)]\} \\
& + k_{7c}\{[HF(1)HF(3)] - [HF(2)HF(4)] - [HF(4)HF(6)] \\
& + [HF(5)HF(7)]\} - k_{-7c1}[HF(0)HF(4)] + k_{-7c2}[HF(1)HF(5)] \\
& + k_{-7c4}[HF(3)HF(7)] - k_{-7c5}[HF(4)HF(8)]\} + k_{7d}\{-[HF(1)HF(4)] \\
& - [HF(4)HF(7)]\} + k_{-7d1}[HF(0)HF(5)] + k_{-7d4}[HF(3)HF(8)]
\end{aligned}$$

$$\begin{aligned}
\frac{d[\text{HF}(5)]}{dt} &= \{k_{-35}[\text{H}][\text{F}] - k_{35}[\text{HF}(5)]\}[\text{M}_6] + \{-[1.1 \times 10^{13} \exp(-510/RT)] \cdot \\
&\cdot [\text{HF}(5)][\text{H}]\} + \{k_{56}[\text{H}][\text{F}_2] - k_{-56}[\text{HF}(5)][\text{F}]\} + \{k_{-6a5}[\text{HF}(4)] \\
&- k_{6a5}[\text{HF}(5)] + k_{6a6}[\text{HF}(6)] - k_{-6a6}[\text{HF}(5)]\}[\text{M}_7] + k_{-6b5}[\text{HF}(4)] \\
&- k_{+6b5}[\text{HF}(5)] + k_{6b6}[\text{HF}(6)] - k_{-6b6}[\text{HF}(5)]\}[\text{M}_8] + \{k_{-6c5}[\text{HF}(4)] \\
&- k_{6c5}[\text{HF}(5)] + k_{6c6}[\text{HF}(6)] - k_{-6c6}[\text{HF}(5)]\}[\text{M}_9] + \{k_{-6d5}[\text{HF}(4)] \\
&- k_{+6d5}[\text{HF}(5)] + k_{6d6}[\text{HF}(6)] - k_{-6d6}[\text{HF}(5)]\}[\text{M}_{10}] + \{k_{-6f5}[\text{HF}(4)] \\
&- k_{6f5}[\text{HF}(5)] + k_{6f6}[\text{HF}(6)] - k_{-6f6}[\text{HF}(5)]\}[\text{M}_5] + \{k_{-6g5}[\text{HF}(4)] \\
&- k_{6g5}[\text{HF}(5)] + k_{6g6}[\text{HF}(6)] - k_{-6g6}[\text{HF}(5)]\}[\text{M}_4] + k_{7a}[\text{HF}(4)]^2 \\
&- 2[\text{HF}(5)]^2 + [\text{HF}(6)]^2\} - k_{-7a4}[\text{HF}(3)\text{HF}(5)] + 2k_{-7a5}[\text{HF}(4)\text{HF}(6)] \\
&- k_{-7a6}[\text{HF}(5)\text{HF}(7)] + [k_{7b}[\text{HF}(3)\text{HF}(4)] - [\text{HF}(4)\text{HF}(5)] \\
&- [\text{HF}(5)\text{HF}(6)] + [\text{HF}(6)\text{HF}(7)]] - k_{-7b3}[\text{HF}(2)\text{HF}(5)] \\
&+ k_{-7b4}[\text{HF}(3)\text{HF}(6)] + k_{-7b5}[\text{HF}(4)\text{HF}(7)] - k_{-7b6}[\text{HF}(5)\text{HF}(8)] \\
&+ k_{7c}[\text{HF}(2)\text{HF}(4)] - [\text{HF}(3)\text{HF}(5)] - [\text{HF}(5)\text{HF}(7)]\}
\end{aligned}$$

$$\begin{aligned}
& - k_{-7c2}[\text{HF}(1)\text{HF}(5)] + k_{-7c3}[\text{HF}(2)\text{HF}(6)] + k_{-7c5}[\text{HF}(4)\text{HF}(8)] \\
& + k_{7d}\{[\text{HF}(1)\text{HF}(4)] - [\text{HF}(2)\text{HF}(5)]\} - k_{-7d1}[\text{HF}(0)\text{HF}(5)] \\
& + k_{-7d2}[\text{HF}(1)\text{HF}(6)]
\end{aligned}$$

$$\begin{aligned}
\frac{d[\text{HF}(6)]}{dt} & = \{k_{-36}[\text{H}][\text{F}] - k_{36}[\text{HF}(6)]\}[\text{M}_6] + \{-[1.9 \times 10^{13} \exp(-566/\text{RT})] \cdot \\
& \cdot [\text{HF}(6)][\text{H}]\} + \{k_{57}[\text{H}][\text{F}_2] - k_{-57}[\text{HF}(6)][\text{F}]\} + \{k_{-6a6}^{\text{HF}(5)} \\
& - k_{6a6}^{\text{HF}(6)} + k_{6a7}^{\text{HF}(7)} - k_{-6a7}^{\text{HF}(6)}\}[\text{M}_7] + \{k_{-6b6}^{\text{HF}(5)} \\
& - k_{6b6}^{\text{HF}(6)} + k_{6b7}^{\text{HF}(7)} - k_{-6b7}^{\text{HF}(6)}\}[\text{M}_8] + \{k_{-6c6}^{\text{HF}(5)} \\
& - k_{6c6}^{\text{HF}(6)} + k_{6c7}^{\text{HF}(7)} - k_{-6c7}^{\text{HF}(6)}\}[\text{M}_9] + \{k_{-6d6}^{\text{HF}(5)} \\
& - k_{6d6}^{\text{HF}(6)} + k_{6d7}^{\text{HF}(7)} - k_{-6d7}^{\text{HF}(6)}\}[\text{M}_{10}] + \{k_{-6f6}^{\text{HF}(5)} \\
& - k_{6f6}^{\text{HF}(6)} + k_{6f7}^{\text{HF}(7)} - k_{-6f7}^{\text{HF}(6)}\}[\text{M}_5] + \{k_{-6g6}^{\text{HF}(5)} \\
& - k_{6g6}^{\text{HF}(6)} + k_{6g7}^{\text{HF}(7)} - k_{-6g7}^{\text{HF}(6)}\}[\text{M}_4] + [k_{7a}\{[\text{HF}(5)]^2 \\
& - 2[\text{HF}(6)]^2 + [\text{HF}(7)]^2\} - k_{-7a5}[\text{HF}(4)\text{HF}(6)] + 2k_{-7a6}[\text{HF}(5) \cdot \\
& \cdot \text{HF}(7)] - k_{-7a7}[\text{HF}(6)\text{HF}(8)] + k_{7b}\{[\text{HF}(4)\text{HF}(5)]
\end{aligned}$$

$$\begin{aligned}
& - [\text{HF}(5)\text{HF}(6)] - [\text{HF}(6)\text{HF}(7)] - k_{-7b4}[\text{HF}(3)\text{HF}(6)] \\
& + k_{-7b5}[\text{HF}(4)\text{HF}(7)] + k_{-7b6}[\text{HF}(5)\text{HF}(8)] + k_{7c}[\text{HF}(3)\text{HF}(5)] \\
& - [\text{HF}(4)\text{HF}(6)] - k_{-7c3}[\text{HF}(2)\text{HF}(6)] + k_{-7c4}[\text{HF}(3)\text{HF}(7)] \\
& + k_{7d}[\text{HF}(2)\text{HF}(5) - \text{HF}(3)\text{HF}(6)] - k_{-7d2}[\text{HF}(1)\text{HF}(6)] \\
& + k_{-7d3}[\text{HF}(2)\text{HF}(7)]
\end{aligned}$$

$$\begin{aligned}
\frac{d[\text{HF}(7)]}{dt} & = \{k_{-37}[\text{H}][\text{F}] - k_{37}[\text{HF}(7)]\}[\text{M}_6] + \{k_{58}[\text{H}][\text{F}_2] - k_{-58}[\text{HF}(7)][\text{F}]\} \\
& + \{k_{-6a7}[\text{HF}(6)] - k_{6a7}[\text{HF}(7)] + k_{6a8}[\text{HF}(8)] - k_{-6a8}[\text{HF}(7)]\}[\text{M}_7] \\
& + \{k_{-6b7}[\text{HF}(6)] - k_{6b7}[\text{HF}(7)] + k_{6b8}[\text{HF}(8)] - k_{-6b8}[\text{HF}(7)]\}[\text{M}_8] \\
& + \{k_{-6c7}[\text{HF}(6)] - k_{6c7}[\text{HF}(7)] + k_{+6c8}[\text{HF}(8)] - k_{-6c8}[\text{HF}(7)]\}[\text{M}_9] \\
& + \{k_{-6d7}[\text{HF}(6)] - k_{6d7}[\text{HF}(7)] + k_{+6d8}[\text{HF}(8)] - k_{-6d8}[\text{HF}(7)]\}[\text{M}_{10}] \\
& + \{k_{-6f7}[\text{HF}(6)] - k_{6f7}[\text{HF}(7)] + k_{6f8}[\text{HF}(8)] - k_{-6f8}[\text{HF}(7)]\}[\text{M}_5] \\
& + \{k_{-6g7}[\text{HF}(6)] - k_{6g7}[\text{HF}(7)] + k_{6g8}[\text{HF}(8)] - k_{-6g8}[\text{HF}(7)]\}[\text{M}_4]
\end{aligned}$$

$$\begin{aligned}
& + k_{7a} \{ [HF(6)]^2 - 2[HF(7)]^2 \} - k_{-7a6} [HF(5)HF(7)] \\
& + 2 k_{-7a7} [HF(6)HF(8)] + k_{7b} \{ [HF(5)HF(6)] - [HF(6)HF(7)] \} \\
& + k_{-7b6} [HF(5)HF(8)] - k_{-7b5} [HF(4)HF(7)] + k_{7c} \{ [HF(4)HF(6)] \\
& - [HF(5)HF(7)] \} - k_{-7c4} [HF(3)HF(7)] + k_{-7c5} [HF(4)HF(8)] \\
& + k_{7d} \{ [HF(3)HF(6)] - [HF(4)HF(7)] \} - k_{-7d3} [HF(2)HF(7)] \\
& + k_{-7d4} [HF(3)HF(8)]
\end{aligned}$$

$$\begin{aligned}
\frac{d[HF(8)]}{dt} & = \{ k_{-38} [H][F] - k_{38} [HF(8)] \} [M_6] + k_{59} [H][F_2] \\
& - k_{-59} [HF(8)][F] + \{ k_{-6a8} HF(7) - k_{6a8} HF(8) \} [M_7] \\
& + \{ k_{-6b8} HF(7) - k_{6b8} HF(8) \} [M_8] + \{ k_{-6c8} HF(7) - k_{6c8} HF(8) \} [M_9] \\
& + \{ k_{-6d8} HF(7) - k_{6d8} HF(8) \} [M_{10}] + \{ k_{-6f8} HF(7) - k_{6f8} HF(8) \} \cdot \\
& \cdot [M_5] + \{ k_{-6g8} HF(7) - k_{6g8} HF(8) \} [M_4] + \{ k_{7a} [HF(7)]^2 \\
& - k_{-7a7} HF(6)HF(8) \} + k_{7b} HF(6)HF(7) - k_{-7b6} HF(5)HF(8)
\end{aligned}$$

$$\begin{aligned}
 &+ k_{7c} [\text{HF}(5)\text{HF}(7)] - k_{-7c5} \text{HF}(4)\text{HF}(8) + k_{7d} \text{HF}(4)\text{HF}(7) \\
 &- k_{-7d4} \text{HF}(3)\text{HF}(8)
 \end{aligned}$$

The vectors \hat{e} and \hat{f} are spatial derivatives of concentration and velocity, respectively, and are approximated by finite differences. The factor $\text{HF}(i)$ is the local concentration of species i and is taken to vary as the position (x, y, z) . The approximation of the derivatives involves the use of a stencil of points around the point of interest. The stencil is chosen to be symmetric and to include all points that are adjacent to the point of interest.

In the equations above, forward, backward, and central differences are used. The notation \hat{e}_x indicates a derivative in the x direction. The notation \hat{e}_y indicates a derivative in the y direction. The notation \hat{e}_z indicates a derivative in the z direction.

Let i represent the number of grid cells in the x direction and j represent the number of grid cells in the y direction. Let x and y are the coordinates of the grid cells. Let k denote the number of the component of vectors \hat{e} , \hat{f} , \hat{g} or \hat{h} as written on pp. 18-21.

Let $i = 1, 2, \dots, N_x$ and $j = 1, 2, \dots, N_y$
 when $i = 1$

$$\hat{e}_x(i, j, k) = \frac{e_x(i+1, j, k) - e_x(i-1, j, k)}{2\Delta x} \quad (16-1)$$

and when $i = N_x$

$$\hat{e}_x(i, j, k) = \frac{e_x(i, j, k) - e_x(i-1, j, k)}{\Delta x} \quad (16-2)$$

Similarly for \hat{e}_y when $j = 1$ or $j = N_y$.

APPENDIX B

VARIOUS DIFFERENCING SCHEMES

The vectors \bar{F} and \bar{G} contain spatial derivatives of temperature and velocities directly and of species densities indirectly through the diffusion velocities. Spatial gradients of vectors \bar{F} and \bar{G} need to be taken in turn to solve equations (58) and (59). Thus effectively spatial gradients of the thermodynamic quantities need to be taken to a largest order of two. This offers various combinations of forward, backward and central differencing schemes to compute the spatial derivatives.

At the boundaries where forward, backward or central differencing scheme may not be applicable a three point forward or backward scheme was used as the case may be. e.g.

Let i represent the number of x wise grid and j represent the number of y wise grid where x and y are the coordinate axes as shown in Fig. 1. k denotes the number of the component of vectors \bar{U} , \bar{F} , \bar{G} or \bar{K} as written on pp. 18-21.

Let $i = 1, 2, 3, \dots, IT$ and $j = 1, 2, 3, \dots, JT$
 when $i = 1$

$$\frac{\partial \bar{F}}{\partial x}(1, j, k) = \frac{4 \times \bar{F}(2, j, k) - 3 \times \bar{F}(1, j, k) - \bar{F}(3, j, k)}{2 \Delta x} \quad (B-1)$$

and when $i = IT$

$$\frac{\partial \bar{F}}{\partial x}(IT, j, k) = - \frac{4 \times \bar{F}(IT-1, j, k) - 3 \times \bar{F}(IT, j, k) - \bar{F}(IT-2, j, k)}{2 \Delta x} \quad (B-2)$$

Similarly for j when $j = 1$ or $j = JT$.

The following four combinations were tried. Their results are outlined.

(1) Central differences for all spatial gradients (except, of course, on the boundaries). A two point difference scheme (equation below) was used to calculate all the gradients at all the grid points except at the boundaries where a three point forward or backward difference scheme (Eqs. (B-1) and (B-2)) was used. e.g.

$$\frac{\partial \bar{F}}{\partial x} (2,j,k) = \frac{\bar{F}(3,j,k) - \bar{F}(1,j,k)}{2 \Delta x} \quad (B-3)$$

$$\frac{\partial \bar{G}}{\partial y} (i,2,k) = \frac{\bar{G}(i,3,k) - \bar{G}(i,1,k)}{2 \Delta y}$$

(2) Forward difference on the \bar{F} and \bar{G} (Eq. (B-4)) vectors to obtain properties at intermediate time step, Eq. (58),

$$\frac{\partial \bar{F}}{\partial x} (2,j,k) = \frac{\bar{F}(3,j,k) - \bar{F}(2,j,k)}{\Delta x} \quad (B-4)$$

$$\frac{\partial \bar{G}}{\partial y} (i,2,k) = \frac{\bar{G}(i,3,k) - \bar{G}(i,2,k)}{\Delta y}$$

and backward differences (Eq. (B-5)) for Eq. (59),

$$\frac{\partial \bar{F}}{\partial x} (2,j,k) = \frac{\bar{F}(2,j,k) - \bar{F}(1,j,k)}{\Delta x} \quad (B-5)$$

$$\frac{\partial \bar{G}}{\partial y} (i,2,k) = \frac{\bar{G}(i,2,k) - \bar{G}(i,1,k)}{\Delta y}$$

but consistently using central differences for T , u , v and ρ_k .

This was called "Partial MacCormack".

(3) Same as (2) above, with the exception of using forward differences for T , u , v and ρ_k (eq. (B-6)),

$$\frac{\partial T}{\partial x}(2,j,k) = \frac{T(3,j,k) - T(2,j,k)}{\Delta x} \quad (B-6)$$

while solving Eq. (58) and backward (Eq. (B-7)),

$$\frac{\partial T}{\partial y}(i,2,k) = \frac{T(i,2,k) - T(i,1,k)}{\Delta y} \quad (B-7)$$

while solving Eq. (59). This was termed "full MacCormack".

(4) Same as (3) above but with a reverse combination viz. backward difference for T , u , v , ρ_k for solving Eq. (58) and forward difference for solving Eq. (59). This could be called "Modified MacCormack". This combination yielded the best results of the above four variations.

Emphasis is made that in methods (2) - (4) above, a forward difference is always used on \bar{F} and \bar{G} for the predictor step, and a rearward difference for the corrector step. The variations between methods (2) - (4) occur only in the differencing of the primary flow variables T , u , v and ρ_k .

Figure B-1 depicts the numerical effect of the various schemes. Pressure at $x/h = 10$ and $y/h = 0.5$ is plotted versus non-dimensional time. Here the velocity profile at the upstream boundary was assumed to be continuous. Results from the four schemes above are labeled 1 - 4 respectively in Figure B-1. Surprisingly, note that scheme 3, the "full MacCormack", did not converge to a steady-state; the program blew up for this case. We have no explanation for this. Scheme 1, using all central differences, converged to a solution of sorts, but with some noticeable oscillations. Scheme 4, the "modified MacCormack" had the

best convergence behavior. In addition, Figs. B-2 through B-4 compare the converged steady-state results from schemes 1, 2 and 4. In Fig. B-2, the velocity profile (variation of u with y) at $x/h = 10$ is shown as calculated from the three convergent schemes. Note that the central differencing and partial MacCormack schemes yielded almost identical profiles, but with wiggles; in contrast, the modified MacCormack scheme yielded a smooth profile which ran through the middle of the above wiggles. Exactly the same comparison is observed in Fig. B-3, which illustrates the F_2 and F density profiles at $x/h = 10$. Again, the modified MacCormack scheme yields smooth profiles which goes through the middle of the wiggles observed from the other techniques. Figure B-4 shows the most striking comparison. Here, the pressure distribution at $x/h = 10$ is given as a function of y . Note that the central difference scheme yields a series of regular wiggles, whereas both the partial and modified MacCormack schemes yield smooth results. Also note that the abscissa in Fig. B-4 is an expanded scale to emphasize the comparison.

The results shown in Figs. B-1 through B-4 clearly indicate that the modified MacCormack (scheme 4 above) yields the best qualitative results, (and presumably quantitative as well). The use of forward finite-differences for F and G in conjunction with rearward differences for T , u , v and ρ_k , and vice versa, appears to be best for the mixing flows studied in the present investigation.

As a final note on this series of results, the preservation of mass flow from the upstream to the downstream boundary is given in the Table IV. Obviously, in real life, mass is preserved; however, computational fluid dynamic calculations such as given here sometimes result in an artificial loss or gain of mass in the flow direction. Calculations

were made for $m = \int_0^h \rho u \, dy$ at $x/h = 0$ and $x/h = 10$ for schemes 1, 2 and 4. The results are given in Table IV. For all practical purposes the loss in the mass flux is negligibly small, thus again accentuating the correctness of the results.

REFERENCES

1. Anderson, J. D., Jr., *Gasdynamic Lasers: An Introduction*, Academic Press, New York, 1976.
2. Glowacki, W. J. and Anderson, J. D., Jr., "A Computer Program for $\text{CO}_2\text{-N}_2\text{-H}_2\text{O}$ Gasdynamic Laser Gain and Maximum Available Power," NOLTR 71-210, Oct. 1971, Naval Ordnance Lab., White Oak, Md.
3. Russel, D. A., "Fluid Mechanics of High Power Grid Nozzle Lasers," AIAA Paper No. 74-223 (1974).
4. Reilly, J. P., "High Power Electric Discharge Lasers (EDL's)," *Astronautics and Aeronautics*, Vol. 13, March 1975, pp. 52-63.
5. Warren, W. R., Jr., "Chemical Lasers," *Astronautics and Aeronautics*, Vol. 13, April 1975, pp. 36-49.
6. Gross, R. W. F. and Bott, J. F., *Handbook of Chemical Lasers*, Wiley Interscience, 1976.
7. Roache, P. J., *Computational Fluid Dynamics*, Hermosa Publishers, Albuquerque, N. Mex., 1972.
8. Chapman, D. R., Mark, H., and Pirtle, M. W., "Computers vs. Wind Tunnels," *Astronautics and Aeronautics*, Vol. 13, April 1975, pp. 22-30.
9. Taylor, R. D., "Numerical Methods for Predicting Subsonic Transonic and Supersonic Flow," AGARDograph No. 187, January, 1974.
10. Emanuel, G., Adams, W. D., and Turner, E. B., "Resale 1: A Chemical Laser Computer Program," Aerospace Corp. TR-0172 (2276)-1, El Segundo, CA., March 1972.
11. Hofland, R. and Mirels, H., "Flame-Sheet Analysis of CW Diffusion-Type Chemical Lasers, I. Uncoupled Radiation," *AIAA Journal*, Vol.

- 10, April 1972, pp. 420-428.
12. Hofland, R. and Mirels, H., "Flame Sheet Analysis of CW Diffusion-Type Chemical Lasers, II. Coupled Radiation," AIAA Journal, Vol. 10, Oct. 1972, pp. 1271-1280.
 13. King, W. S. and Mirels, H., "Numerical Study of a Diffusion-Type Chemical Laser," AIAA Journal, Vol. 10, Dec. 1972, pp. 1647-1654.
 14. Tripodi, R., Coulter, L. J., Bronfin, B. R. and Cohen, L. S., "Coupled Two-Dimensional Computer Analysis of CW Chemical Mixing Lasers," AIAA Journal, Vol. 13, June 1975, pp. 776-784.
 15. Grohs, G. L., "Chemical Laser Cavity Mixing and Turbulence," AIAA Paper 76-56, Syracuse, N.Y., 1976.
 16. Kothari, A. P. and Anderson, J. D., Jr., "Navier-Stokes Solutions for Chemical Laser Flows," Technical Report AE 75-6, Dept. of Aerospace Eng., University of Maryland, June 1975, also AFOSR-TR-75-1447.
 17. Kothari, A. P. and Anderson, J. D., Jr., "Navier-Stokes Solutions for Chemical Laser Flows: Cold Flows," AIAA Journal, Vol. 14, May 1976, pp. 702-703.
 18. Kothari, A. P., Anderson, J. D., Jr., and Jones, E., "Navier-Stokes Solutions for Chemical Laser Flows," AIAA Journal, Vol. 15, No. 1, Jan. 1977, pp. 92-100.
 19. Kothari, A. P., Anderson, J. D., Jr., and Jones, E., "Navier-Stokes Solutions for Chemical Laser Flows: Steady and Unsteady Flows," AIAA paper No. 79-0009, (1979).
 20. Theones, J., McDanal, A. J., Ratliff, A. W. and Smith, S. D., "Analysis of Chemical Lasers; Vol. 1, Laser and Mixing Program (LAMP), Theory and User's Guide," Lockheed. Technical Report

- RK-CR-74-13, Huntsville, Alabama.
21. Zelazny, S. W., Driscoll, R. J., Raymouda, J. W., Blauer, J. A. and Soloman, W. C., "Modelling DF/HF CW Lasers: An Examination of Key Assumptions," AIAA Journal, Vol. 16, No. 4, April 1978, pp. 297-304.
 22. Jones, E. and Anderson, J. D., Jr., "Numerical Solutions of the Navier-Stokes Equations for Laminar and Turbulent Supersonic Mixing Flows," Aerospace Engineering Technical Report AE-75-5, University of Maryland, College Park, MD., June 1975.
 23. Parthasarathy, K. N., Anderson, J. D., Jr. and Jones, E., "Downstream Mixing Gasdynamic Lasers - A Numerical Solution," AIAA Paper 79-0207 (1979).
 24. MacCormack, R. W., "The Effect of Viscosity in Hypervelocity Impact Cratering," AIAA Paper, 69-354, Cincinnati, Ohio, 1969.
 25. Butler, R. D. and O'Rourke, P. J., "A Numerical Method for Two-Dimensional Unsteady Reacting Flows," 16th International Symposium on Combustion, Aug. 15-21, 1976, Cambridge, Mass.
 26. Ramshaw, J. D., Mjolsness, R. C. and Farmaer, O. A., "Numerical Method for Two-Dimensional Steady-State Chemical Laser Calculations," Journal of Quantitative Spectroscopy and Radiative Transfer, March 1976.
 27. Rivard, W. C., Farmer, O. A., and Butler, T. D., "RICE: A Computer Program for Multicomponent Chemically Reactive Flows at All Speeds," Report LA-5812, Los Alamos Scientific Lab., N. Mex., Nov. 1974.
 28. Theones, J. and Ratcliff, A. W., "Chemical Laser Oscillator Analytical Model," AIAA Paper 73-644, Palm Springs, Calif., 1973.

29. King, W. S., and Mirels, H., "Numerical Study of a Diffusion Type Chemical Laser," Aerospace Corporation SAMS ²TR-75-140, El Segundo, Calif., June 1975.
30. Lengyle, B. A., Lasers, Wiley-Interscience, New York, 1971.
31. Anderson, J.D., Jr., "A Time-Dependent Analysis for Vibrational and Chemical Nonequilibrium Nozzle Flows," AIAA Journal, Vol. 8, March 1970, pp. 545-550.
32. Reid, R. C. and Sherwood, T. K., The Properties of Gases and Liquids, McGraw-Hill, 1966.
33. Schlichting, H., Boundary Layer Theory, McGraw-Hill, New York, 1968.
34. Brokaw, R. S., "Alignment Charts for Transport Properties Viscosity, Thermal Conductivity and Diffusion Coefficients for Non-Polar Gases and Gas Mixtures at Low Density," NASA TR-R-81, 1961.
35. Cohen, N., "A Review of Rate Coefficients for Reactions in the H₂-F₂ Laser System," Aerospace Corporation Report TR-5073 (3420)-9, El Segundo, Calif., No. 1972.
36. Stull, D. R., and Prophet, H., JANAF Thermochemical Tables, 2nd Edition, NSRDC-NBS 36, U.S. Dept. of Commerce, Washington, D.C., June 1971.
37. Cohen, N., Private Communication, Oct. 15, 1974, Aerospace Corporation, El Segundo, Calif.
38. Anderson, J. D., Jr., "Gasdynamic Lasers: Theory, Experiment and the State of the Art," Technical Report AE 74-1, Dept. of Aerospace Eng., University of Maryland, College Park, Md., May 1974.
39. Mitchell, A. C. G., and Zemansky, M. W., "Resonance Radiation and Excited Atom," Cambridge University Press, England, 1934 (1961).

40. Anderson, J. D., Jr., Albacete, L. M., and Winkelmann, A. E., "On Hypersonic Blunt Body Flow Fields Obtained with a Time-Dependent Technique," NOLTR-68-129, Aug. 1968, Naval Ordnance Lab., White Oak, Md.
41. Moretti, G. and Abbett, M., "A Time-Dependent Computational Method for Blunt Body Flows," AIAA Journal, Vol. 4, Dec. 1956, pp. 2136-2141.
42. Courant, R., Fredrichs, K. O. and Lewy, H., "Ueber die Diferenzgleichungen der Machematischen der Matehmatischen Physic," Mathematics Annuals Vol. 100, 1928, p. 32.
43. Vincenti, W. G. and Kruger, C. H., Introduction to Physical Gas Dynamics, Wiley, New York, 1965.
44. Zelazny, S. B., Private communication, May 1979, Bell Aerospace Textron, Buffalo, New York.
45. Roshko, A., "Structure of Turbulent Shear Flows: A New Look," Dryden Lecture of AIAA; AIAA Paper 76-78, 1976. Also AIAA Journal, Vol. 14, No. 10, October 1976, pp. 1349-1357.
46. Meredith, R. E. and Smith, F. G., "Investigation of Fundamental Laser Processes Vol. II: Computation of Electric Dipole Matrix Elements for Hydrogen Fluoride and Deuterium Fluoride," Report 84130-39-T(II), Willow-Run Laboratory, Ann Arbor, Michigan, 1971.
47. Kwok, M. A., Giedt, R. R. and Gross, R. W. F., "Comparison of HF and DF Continuous Chemical Lasers: II, Spectroscopy," Applied Physics Letters, May 1970, Vol. 16, No. 10, pp. 386-387.

TABLE I⁴⁷

Wavelength of Radiation for Various P Transitions

Identification Vibrational Band	Line	Wavelength μ
1 \rightarrow 0	P(4)	2.640
	P(5)	2.673
	P(6)	2.707
	P(7)	2.744
2 \rightarrow 1	P(4)	2.760
	P(5)	2.795
	P(6)	2.832
	P(7)	2.871

TABLE II-

Species #	Species Name	C_p cal gmole ^o k	σ Å	ϵ/k °k	Sp. Gas Const. R j kg°k	Molr. Wt m kg/kgmole	e_{vib} j/kg	ΔH_f^o j/kg
1	F ₂	7.49	3.653	112	218.8	38	0	0
2	H ₂	6.892	2.915	38	4124.3	2.016	0	0
3	F	5.437	2.9	112	437.6	19	0	3.8391x10 ⁶
4	H	4.968	2.68	38	8248.6	1.008	0	1.07986x10 ⁷
5	He	4.966	2.576	10.22	2077.1	4.0026	0	0
6	HF(0)	6.964	4.1	354	415.56	20.008	0	-1.35512x10 ⁷
7	HF(1)	6.964	4.1	354	415.56	20.008	2.3691x10 ⁶	-1.35512x10 ⁷
8	HF(2)	6.964	4.1	354	415.56	20.008	4.6352x10 ⁶	-1.35512x10 ⁷
9	HF(3)	6.964	4.1	354	415.56	20.008	6.8012x10 ⁶	-1.35512x10 ⁷
10	HF(4)	6.964	4.1	354	415.56	20.008	8.8696x10 ⁶	-1.35512x10 ⁷
11	HF(5)	6.964	4.1	354	415.56	20.008	1.08427x10 ⁷	-1.35512x10 ⁷
12	HF(6)	6.964	4.1	354	415.56	20.008	1.2722x10 ⁷	-1.35512x10 ⁷
13	HF(7)	6.964	4.1	354	415.56	20.008	1.4509x10 ⁷	-1.35512x10 ⁷
14	HF(8)	6.964	4.1	354	415.56	20.008	1.6205x10 ⁷	-1.35512x10 ⁷

Molecular properties of various species

Table III. Recommended Rate Coefficients for H₂ - F₂ Chemical Laser

Reaction No.	Reaction	Rate Coefficient (cc/mole-sec)	M, v
1a	F ₂ + M ₁ = 2F + M ₁	k _{1a} = 10 ^{13.7-35.1/θ}	M ₁ = all species except F, F ₂
1b	F ₂ + M ₂ = 2F + M ₂	k _{1b} = 2.4k _{1a}	M ₂ = F, F ₂
2a	H ₂ (0) + M ₃ = 2H + M ₃	k _{-2a} = 10 ^{18T⁻¹}	M ₃ = all except H, H ₂
2b	H ₂ (0) + M ₄ = 2H + M ₄	k _{-2b} = 10 ^{17T⁻¹-0.6}	M ₄ = H ₂
2c	H ₂ (0) + M ₅ = 2H + M ₅	k _{-2c} = 20k _{-2a}	M ₅ = H
3v	HF(v) + M ₆ = H + F + M ₆	k _{3v} = $\frac{1.2}{n} \times 10^{19-135.9/\theta - 1.0(E_v - E_0)/\theta}$	M ₆ = all species v = 0 . . . n - 1
4a	F + H ₂ (v) = HF(1) + H	k _{4a} = 2.6 × 10 ^{13-1.6/θ}	all v
4b	F + H ₂ (v) = HF(2) + H	k _{4b} = 8.8 × 10 ^{13-1.6/θ}	all v
4c	F + H ₂ (v) = HF(3) + H	k _{4c} = 4.4 × 10 ^{13-1.6/θ}	all v
4d	F + H ₂ (v) = HF(4) + H	$\sum_v k_{-4dv} = 7.4 \times 10^{12-0.50/\theta}$	see note a
4e	F + H ₂ (v) = HF(5) + H	$\sum_v k_{-4ev} = 1.1 \times 10^{13-0.51/\theta}$	see note a
4f	F + H ₂ (v) = HF(6) + H	$\sum_v k_{-4fv} = 1.9 \times 10^{13-0.56/\theta}$	see note a
5a	H + F ₂ = HF(0) + F	k _{5a} = 1.1 × 10 ^{12-2.4/θ}	
5b	H + F ₂ = HF(1) + F	k _{5b} = 2.5 × 10 ^{12-2.4/θ}	
5c	H + F ₂ = HF(2) + F	k _{5c} = 3.5 × 10 ^{12-2.4/θ}	
5d	H + F ₂ = HF(3) + F	k _{5d} = 3.6 × 10 ^{12-2.4/θ}	
5e	H + F ₂ = HF(4) + F	k _{5e} = 1.6 × 10 ^{13-2.4/θ}	
5f	H + F ₂ = HF(5) + F	k _{5f} = 3.6 × 10 ^{13-2.4/θ}	
5g	H + F ₂ = HF(6) + F	k _{5g} = 4.8 × 10 ^{13-2.4/θ}	
5h	H + F ₂ = HF(7) + F	k _{5h} = 5.5 × 10 ^{12-2.4/θ}	
5i	H + F ₂ = HF(8) + F	k _{5i} = 2.5 × 10 ^{12-2.4/θ}	
6a _v	HF(v) + M ₇ = HF(v-1) + M ₇	k _{6a_v} = v(10 ^{14.0T⁻¹-0.8} + 10 ^{0.4T⁻¹-3.5}) ^b	M ₇ = HF, v = 1 . . . 8

Table III. Recommended Rate Coefficients for H₂ - F₂ Chemical Laser
(Continued)

Reaction No.	Reaction	Rate Coefficient (cc/mole-sec)	M, v
6b ₁	HF(1) + M ₈ = HF(0) + M ₈	$k_{6b_1} = 1.5 \times 10^{10-1.1/\theta_T}$	M ₈ = F
6b ₂	HF(2) + M ₈ = HF(1) + M ₈	$k_{6b_2} = 1.5 \times 10^{10-0.5/\theta_T}$	v = 3 . . . 8
6b _v	HF(v) + M ₈ = HF(v-1) + M ₈	$k_{6b_v} = 1.5 \times 10^{10}$	M ₉ = Ar, F ₂ , v = 1 . . . 8
6c _v	HF(v) + M ₉ = HF(v-1) + M ₉	$k_{6c_v} = (8 \times 10^{-4} T^4)_v$	M ₁₀ = He v = 1 . . . 8
6d _v	HF(v) + M ₁₀ = HF(v-1) + M ₁₀	$k_{6d_v} = v(8.7 \times 10^{-7} T^5)$	M ₁₁ = N ₂ v = 1 . . . 8
6e _v	HF(v) + M ₁₁ = HF(v-1) + M ₁₁	$K_{6e_v} = v(3 \times 10^{-4} T^2)$	M ₁₂ = H v = 1 . . . 8, v' < v see note c
6f _v	HF(v) + M ₁₂ = HF(v') + M ₁₂	$k_{6f_v} = 1.8 \times 10^{13-0.7/\theta}$	M ₁₃ = H ₂ v = 1 . . . 8
6g _v	HF(v) + M ₁₃ = HF(v-1) + M ₁₃	$k_{6g_v} = v(1 \times 10^5 T^2)$	v = 1 . . . 7
7a	HF(v) + HF(v) = HF(v-1) + HF(v+1)	$k_{7a} = 1.5 \times 10^{12} T^{1/2}$	v = 1 . . . 6
7b	HF(v) + HF(v+1) = HF(v-1) + HF(v+2)	$k_{7b} = 0.5k_{7a}$	v = 1 . . . 5
7c	HF(v) + HF(v+2) = HF(v-1) + HF(v+3)	$k_{7c} = 0.25k_{7a}$	v = 1 . . . 4
7d	HF(v) + HF(v+3) = HF(v-1) + HF(v+4)	$k_{7d} = 0.125k_{7a}$	
8a	HF(0) + H ₂ (1) = HF(1) + H ₂ (0)	$k_{8a} = 9 \times 10^{11}$	
8b	HF(1) + H ₂ (1) = HF(2) + H ₂ (0)	$k_{8b} = 2.9 \times 10^{12}$	
8c	HF(2) + H ₂ (1) = HF(3) + H ₂ (0)	$k_{8c} = 9 \times 10^{12}$	
8d	HF(3) + H ₂ (1) = HF(4) + H ₂ (0)	$k_{8d} = 2 \times 10^{13}$	
8e	HF(0) + H ₂ (2) = HF(1) + H ₂ (1)	$k_{8e} = k_{8a}$	
8f	HF(1) + H ₂ (2) = HF(2) + H ₂ (1)	$k_{8f} = k_{8b}$	v = 1, 2
9a _v	H ₂ (v) + M ₃ = H ₂ (v-1) + M ₃	$k_{9a_v} = v(2.5 \times 10^{-4}) T^{4.3}$	v = 1, 2
9b _v	H ₂ (v) + M ₁₄ = H ₂ (v-1) + M ₁₄	$k_{9b_v} = v(10^{-3} T^{4.3})$	

^a See text for specific values of k_{7d} for various vibrational levels of H₂.

^b If calculations are confined either to T > 1200°K or T < 1200°K, see text for appropriate forms of k_{6a_v} .

^c See text for more precise values of k_{6f} for different v and v'.

$\theta = 4.575T/1000$ kcal/mole

v = Vibrational level

M = Collision partner

TABLE IV
Mass conservation in flow-wise direction

Scheme	\dot{m} @ $x/h = 0$	\dot{m} @ $x/h = 10$	% Loss
Central Differences	5.2786	5.2754	0.06062%
Partial MacCormack	5.2786	5.2688	0.18566%
Modified MacCormack	5.2786	5.2726	0.11367%

\dot{m} HAS BEEN NON-DIMENSIONALIZED BY $\rho_r U_r$

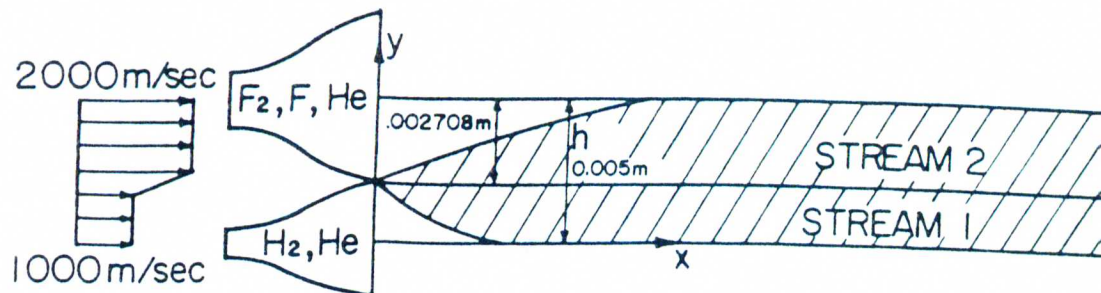


fig. 1

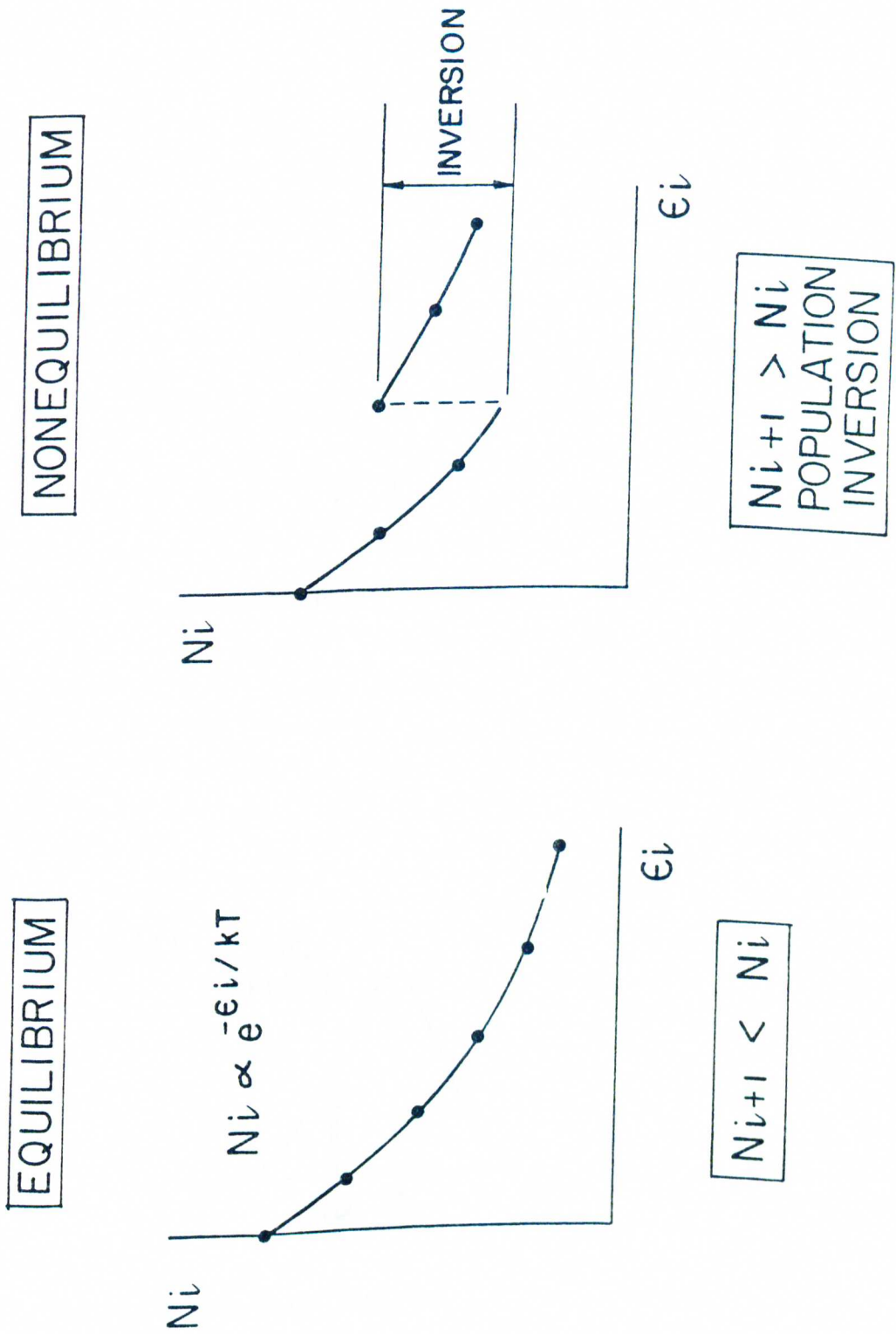
NOZZLE CONFIGURATION

	STREAM 1	STREAM 2
$P \text{ n/m}^2$	500	500
$T \text{ }^\circ\text{K}$	150	150
$\rho \text{ Kg/m}^3$	8.1619×10^{-4}	3.7214×10^{-3}
$\rho_1 \text{ Kg/m}^3$	—	1.8282×10^{-3}
$\rho_2 \text{ Kg/m}^3$	8.00136×10^{-4}	—
$\rho_3 \text{ Kg/m}^3$	—	0.6094×10^{-3}
$\rho_4 \text{ Kg/m}^3$	—	—
$\rho_5 \text{ Kg/m}^3$	1.6048×10^{-5}	1.2838×10^{-3}

INITIAL CONDITIONS

$\rho_k = 0$ for $k=6,7,\dots,14$

Fig. 2 --- Population inversion-mechanism for laser action



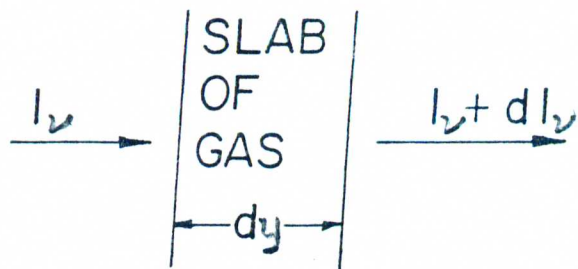


Fig. 3 -- Slab of gas emitting or absorbing radiation

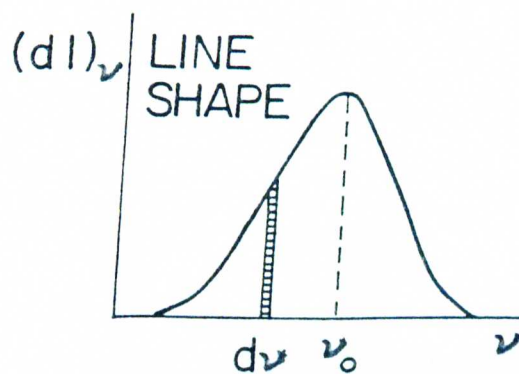


Fig. 4 -- Plot of a line shape function

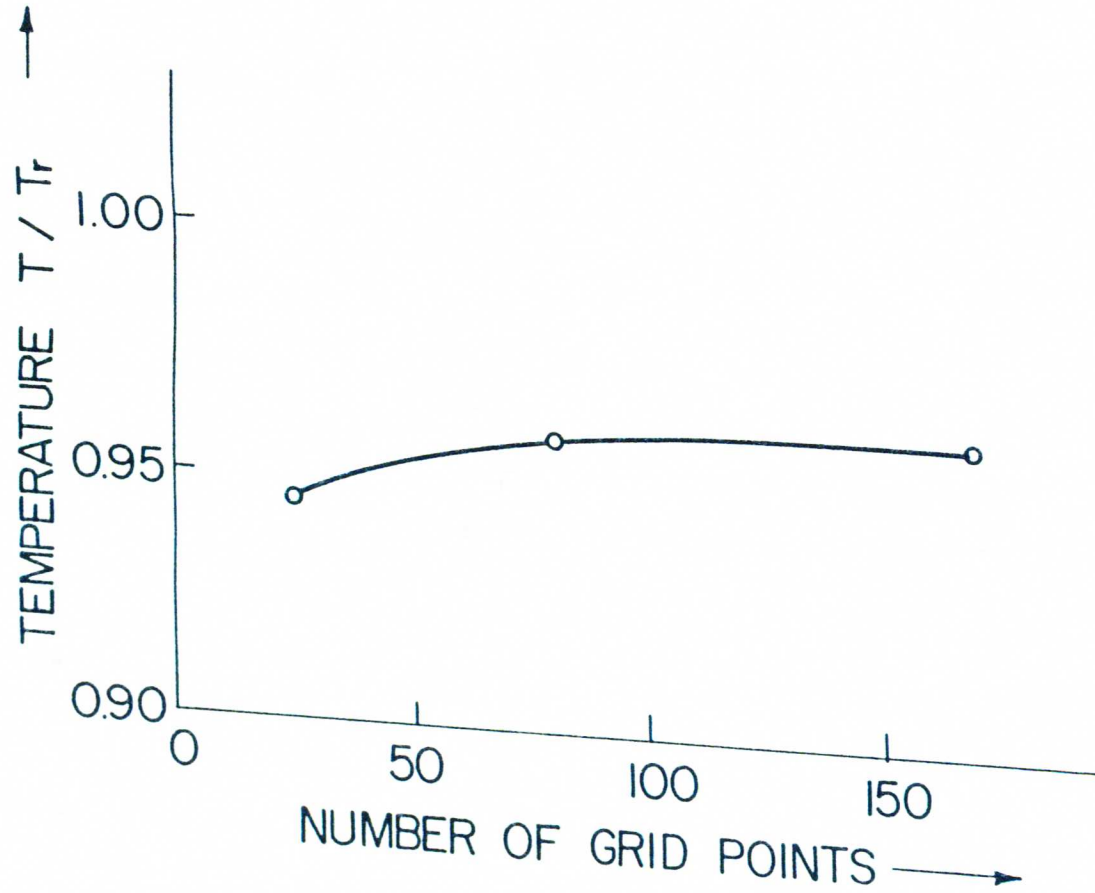


Fig. 5 -- Convergence behavior of the solution for various grids

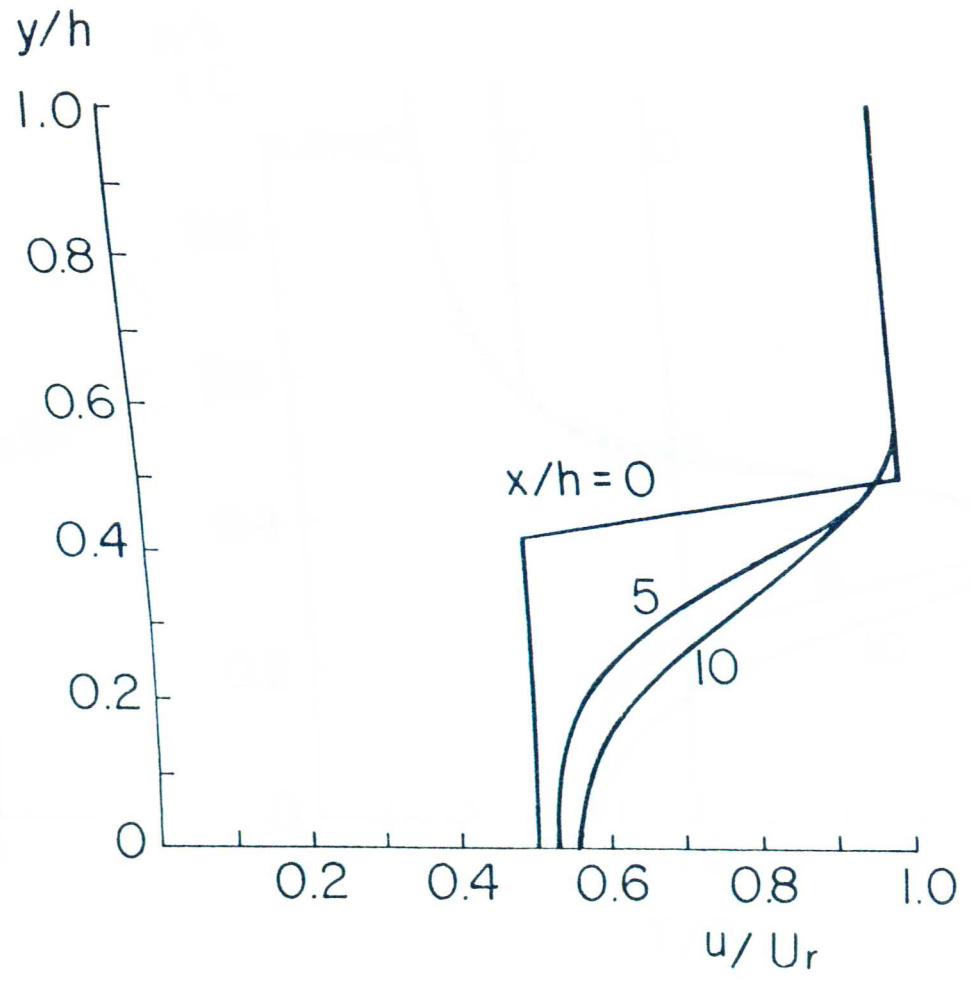
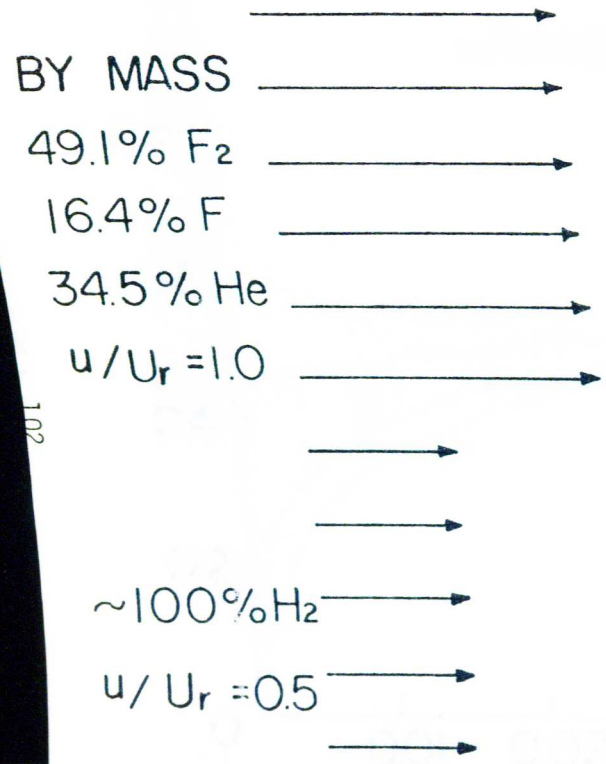


fig. 6

VELOCITY PROFILES AT VARIOUS X LOCATIONS
 FOR 13 x 13 GRID SIZE

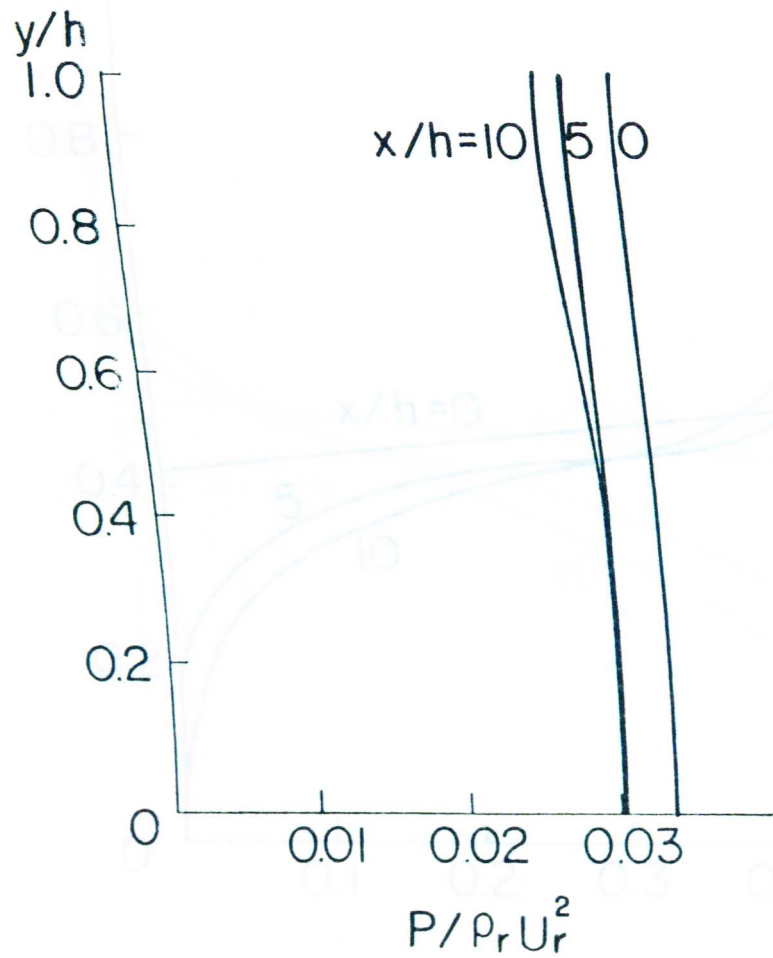


fig. 7
 PRESSURE PROFILES
 at $x/h = 0,5$ and 10
 13 x 13 GRID

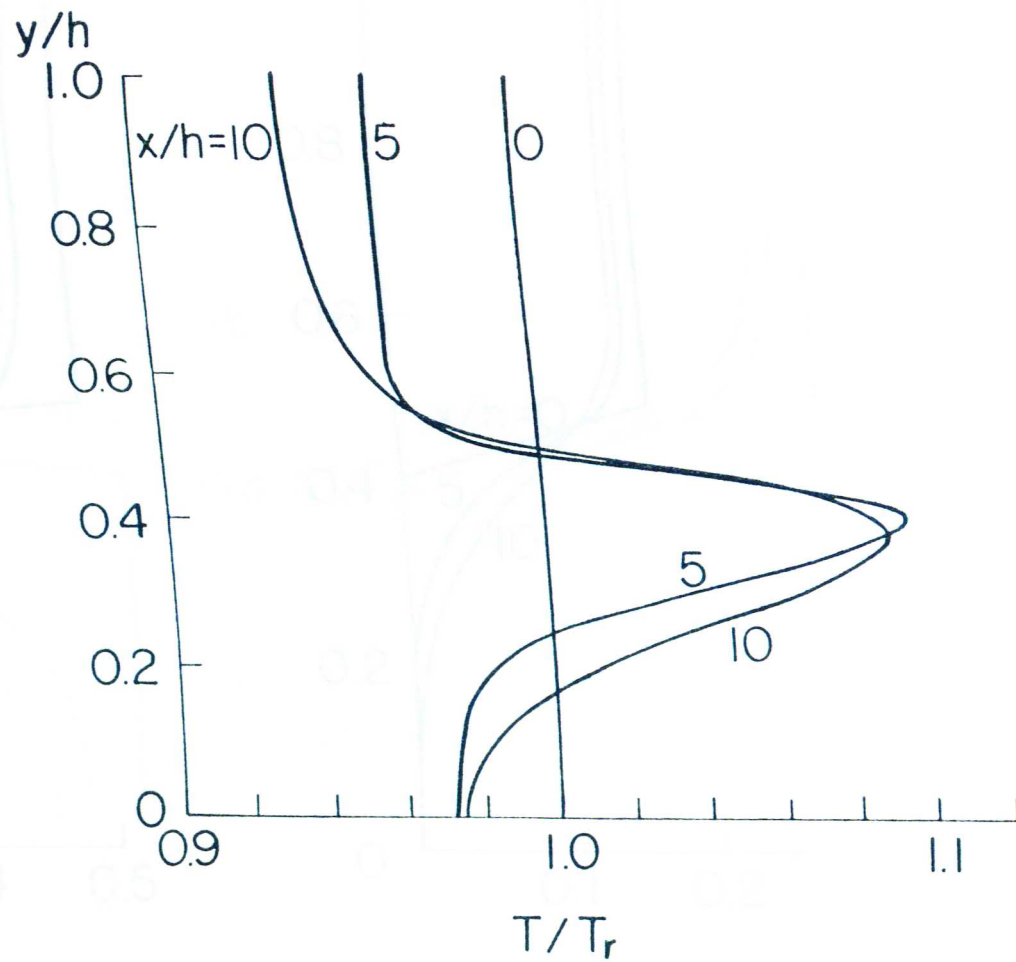


fig. 8
 TEMPERATURE PROFILES
 at $x/h = 0,5$ and 10
 13 x 13 GRID

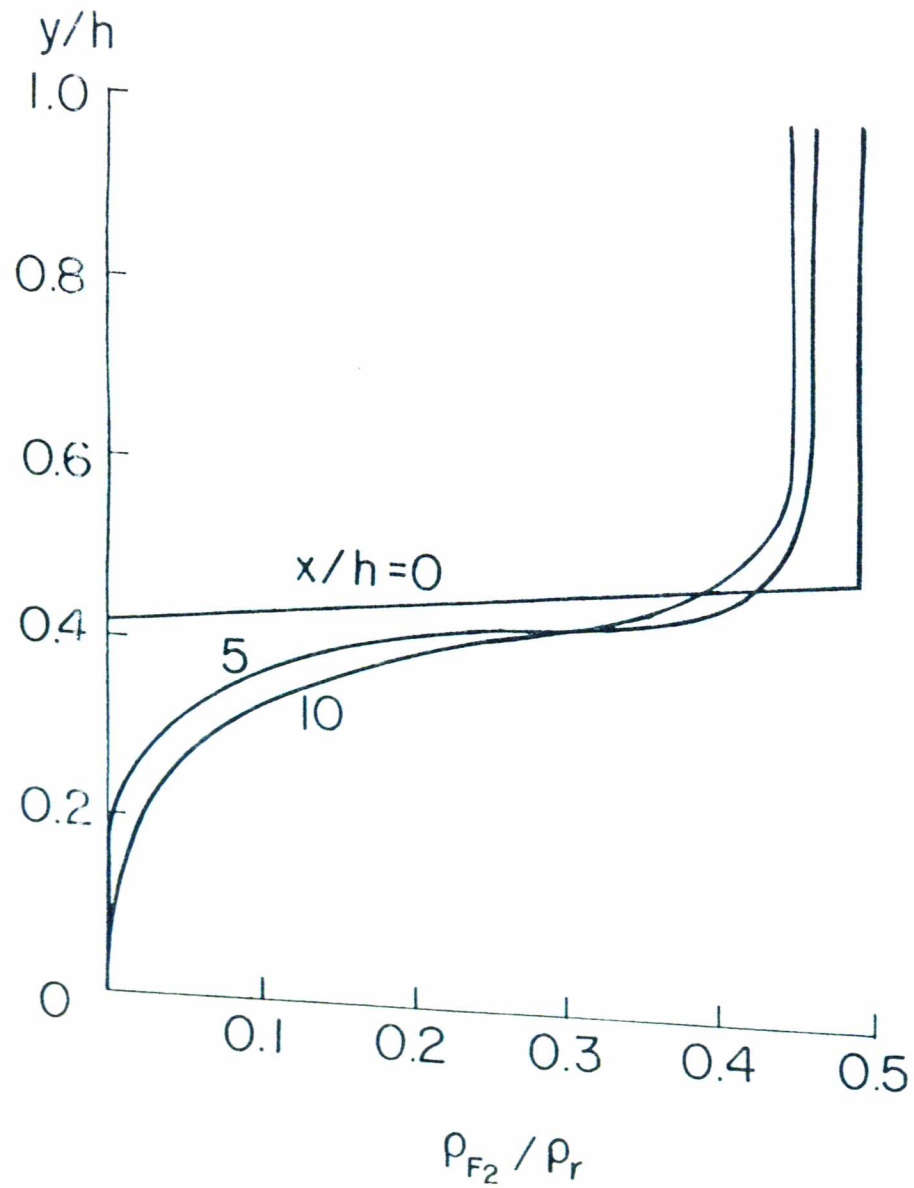


fig. 9

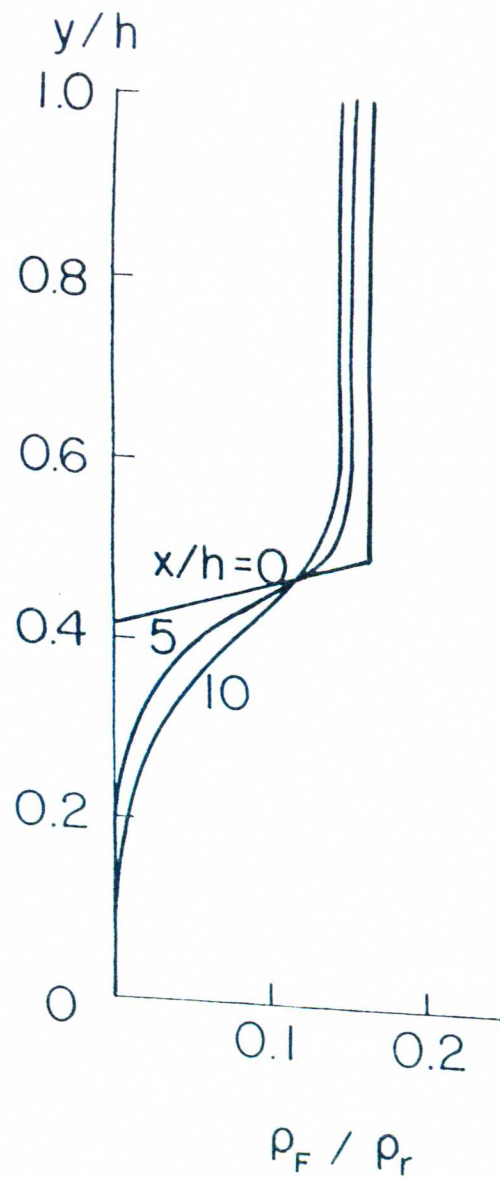


fig. 10

SPECIFIC DENSITY PROFILES AT VARIOUS X LOCATIONS
FOR 13 x 13 GRID SIZE

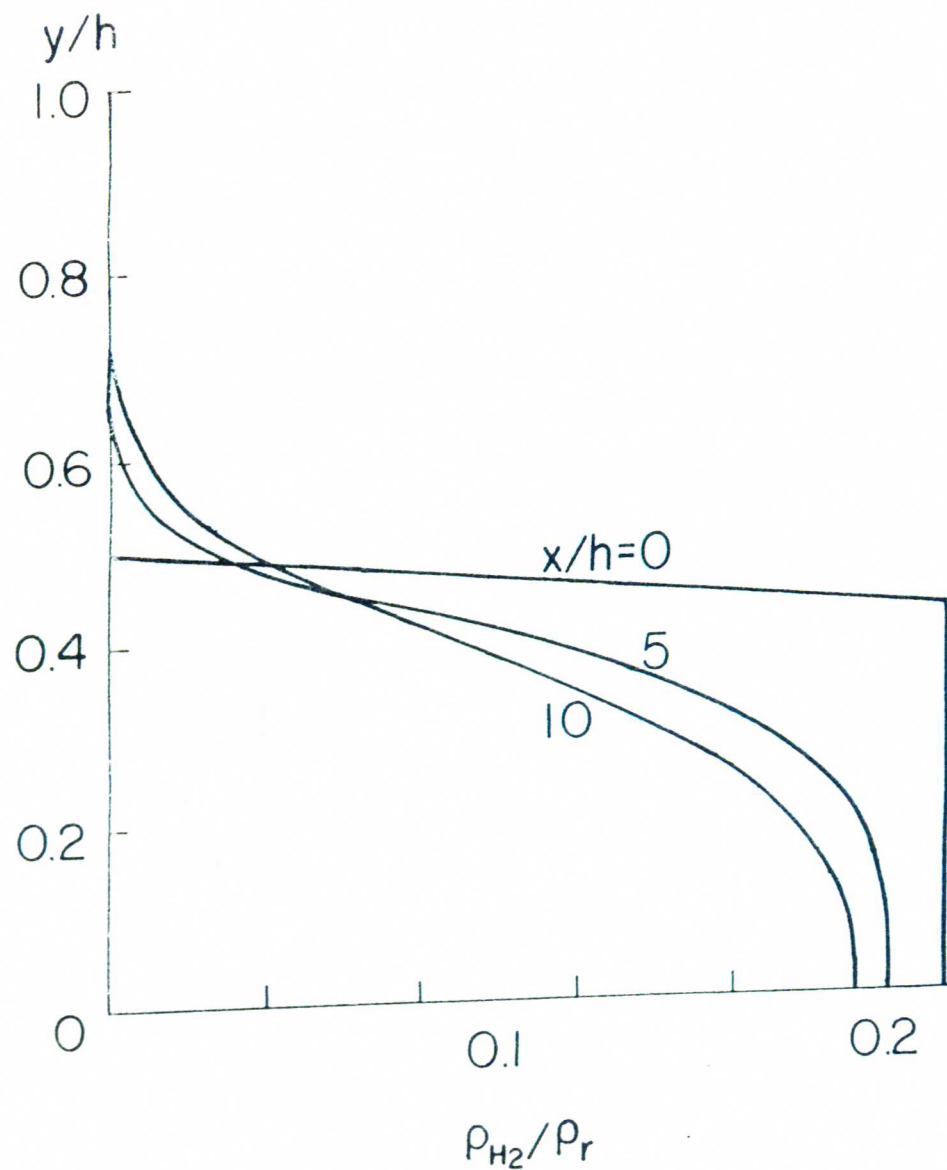


fig. 11

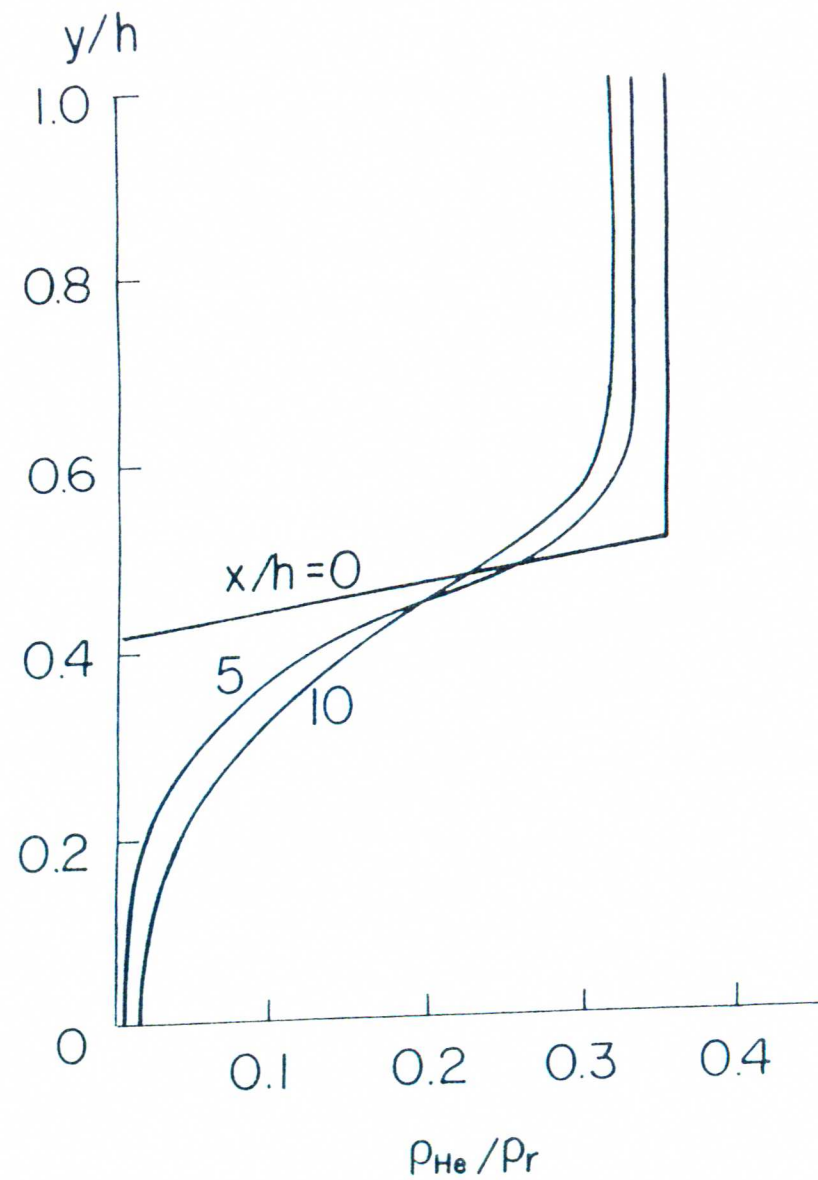


fig. 12

SPECIFIC DENSITY PROFILES AT VARIOUS X LOCATIONS
FOR 13 x 13 GRID SIZE

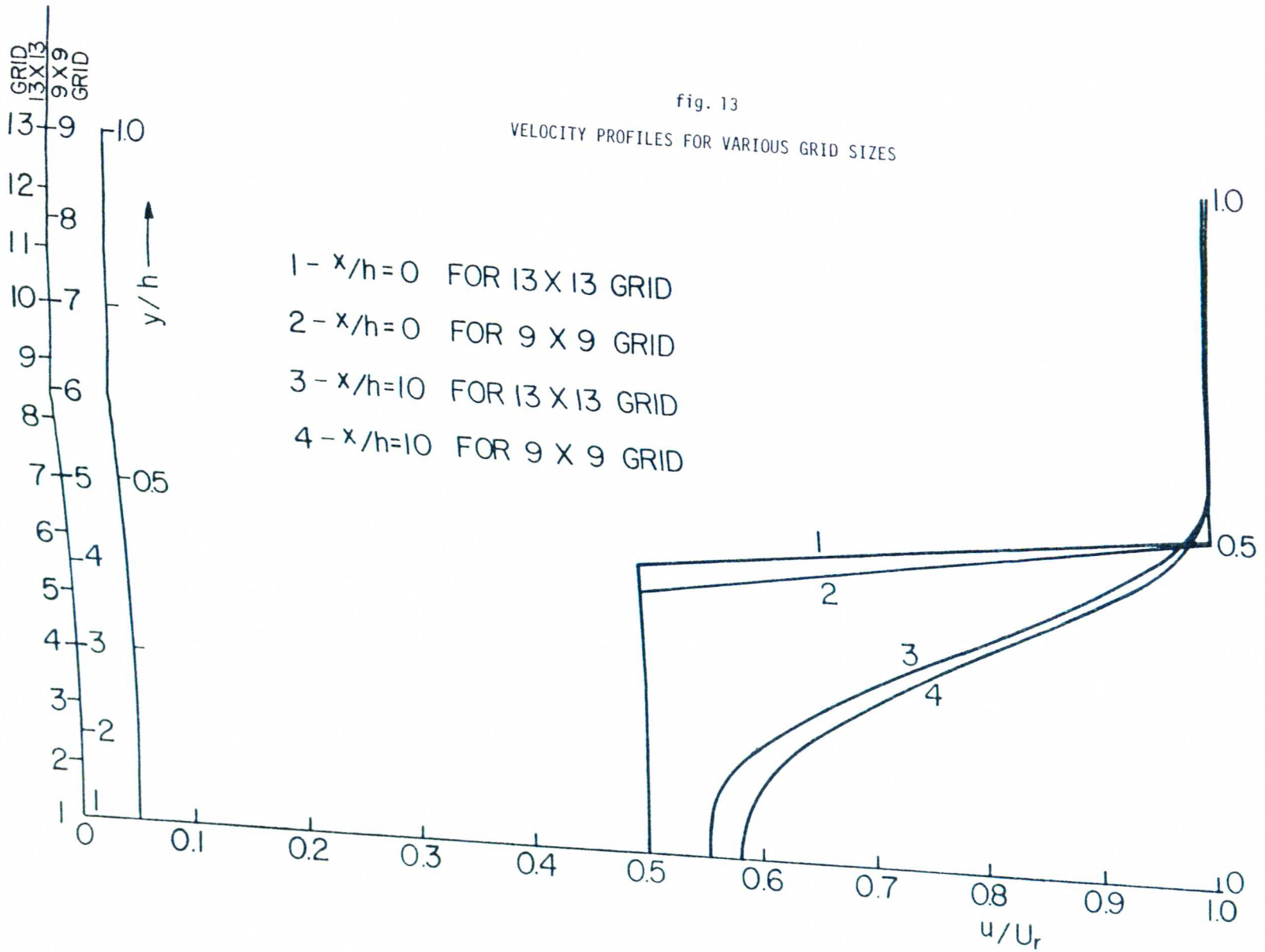


fig. 14

PRESSURE PROFILES FOR VARIOUS GRID SIZES

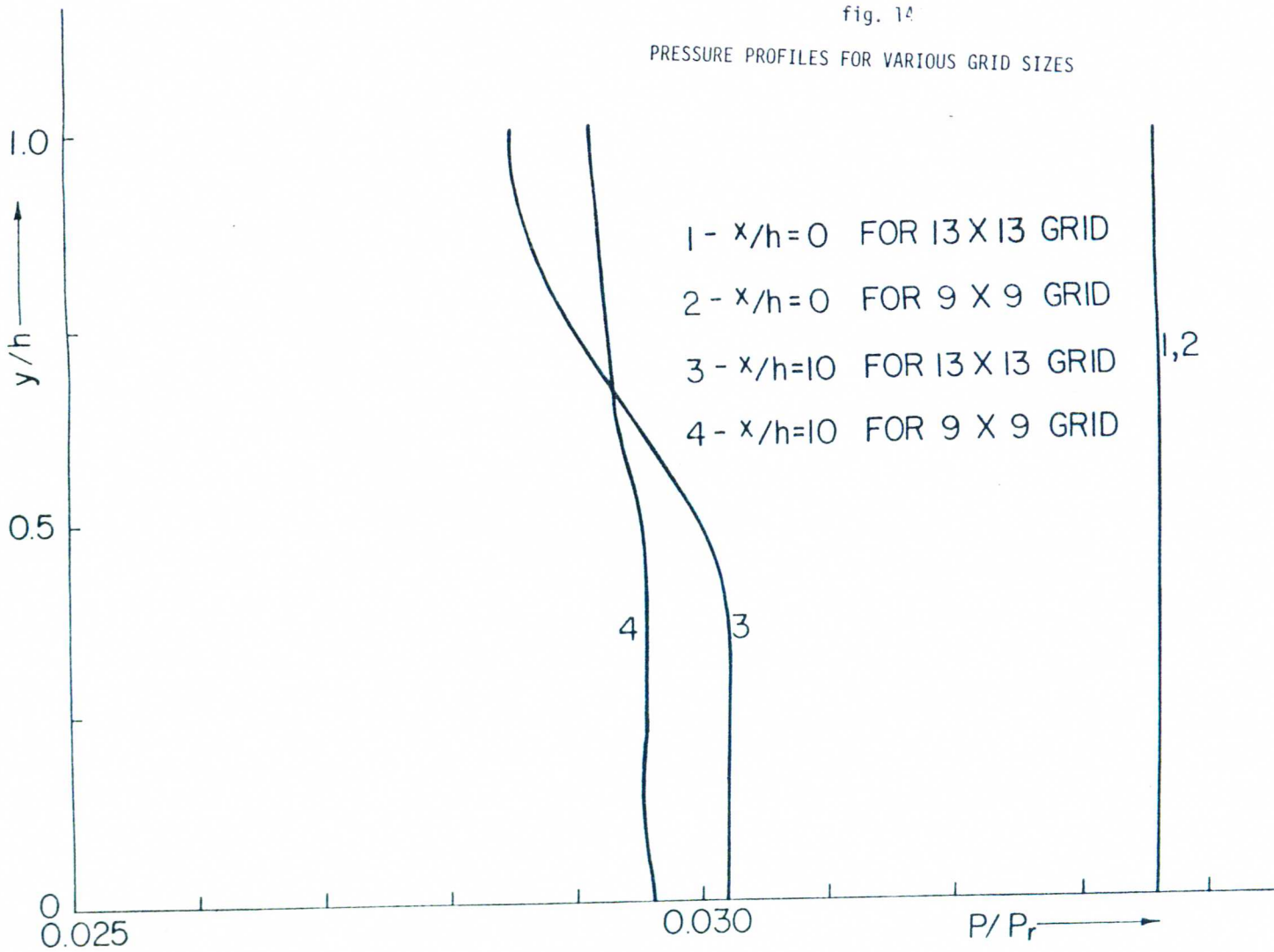


fig. 15

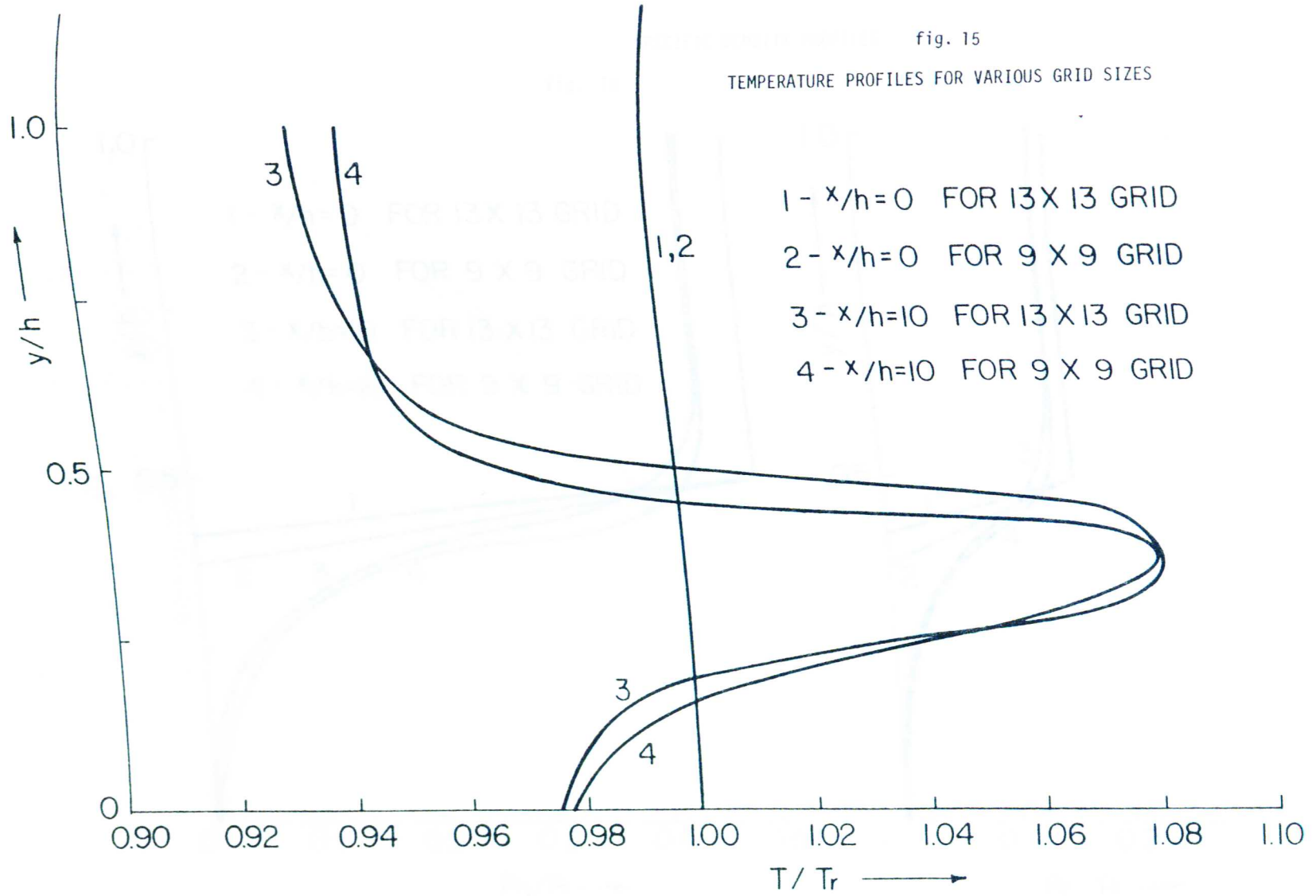
TEMPERATURE PROFILES FOR VARIOUS GRID SIZES

1 - $x/h=0$ FOR 13 X 13 GRID

2 - $x/h=0$ FOR 9 X 9 GRID

3 - $x/h=10$ FOR 13 X 13 GRID

4 - $x/h=10$ FOR 9 X 9 GRID



SPECIFIC DENSITY PROFILES

fig. 16

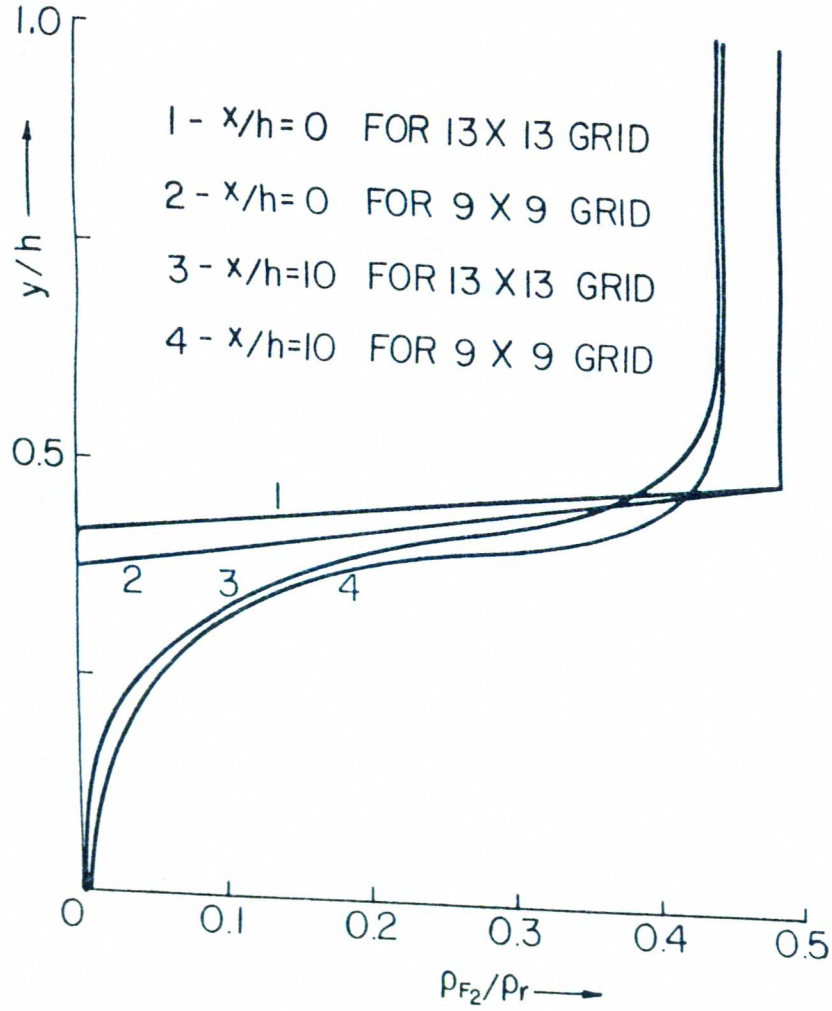
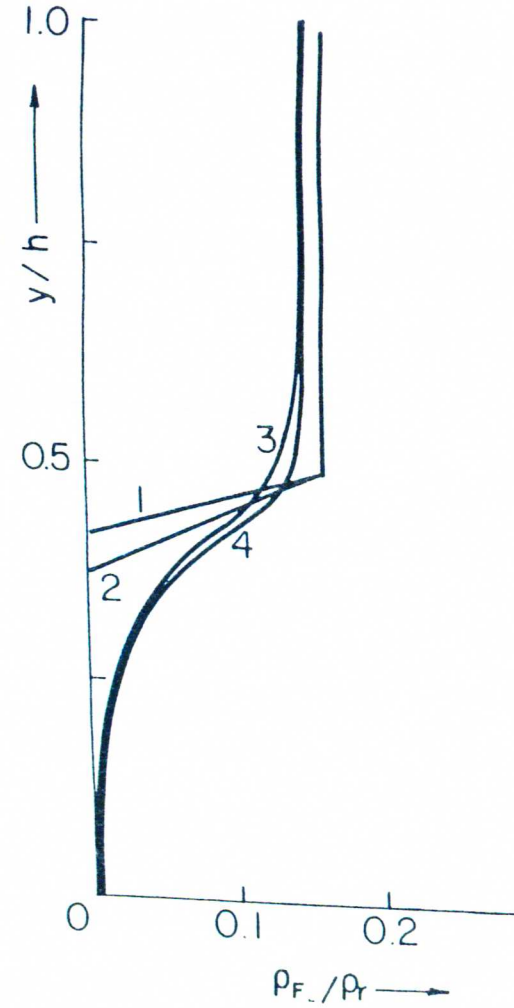
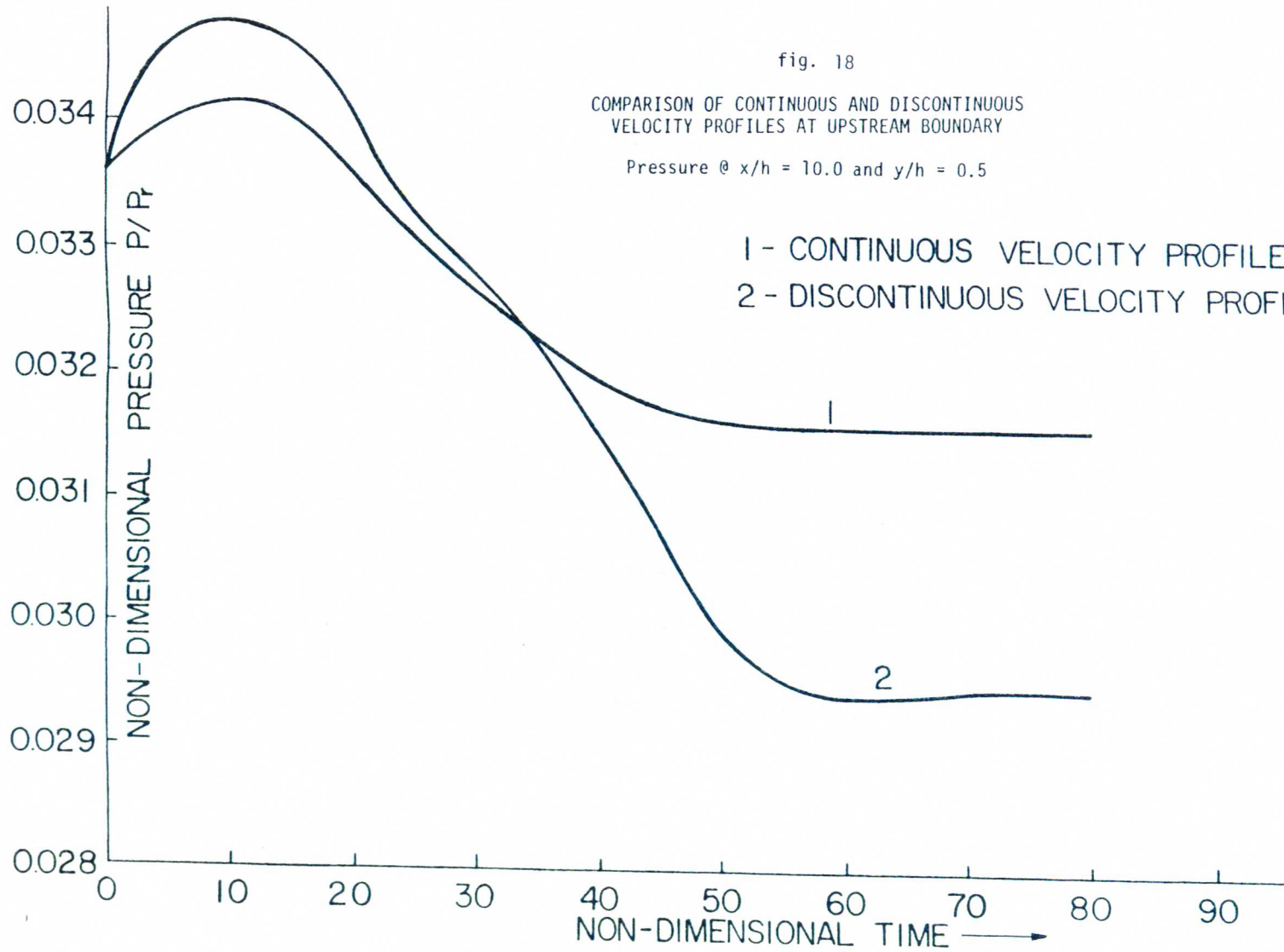


fig. 17





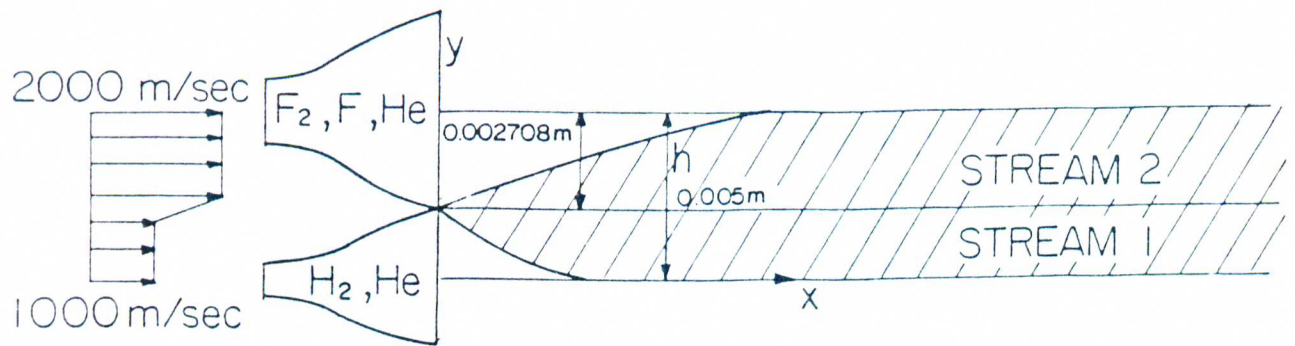


fig. 19
NOZZLE CONFIGURATION

	STREAM 1	STREAM 2
$P \text{ n/m}^2$	500	500
$T \text{ }^\circ\text{K}$	150	150
$\rho \text{ Kg/m}^3$	1.2862×10^{-3}	2.4514×10^{-3}
$\rho_{F_2} \text{ Kg/m}^3$	—	7.3128×10^{-4}
$\rho_{H_2} \text{ Kg/m}^3$	3.2328×10^{-4}	—
$\rho_F \text{ Kg/m}^3$	—	2.4376×10^{-4}
$\rho_H \text{ Kg/m}^3$	—	—
$\rho_{He} \text{ Kg/m}^3$	9.6288×10^{-4}	1.4764×10^{-3}

INITIAL CONDITIONS

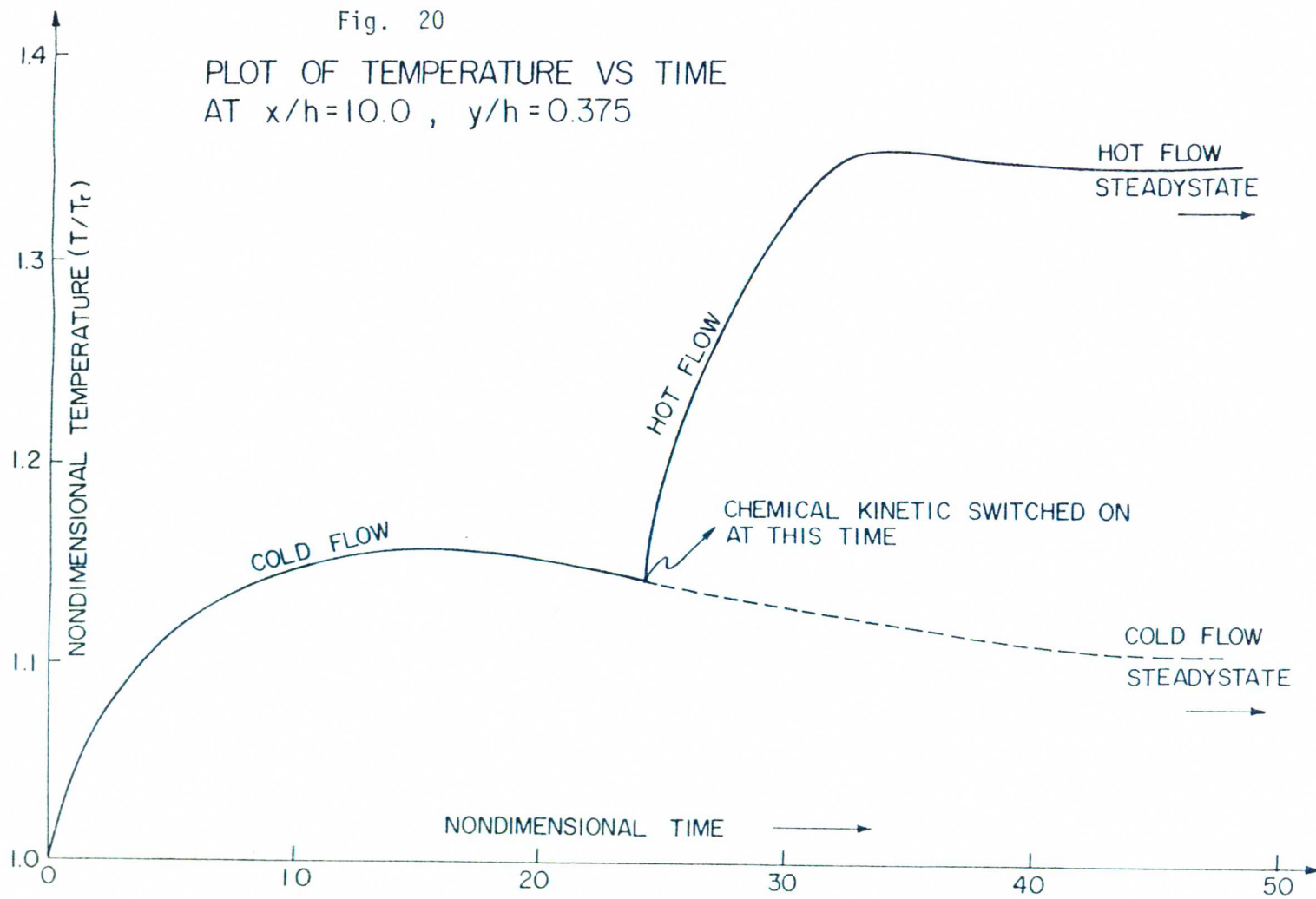
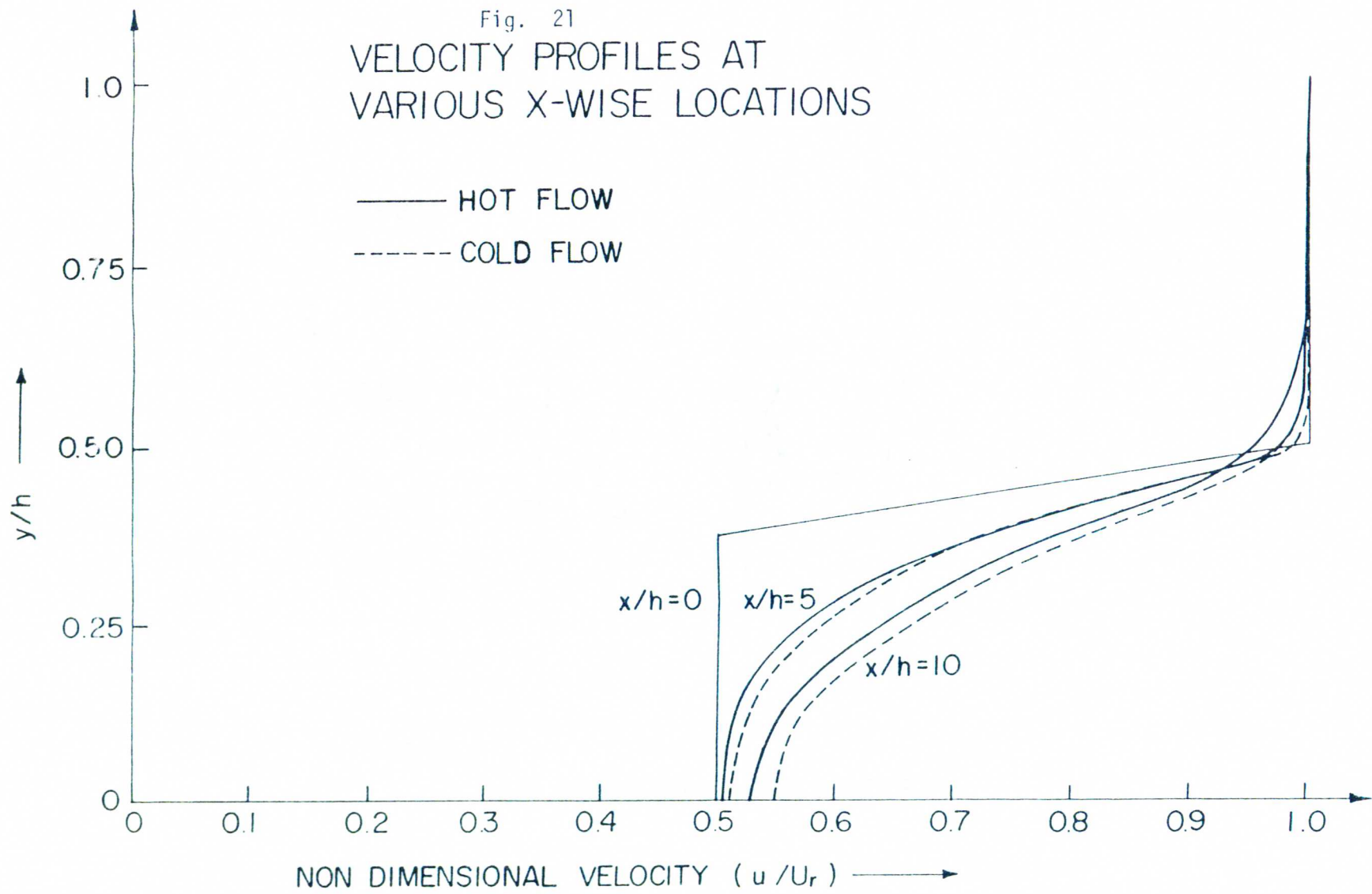


Fig. 21
VELOCITY PROFILES AT
VARIOUS X-WISE LOCATIONS



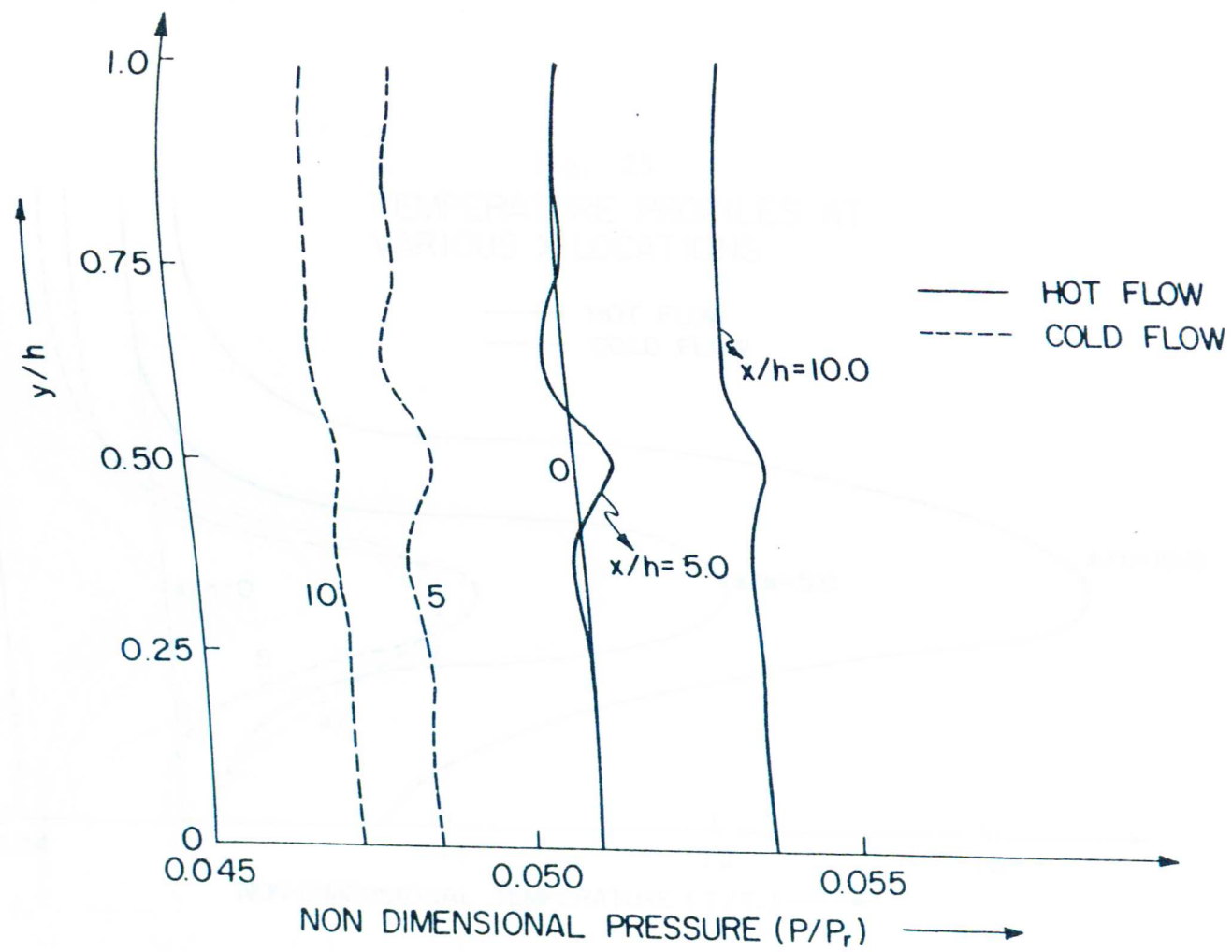
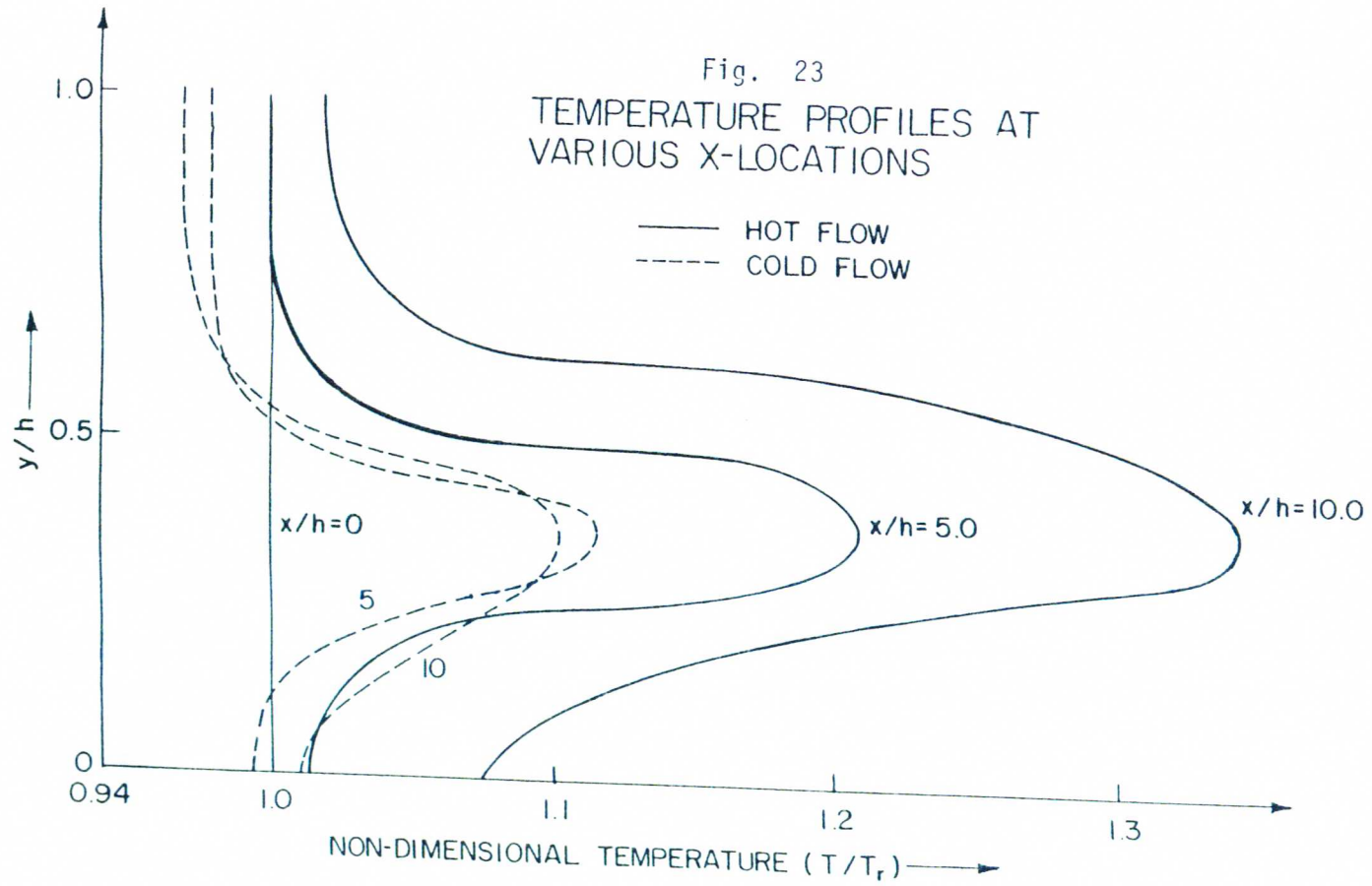
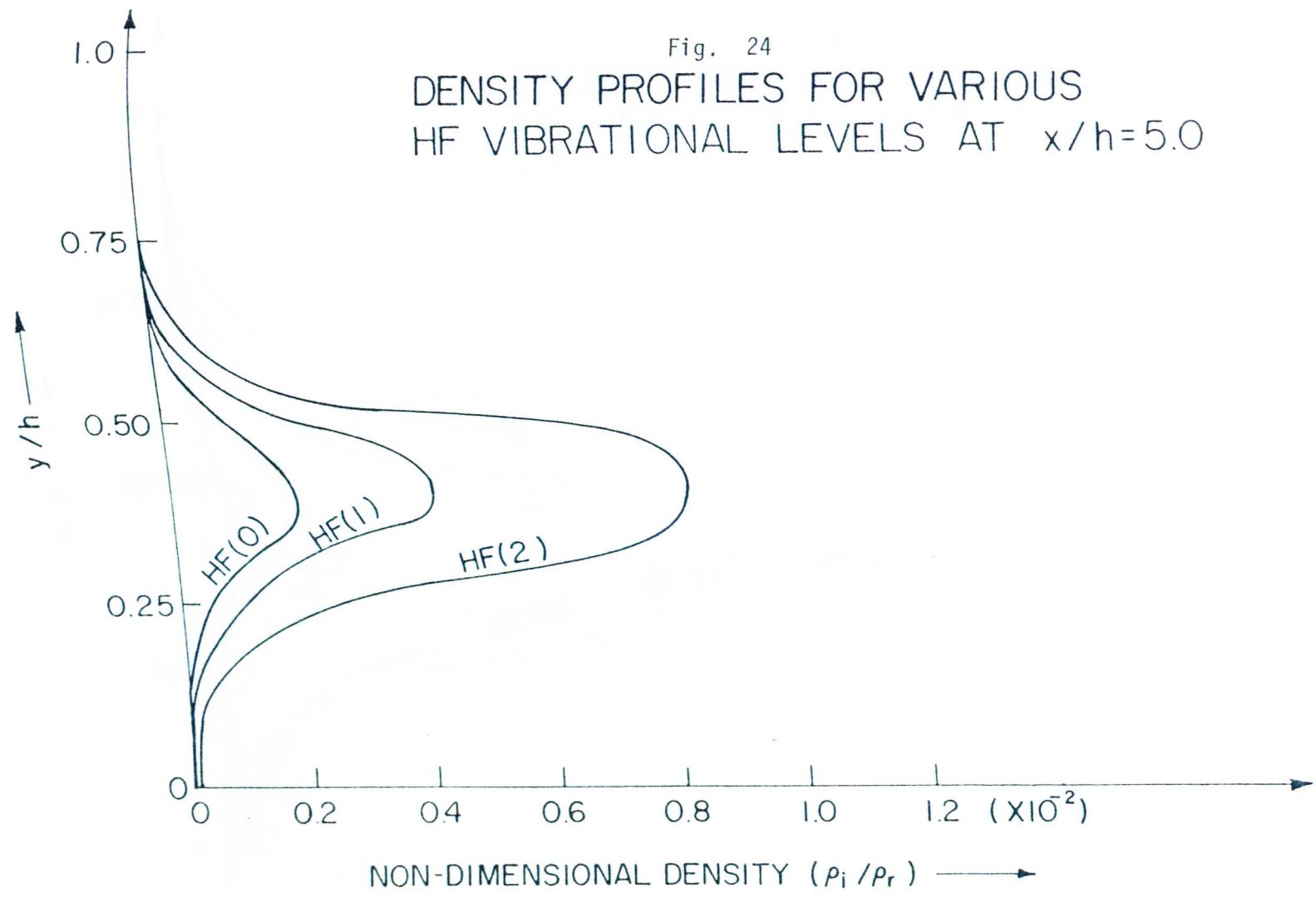


Fig. 22 -- Steady state pressure profiles at various x-wise locations





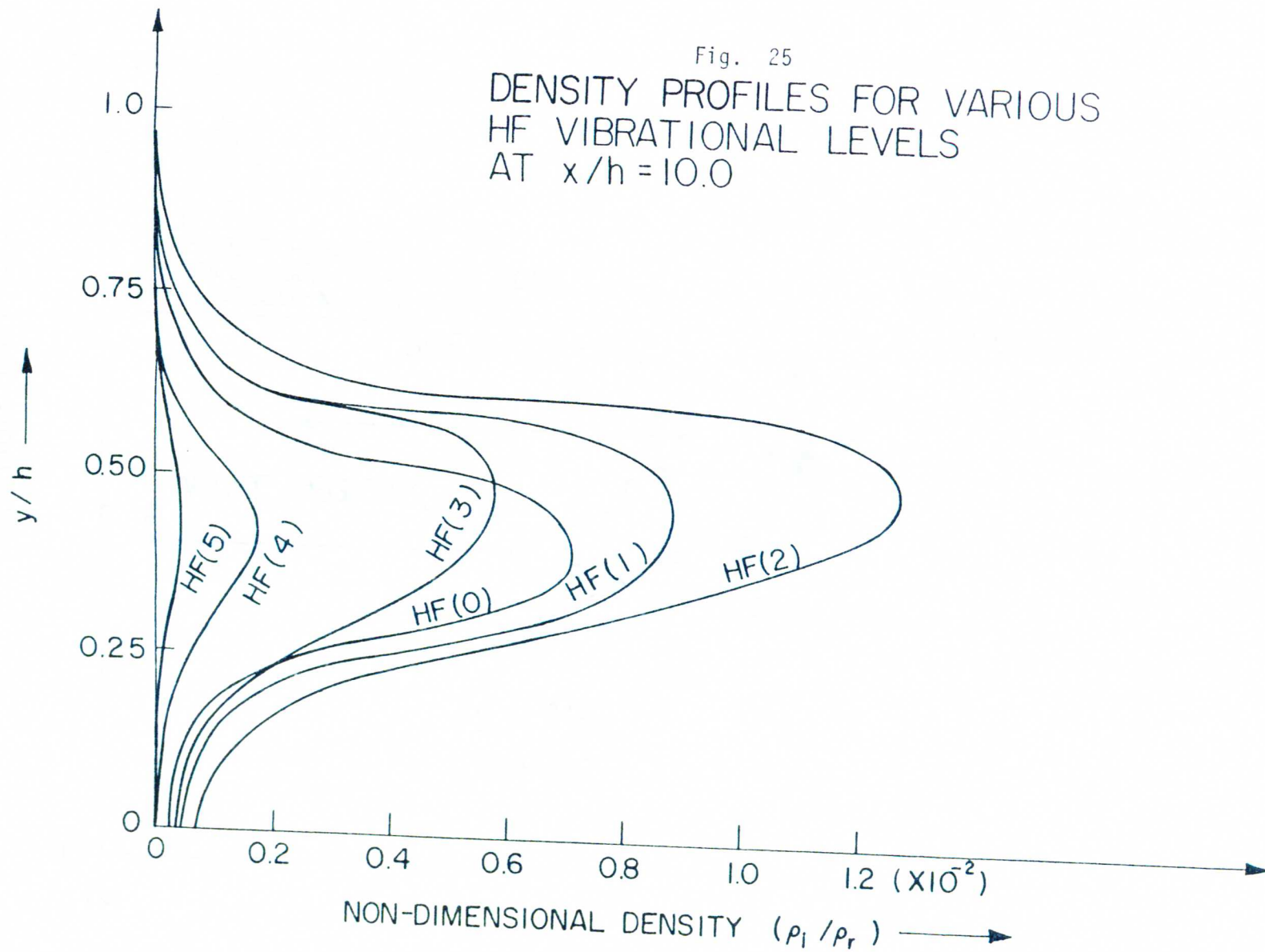


Fig. 26 -- Growth of the reaction zone; comparison of present calculations with experiment

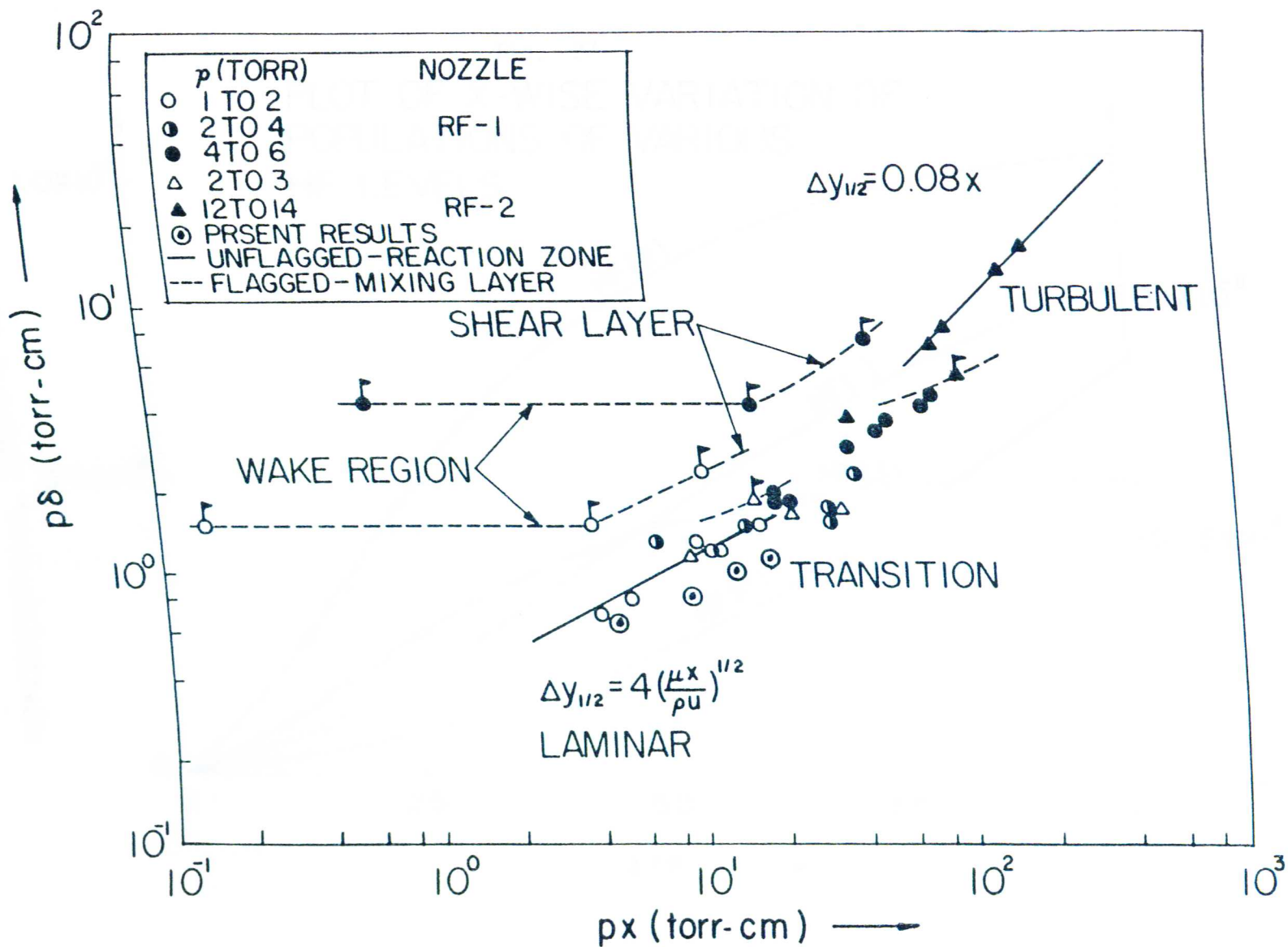


Fig. 27

PLOT OF X-WISE VARIATION OF POPULATIONS OF VARIOUS HF LEVELS

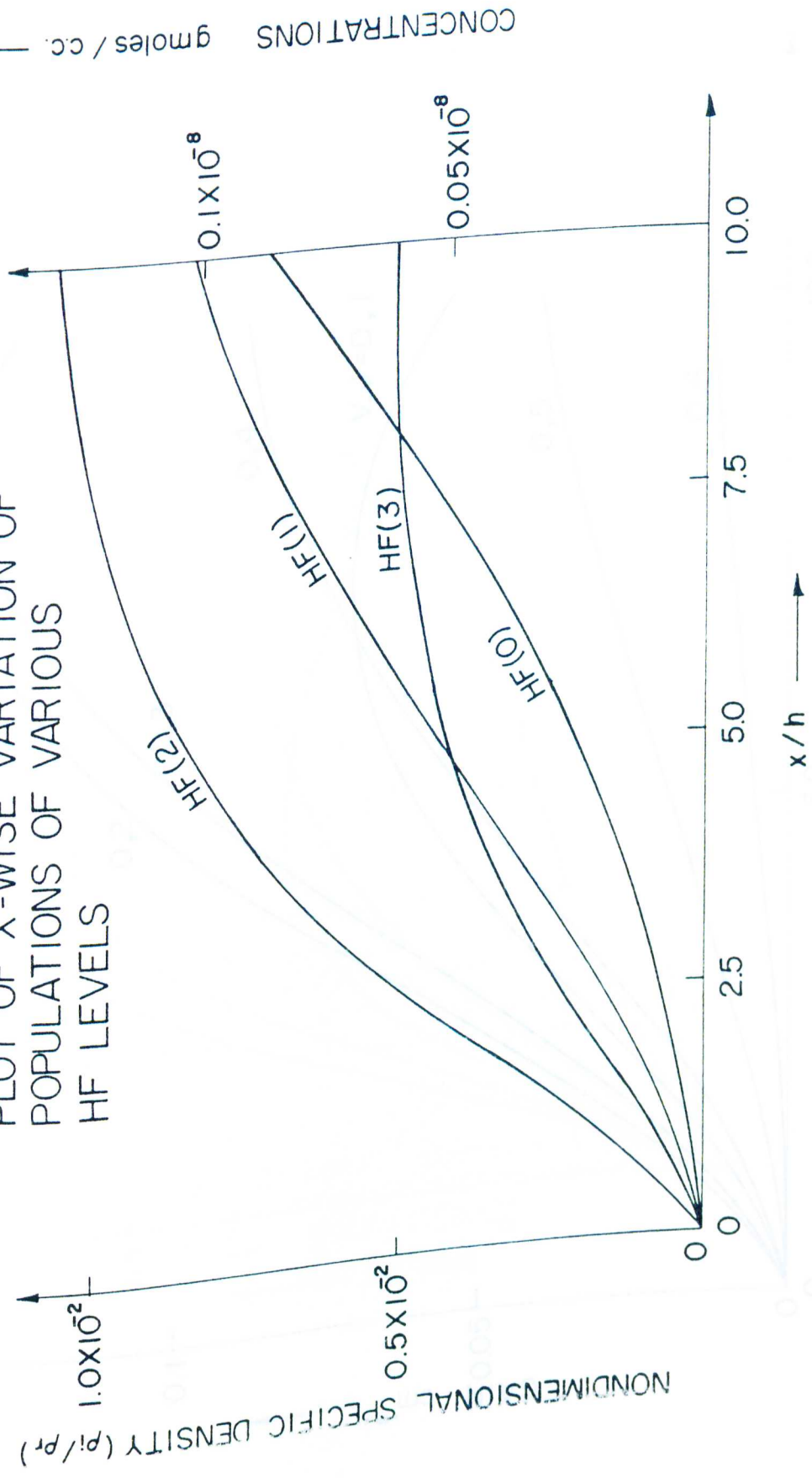
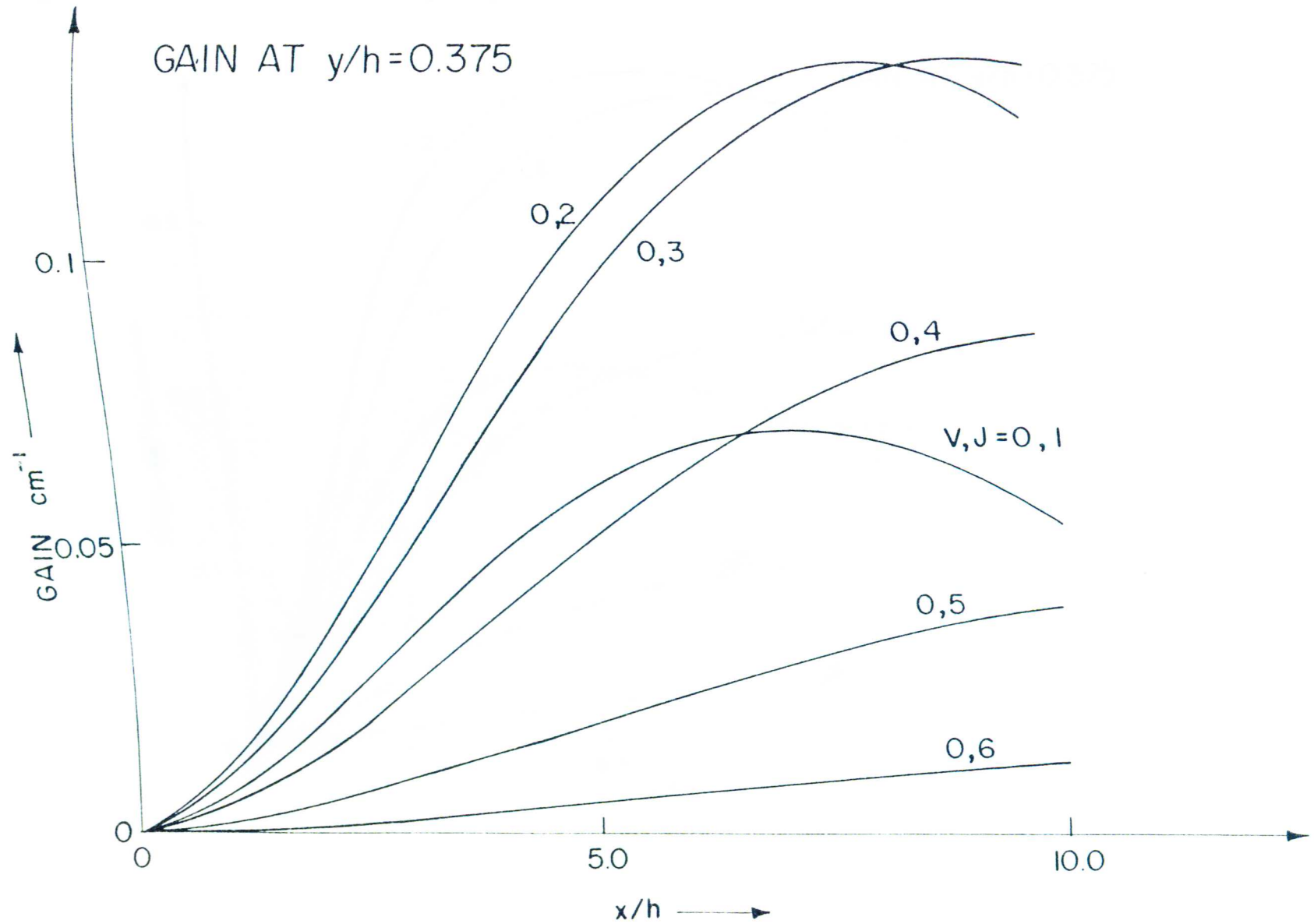
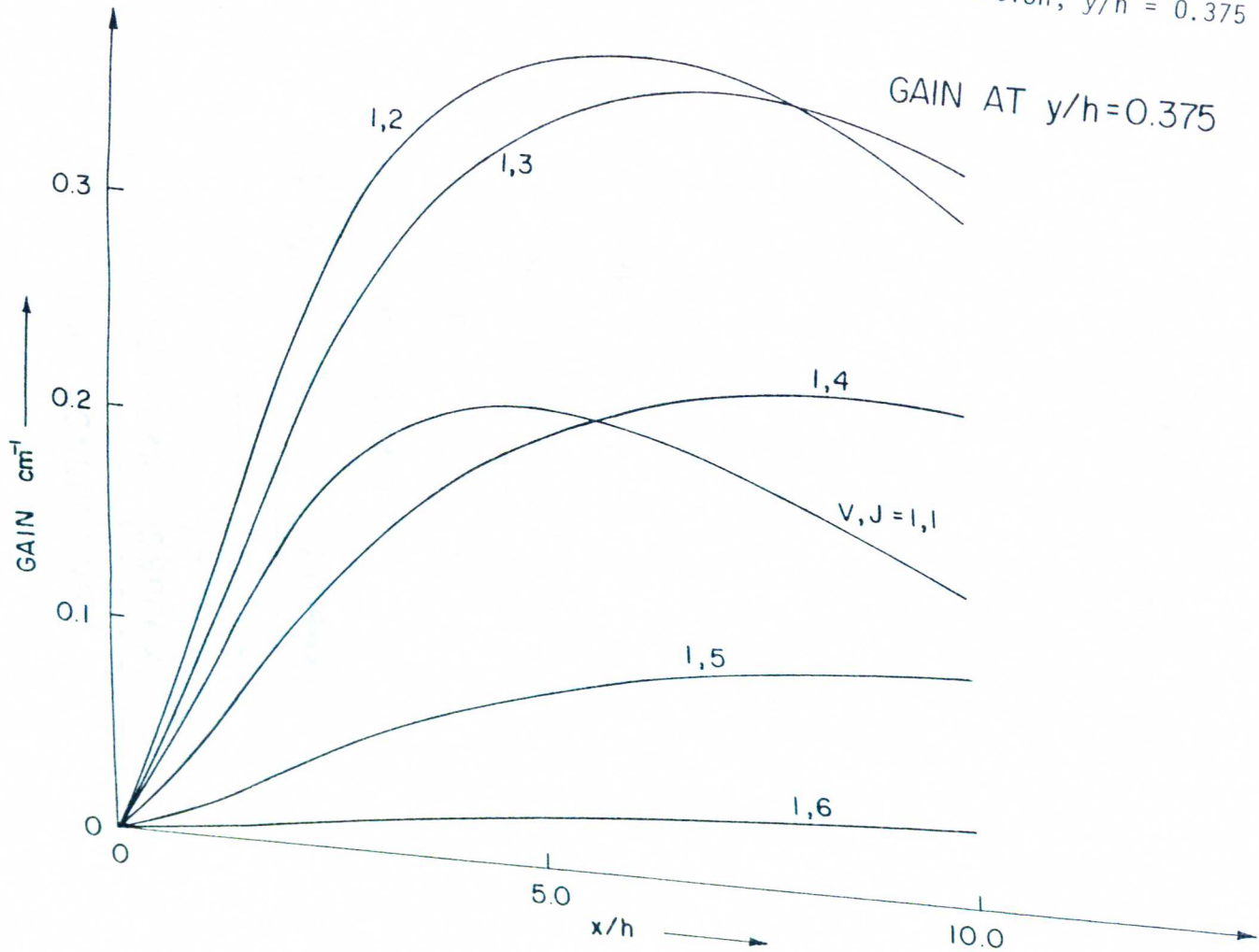


Fig. 28 -- Variation of small signal gain in flow direction; 1 - 0 transition, $y/h = 0.375$



120

Fig. 29 -- Variation of small signal gain in flow direction; 2-1 transition, $y/h = 0.375$



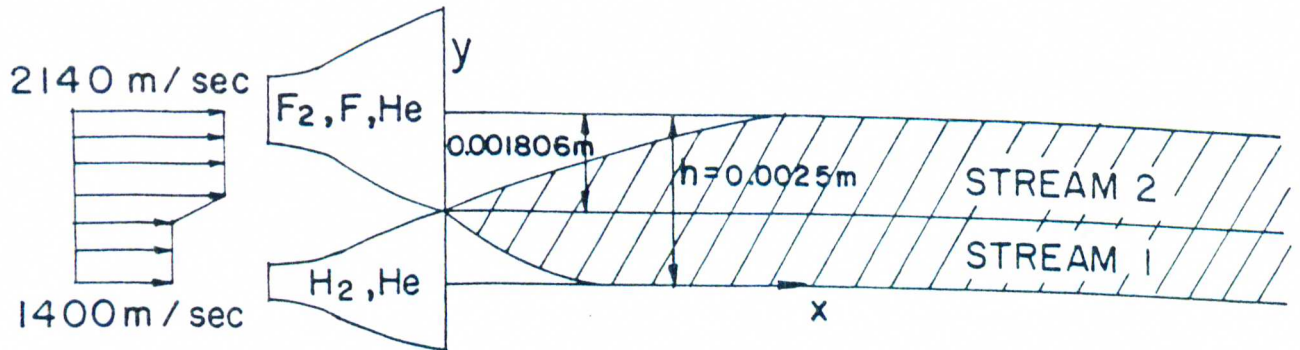


Fig. 30

NOZZLE CONFIGURATION

	STREAM 1	STREAM 2
$P \text{ n/m}^2$	666.61	666.61
$T \text{ }^\circ\text{K}$	110	400
$\rho \text{ Kg/m}^3$	1.5054×10^{-3}	1.6741×10^{-3}
$\rho_{F_2} \text{ Kg/m}^3$	—	—
$\rho_{H_2} \text{ Kg/m}^3$	1.4327×10^{-3}	—
$\rho_F \text{ Kg/m}^3$	—	1.1044×10^{-3}
$\rho_H \text{ Kg/m}^3$	—	—
$\rho_{He} \text{ Kg/m}^3$	7.2698×10^{-5}	5.6966×10^{-4}

INITIAL CONDITIONS

Fig. 31 -- Pressure versus longitudinal distance; comparison between present results and method of Refs. 20 and 29 - strongly reacting case

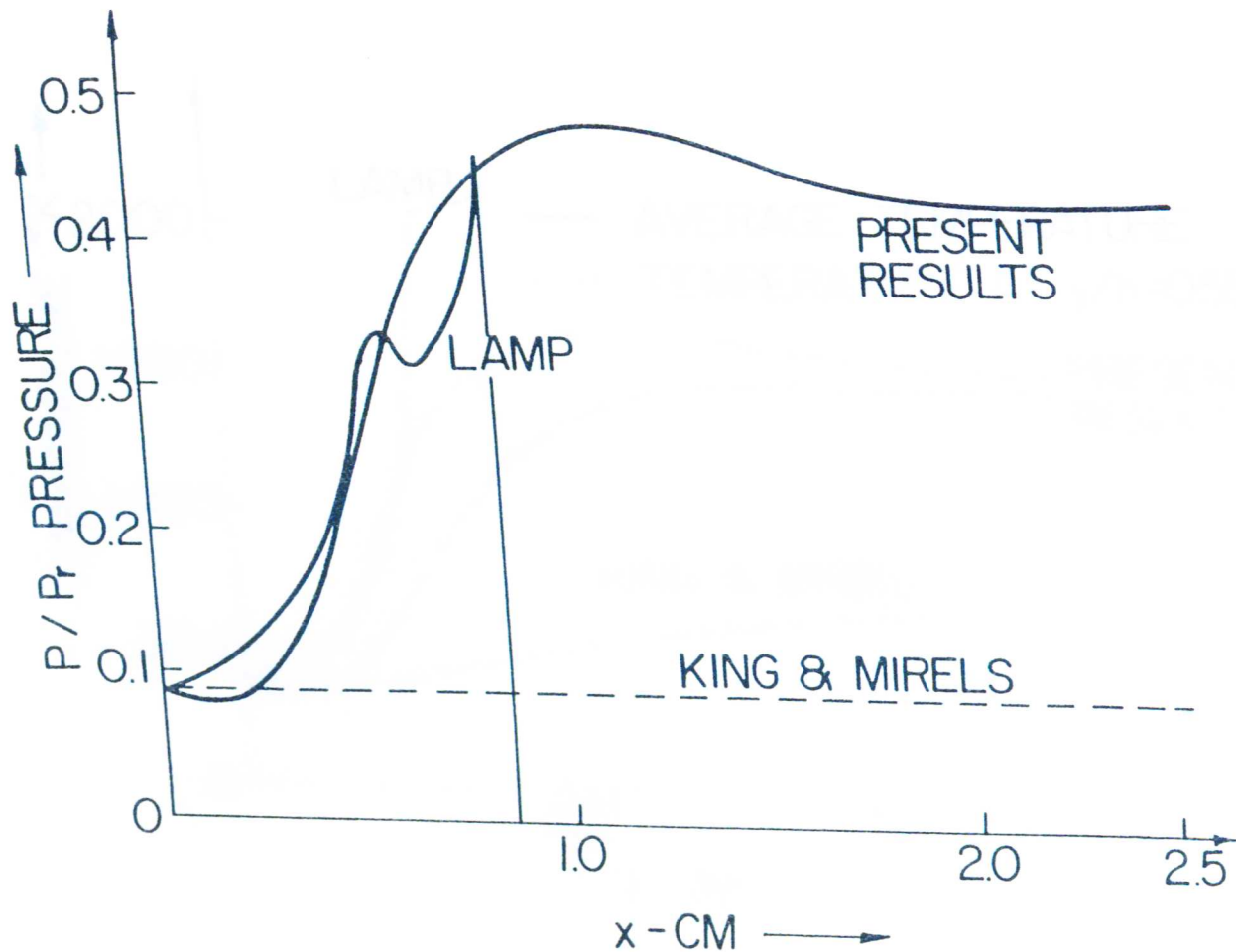


Fig. 32 -- Temperature versus longitudinal distance; comparison between present results and method of Refs. 20 and 29 - strongly reacting case

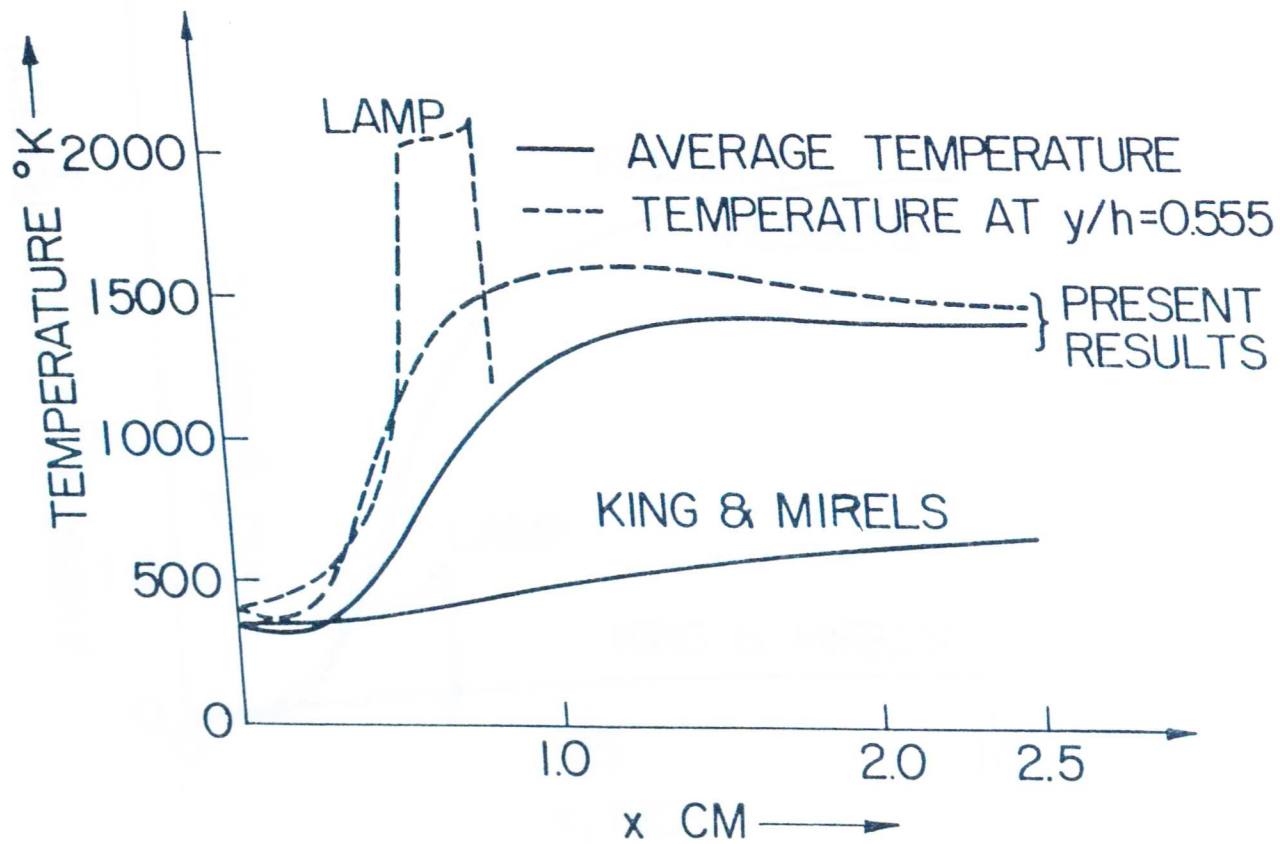


Fig. 33 -- HF(0) density versus longitudinal distance; comparison between present results and methods of Refs. 20 and 29 - strongly reacting case

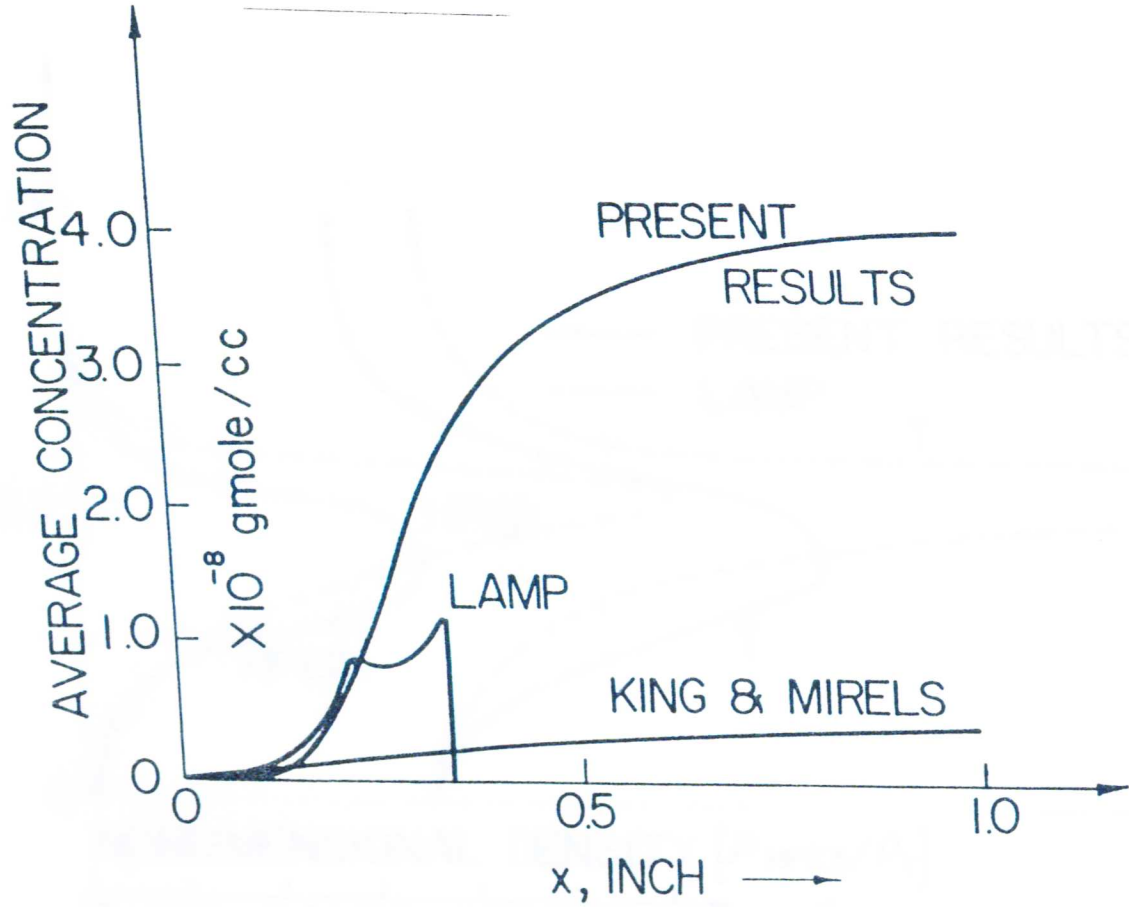
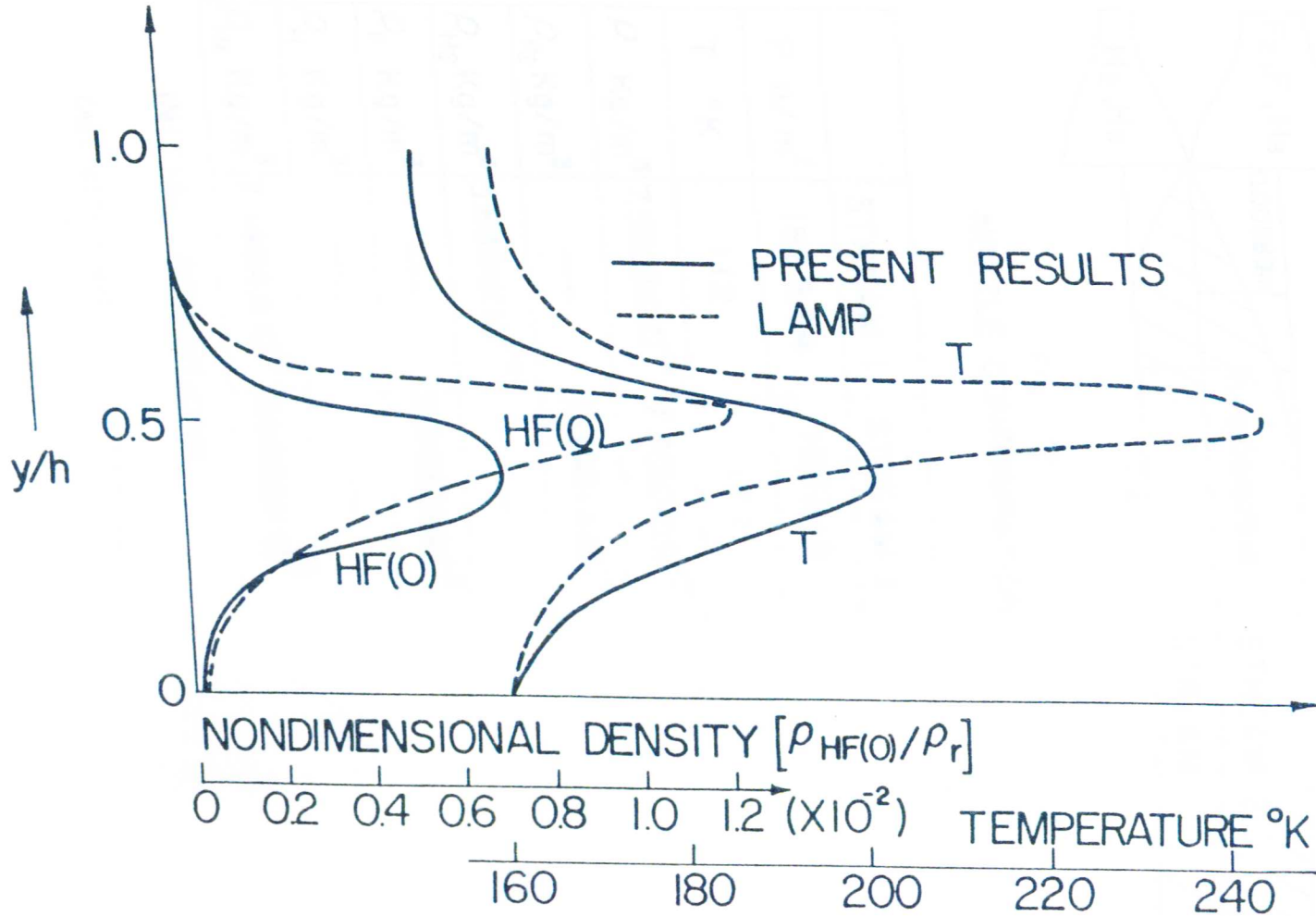


Fig. 34 -- HF(0) and temperature profiles; comparison between present results and methods of Ref. 29 - weakly reacting case



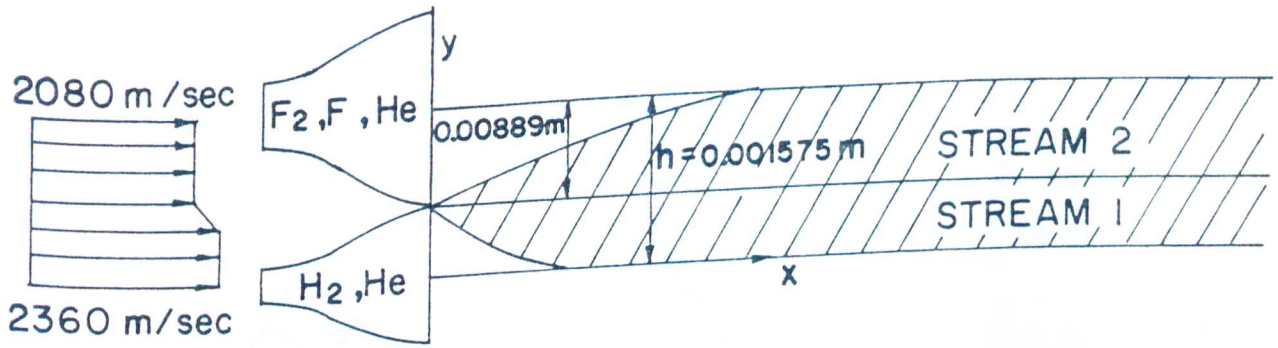
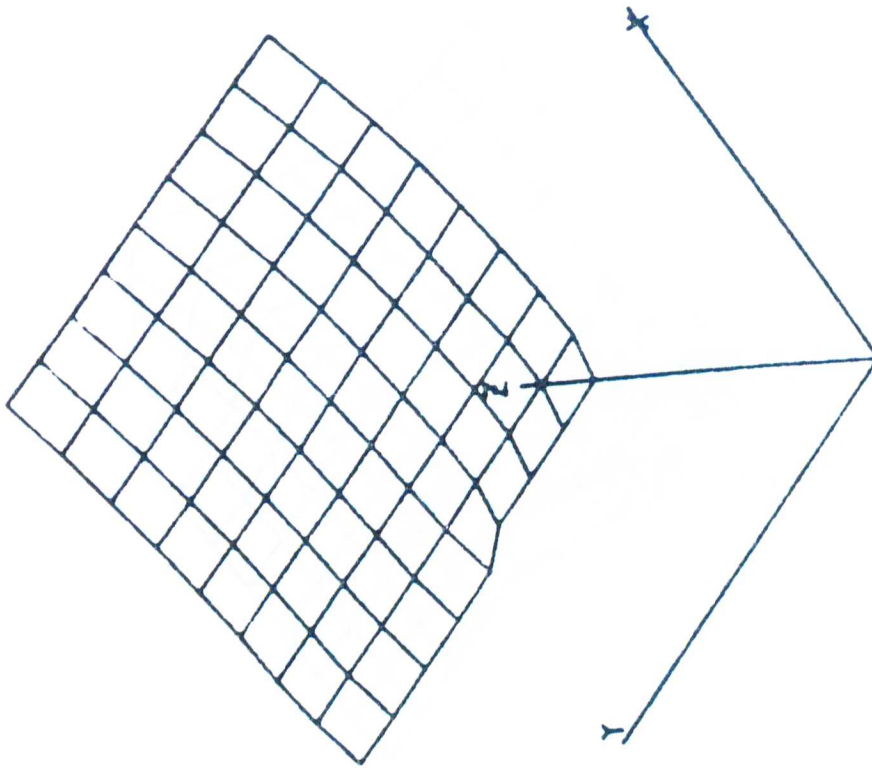


Fig. 35
NOZZLE CONFIGURATION

	STREAM 1	STREAM 2
P n/m^2	1839.84	1653.19
T $^{\circ}K$	112	177
ρ Kg/m^3	7.5303×10^{-3}	7.3010×10^{-3}
ρ_{F_2} Kg/m^3	—	9.4651×10^{-4}
ρ_{H_2} Kg/m^3	3.8391×10^{-4}	—
ρ_F Kg/m^3	—	2.3663×10^{-3}
ρ_H Kg/m^3	—	—
ρ_{He} Kg/m^3	7.1464×10^{-3}	3.9882×10^{-3}

INITIAL CONDITIONS

CASE WITH HIGHER CAVITY PRESSURE

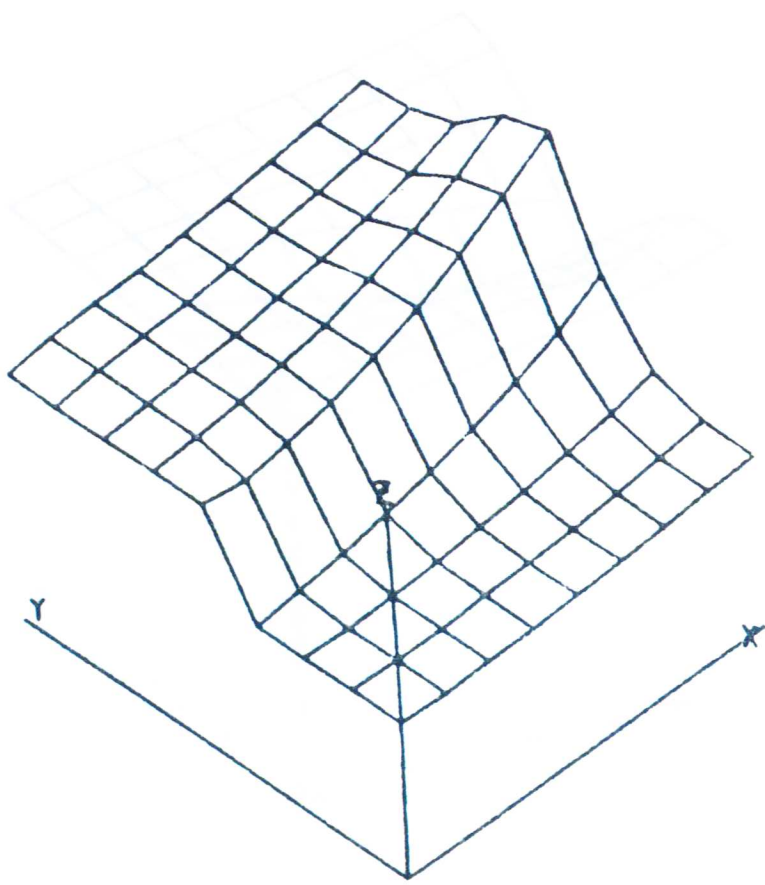


VIEWING ANGLE
 THETA = 45.0
 PHI = 225.0
 OPTIONS: A, U, 9

DIMENSION
 X: 1 STEP 1 UNTIL 9
 Y: 1 STEP 1 UNTIL 9
 Z: C.07
 .05]

REGION PLOTTED
 1 STEP 1 UNTIL 9
 1 STEP 1 UNTIL 9
 C.07
 .000]

Fig. 36 -- Pressure surface; note different viewing angle



VIEWING ANGLE
THETA = 45.0
PHI = 225.0
OPTIONS: A, U, 9

DIMENSION
X: 1 STEP 1 UNTIL 9
Y: 1 STEP 1 UNTIL 9
Z: [1.45
.82]

REGION PLOTTED
1 STEP 1 UNTIL 9
1 STEP 1 UNTIL 9
[1.45
.0.0]

Fig. 37 -- Temperature surface; note different viewing angle

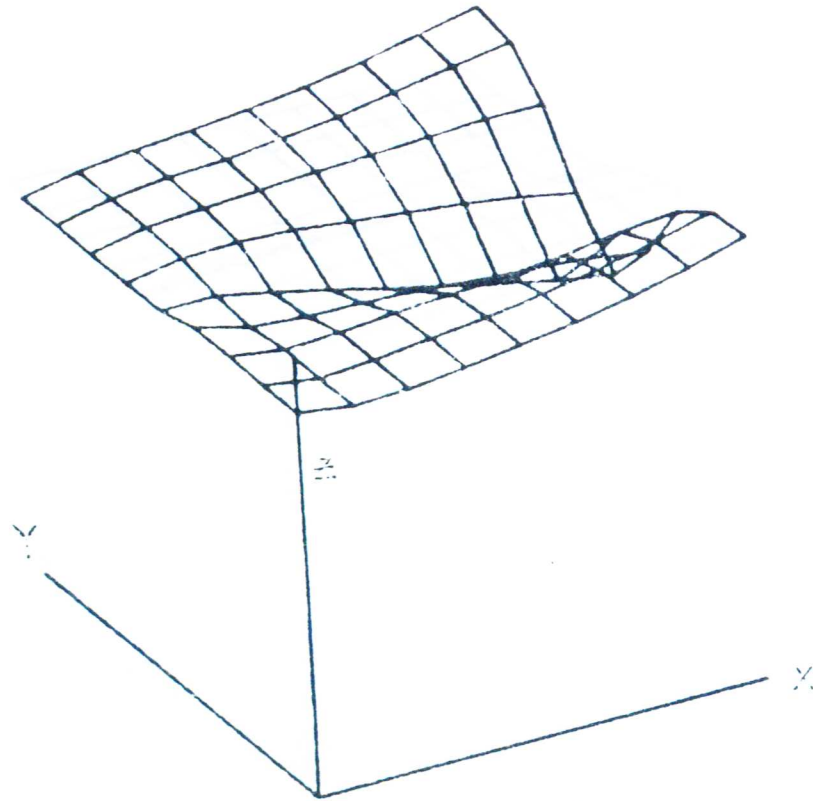


Fig. 38a -- Global density surface

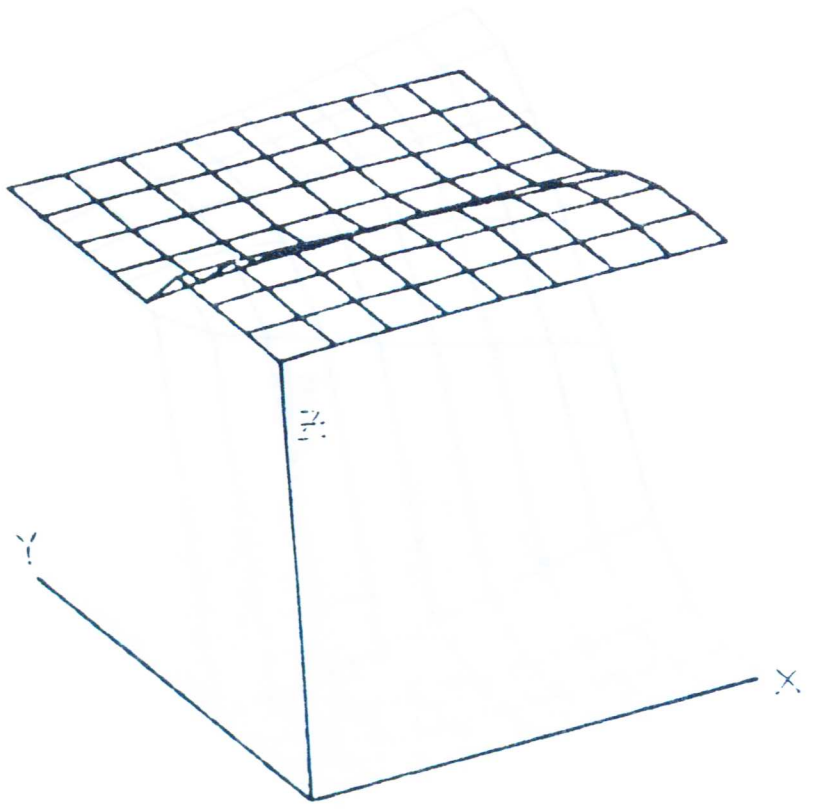


Fig. 38b -- u velocity surface

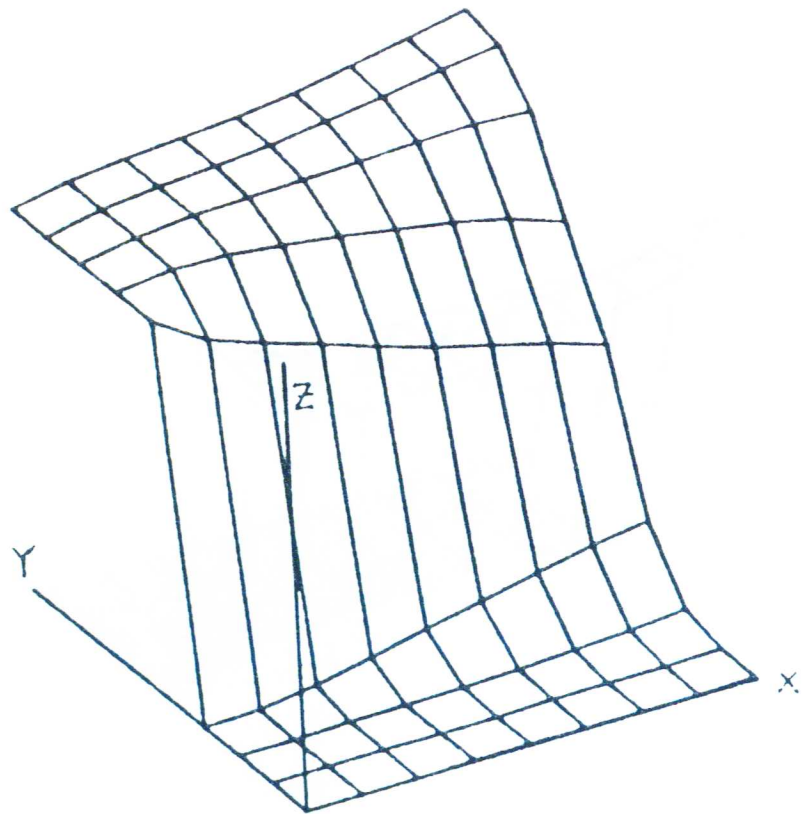


Fig. 39 -- Species density - F_2

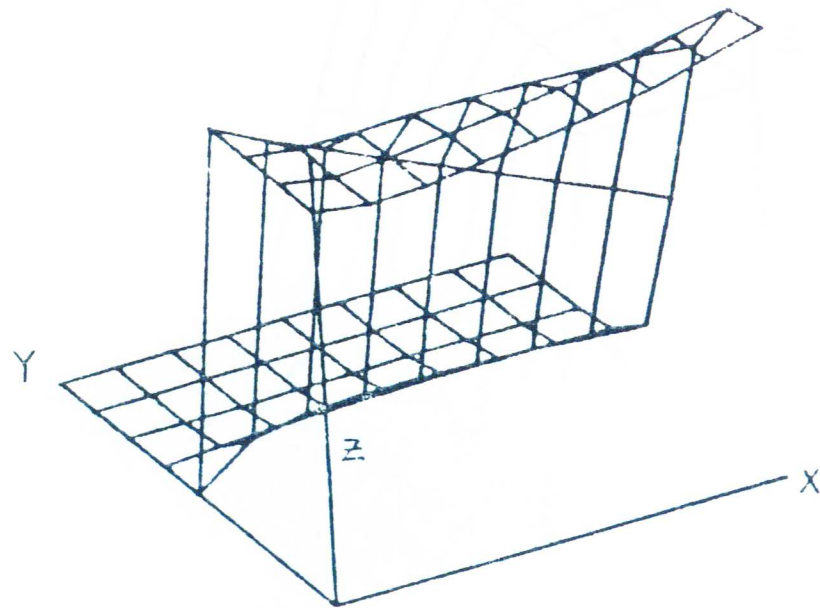


Fig. 40 -- Species density - H_2

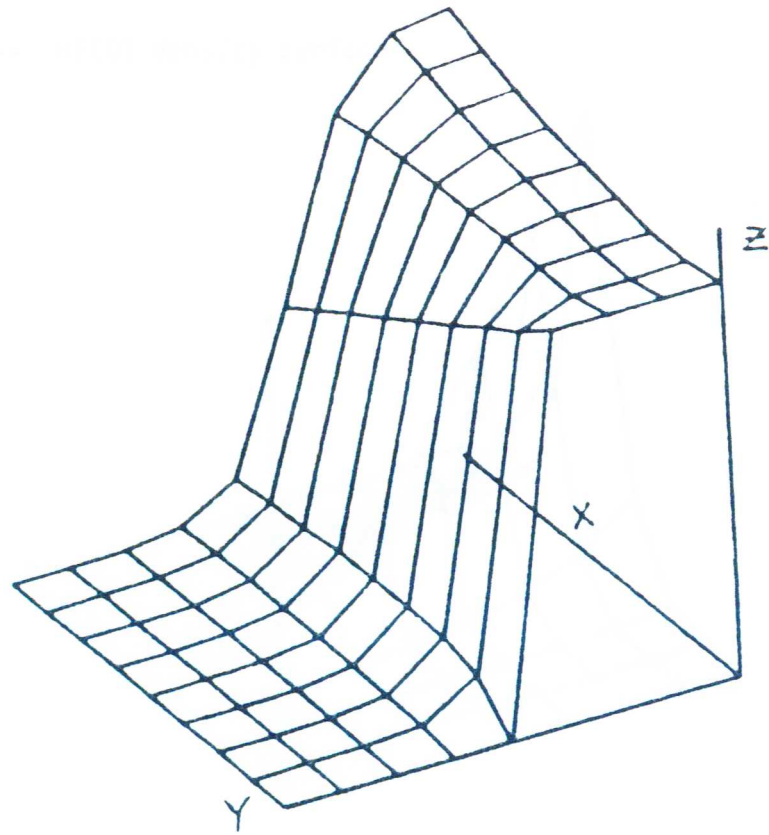
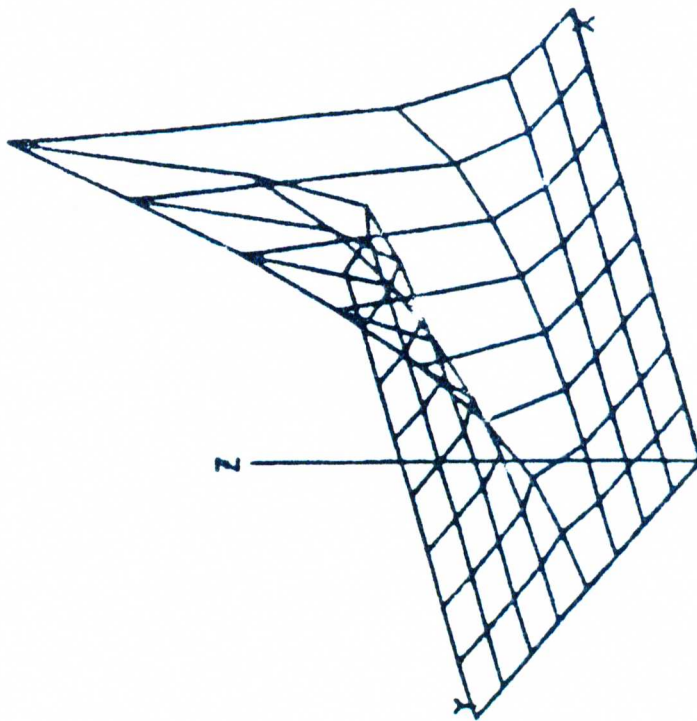


Fig. 41 -- Species density - H_2 . Note different viewing angle - $\theta = 60^\circ$ and $\phi = 150^\circ$

Fig. 42 -- HF(0) density surface



VIEWING ANGLE
 THETA = 60.0
 PHI = 240.0
 OPTIONS: A, U, S
 Z CHANGE: + .0

DIMENSION
 X: 1 STEP 1 UNTIL 9
 Y: 1 STEP 1 UNTIL 9
 Z: [.04
 .00]

REGION PLOTTED
 1 STEP 1 UNTIL 9
 1 STEP 1 UNTIL 9
 [.04
 .00]

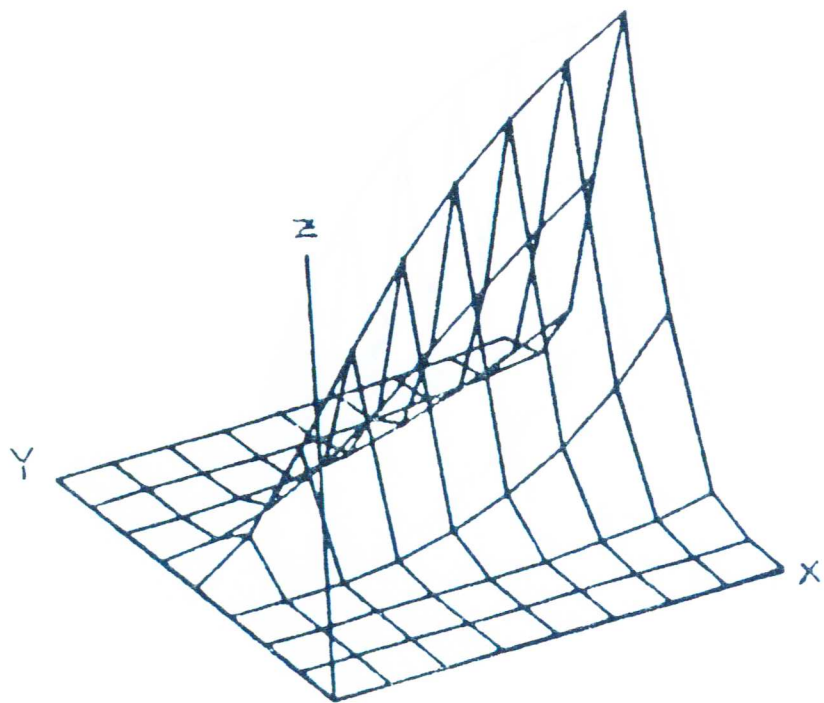
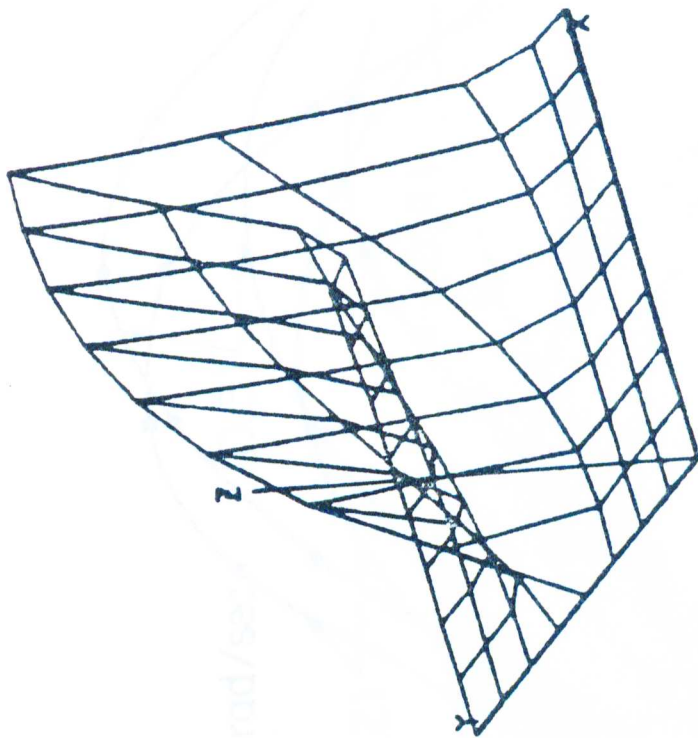


Fig. 43 -- HF(1) density surface

Fig. 44 -- HF(2) density surface

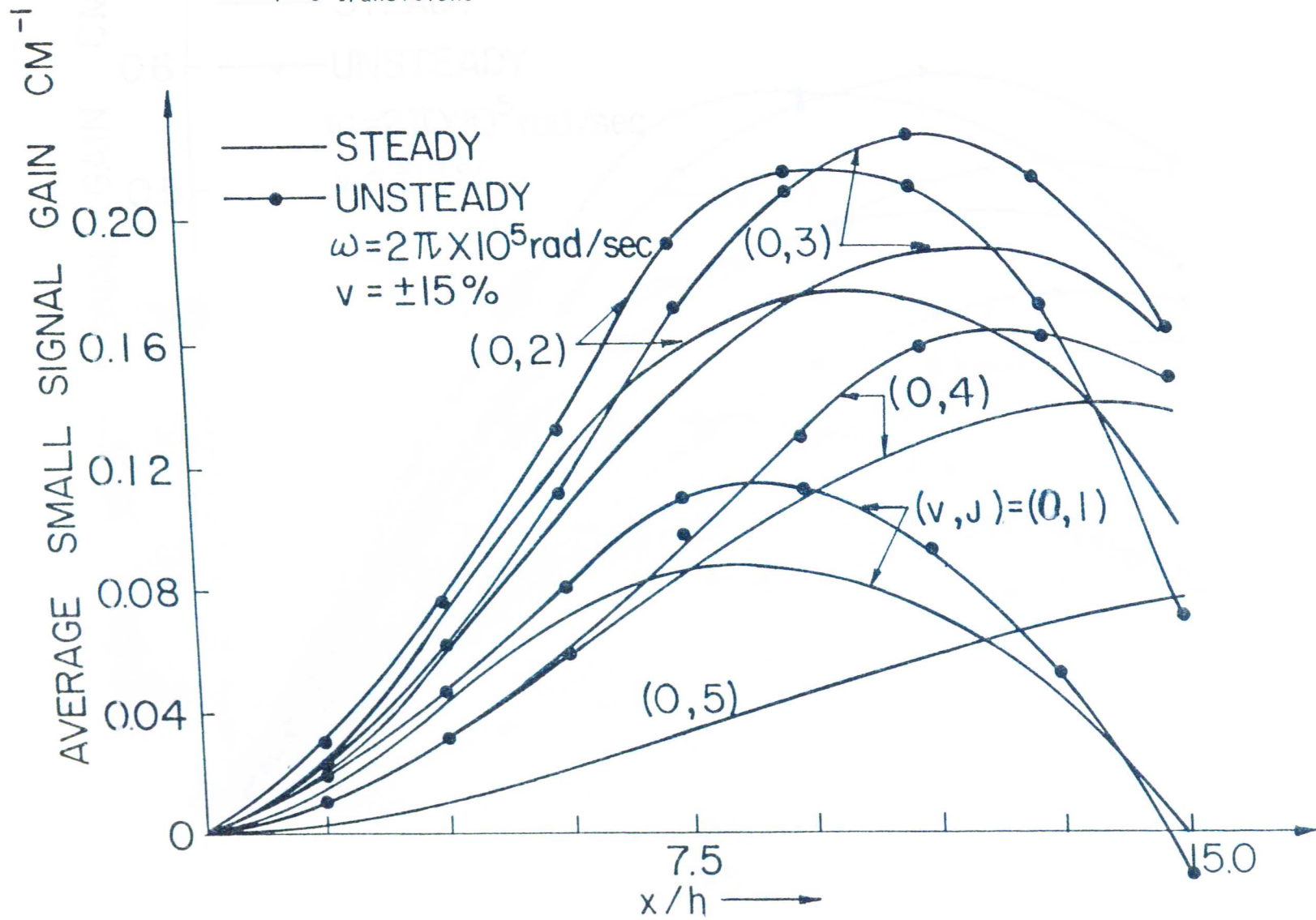


VIEWING ANGLE
 THETA = 60.0
 PHI = 240.0
 OPTIONS: A, U, S

DIMENSION
 X: 1 STEP 1 UNTIL 9
 Y: 1 STEP 1 UNTIL 9
 Z: C.02
 ..00

REGION PLOTTED
 1 STEP 1 UNTIL 9
 1 STEP 1 UNTIL 9
 C.02
 .0.00

Fig. 45 -- Comparison plot of averaged small signal gains between steady and unsteady cases:
 1-0 transitions



138

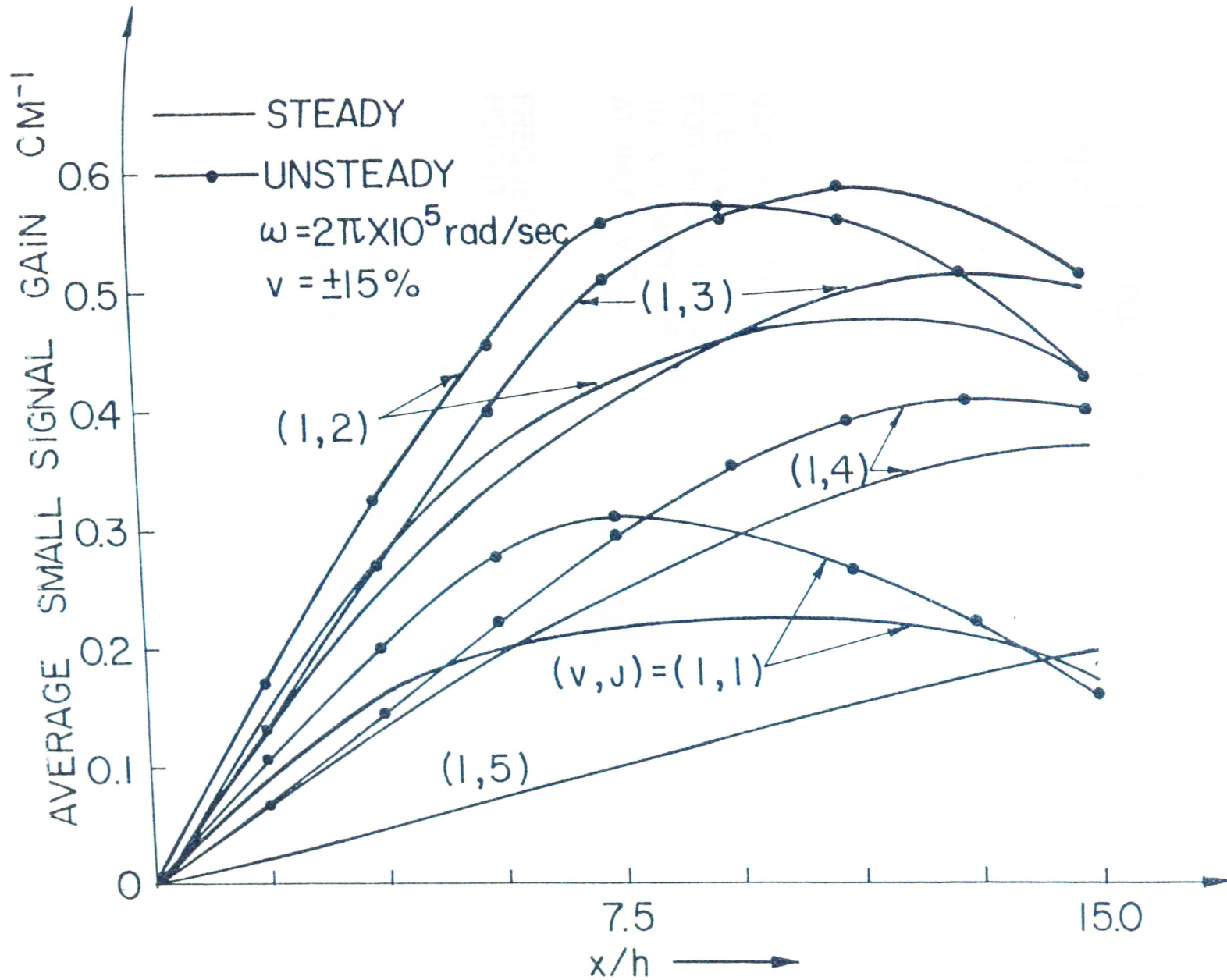
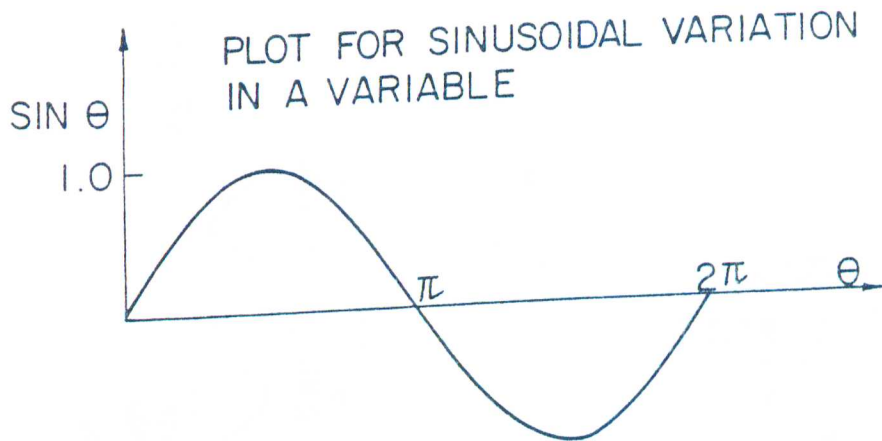
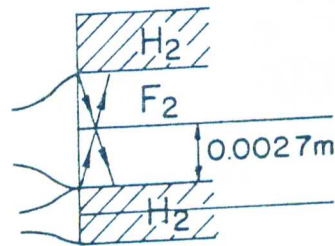


Fig. 46 -- Comparison plot of averaged small signal gains between steady and unsteady cases: 2-1 transitions



VARIOUS DIFFERENT
FREQUENCIES TRIED
FOR FLUCTUATIONS
IN X-COMPO. OF VEL.
AT INLET VIZ. u



FREQUENCY CALCULATION ACCORDING TO F_2 NOZZLE
HEIGHT

$$a = v/M = \frac{2000}{4.2362} = 472.12 \text{ M/SEC.}$$

$$T = 0.0054 / a = 1.1438 \times 10^{-5} \text{ SEC.}$$

$$\omega_3 = 2\pi / T = 5.4934 \times 10^5 \text{ RAD/SEC.}$$

$$\Delta t = T/30$$

Fig. 47

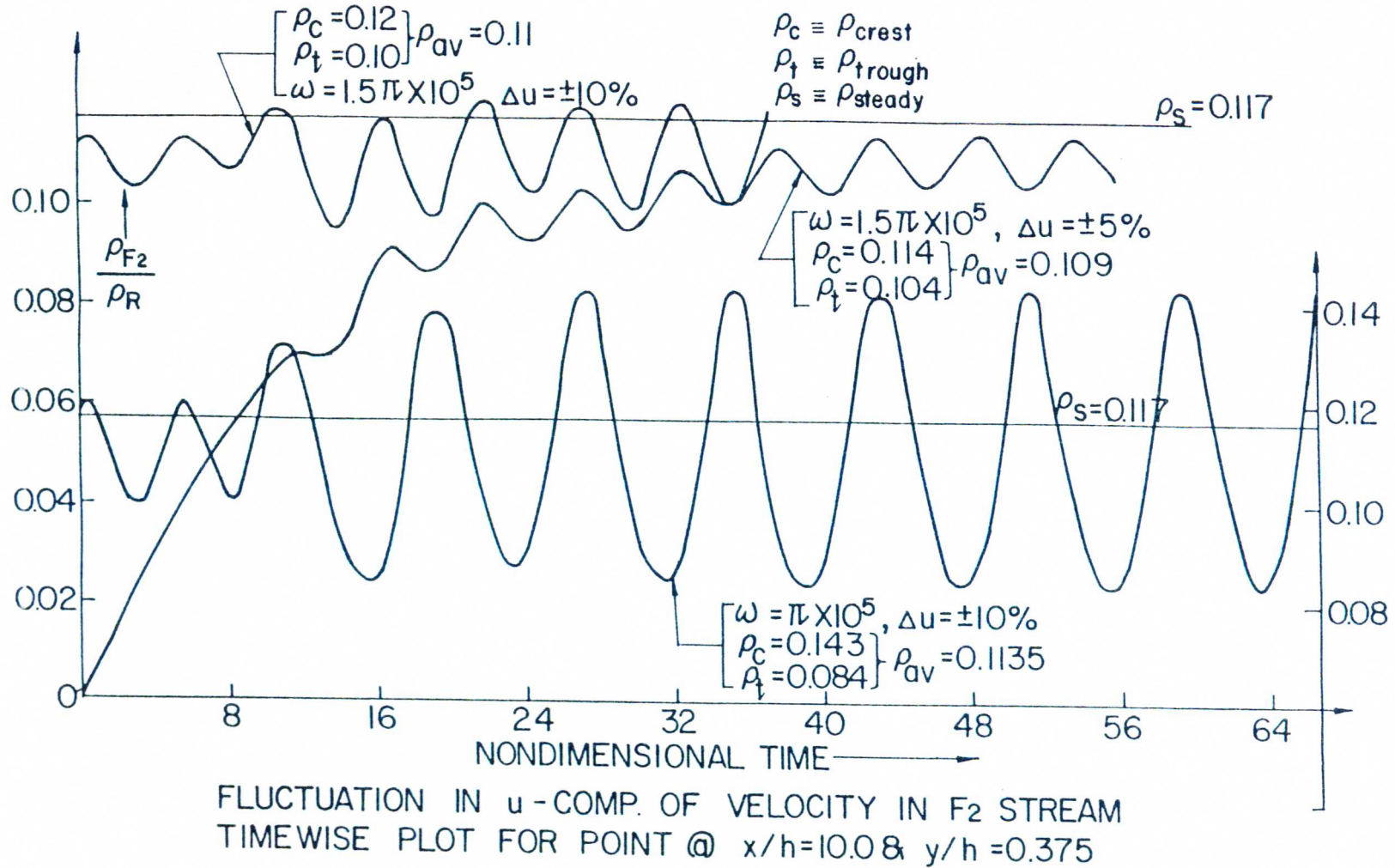


Fig. 48

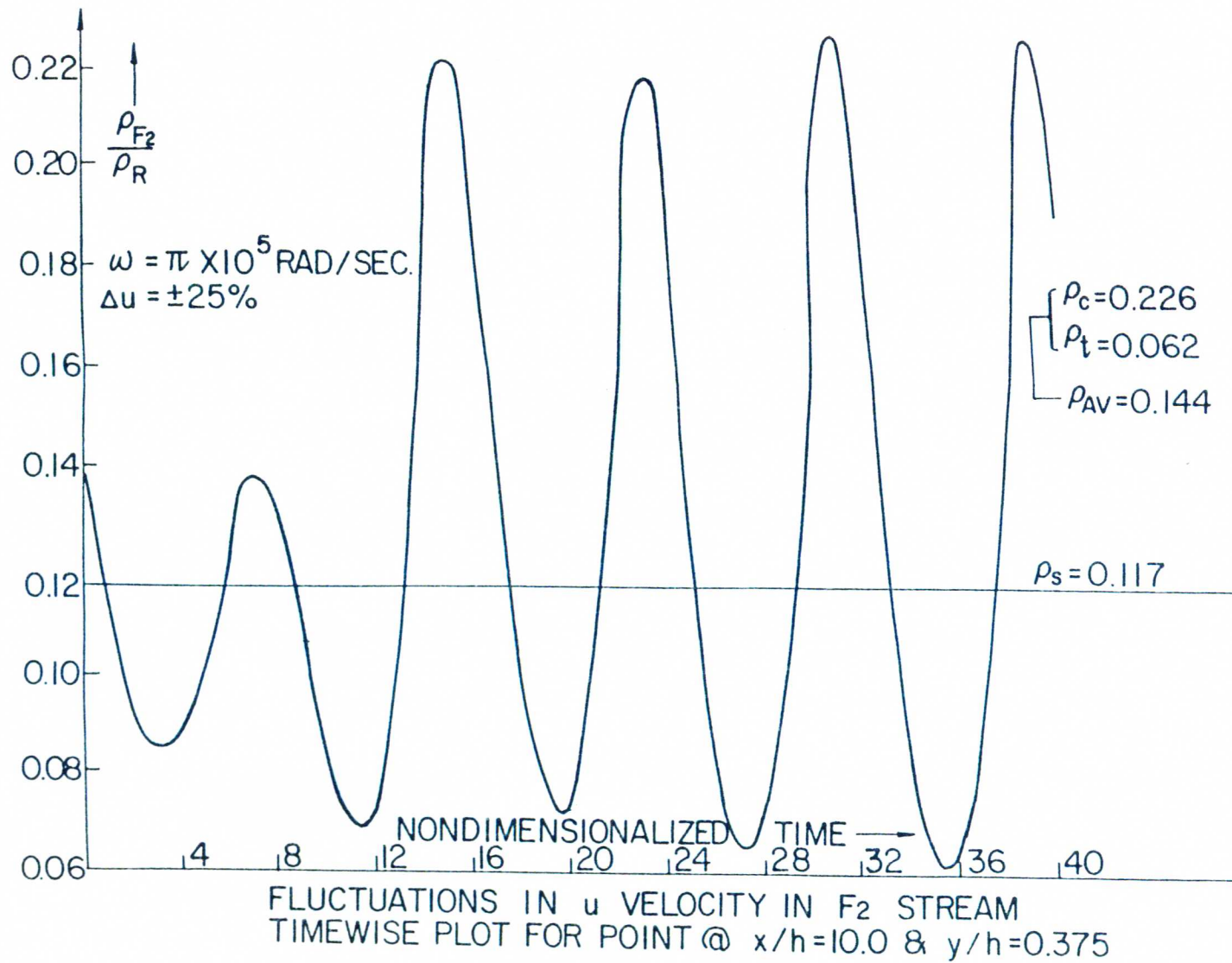
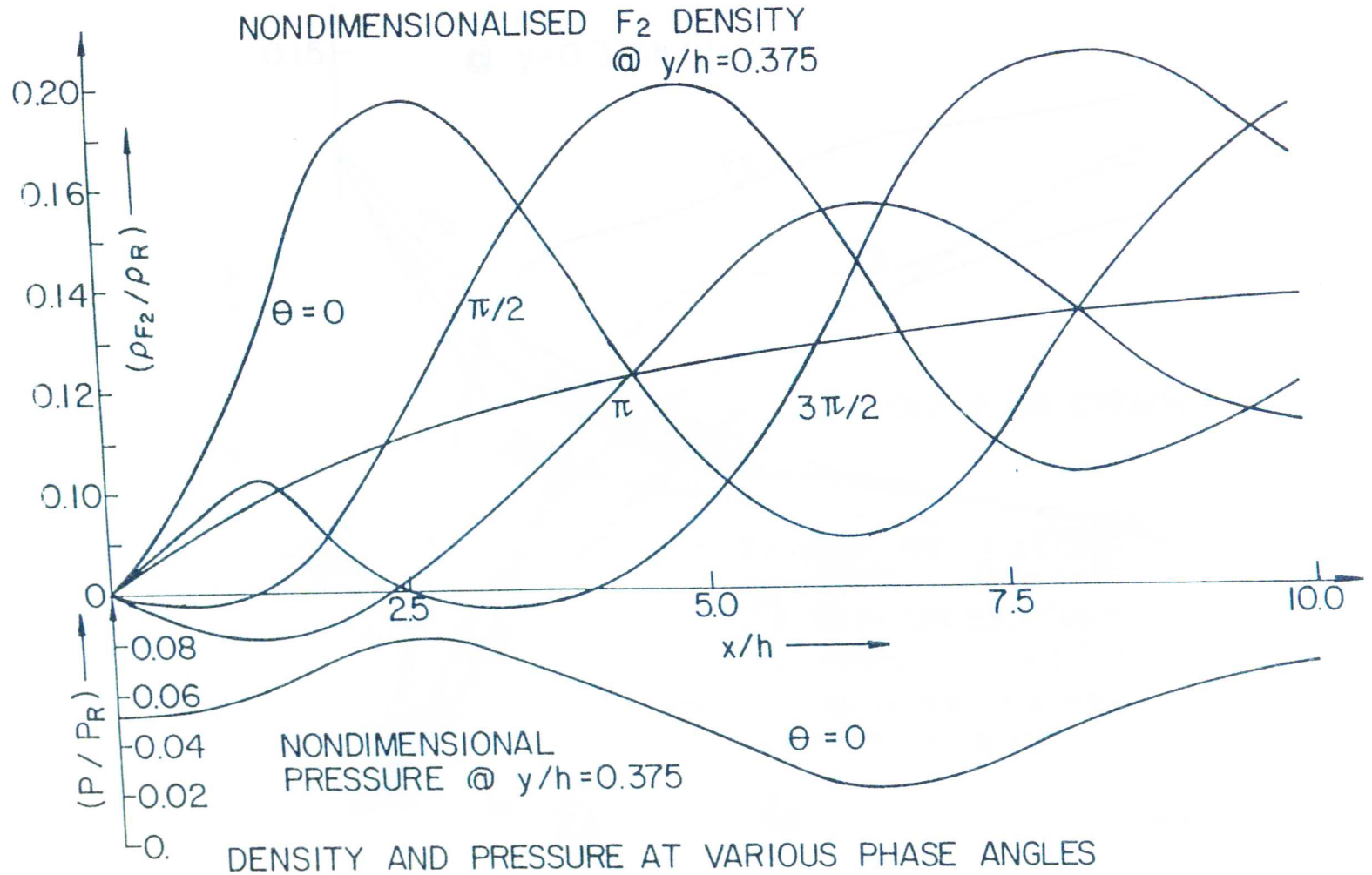


Fig. 49



NONDIMENSIONALISED F_2 DENSITY
@ $y/h=0.375$

(ρ_{F_2} / ρ_R)

$\theta = 0$

$\pi/2$

π

$3\pi/2$

x/h

(P / P_R)

NONDIMENSIONAL
PRESSURE @ $y/h=0.375$

$\theta = 0$

DENSITY AND PRESSURE AT VARIOUS PHASE ANGLES

$\omega = \pi \times 10^5$ RAD/SEC $\Delta u = \pm 25\%$

Fig. 50

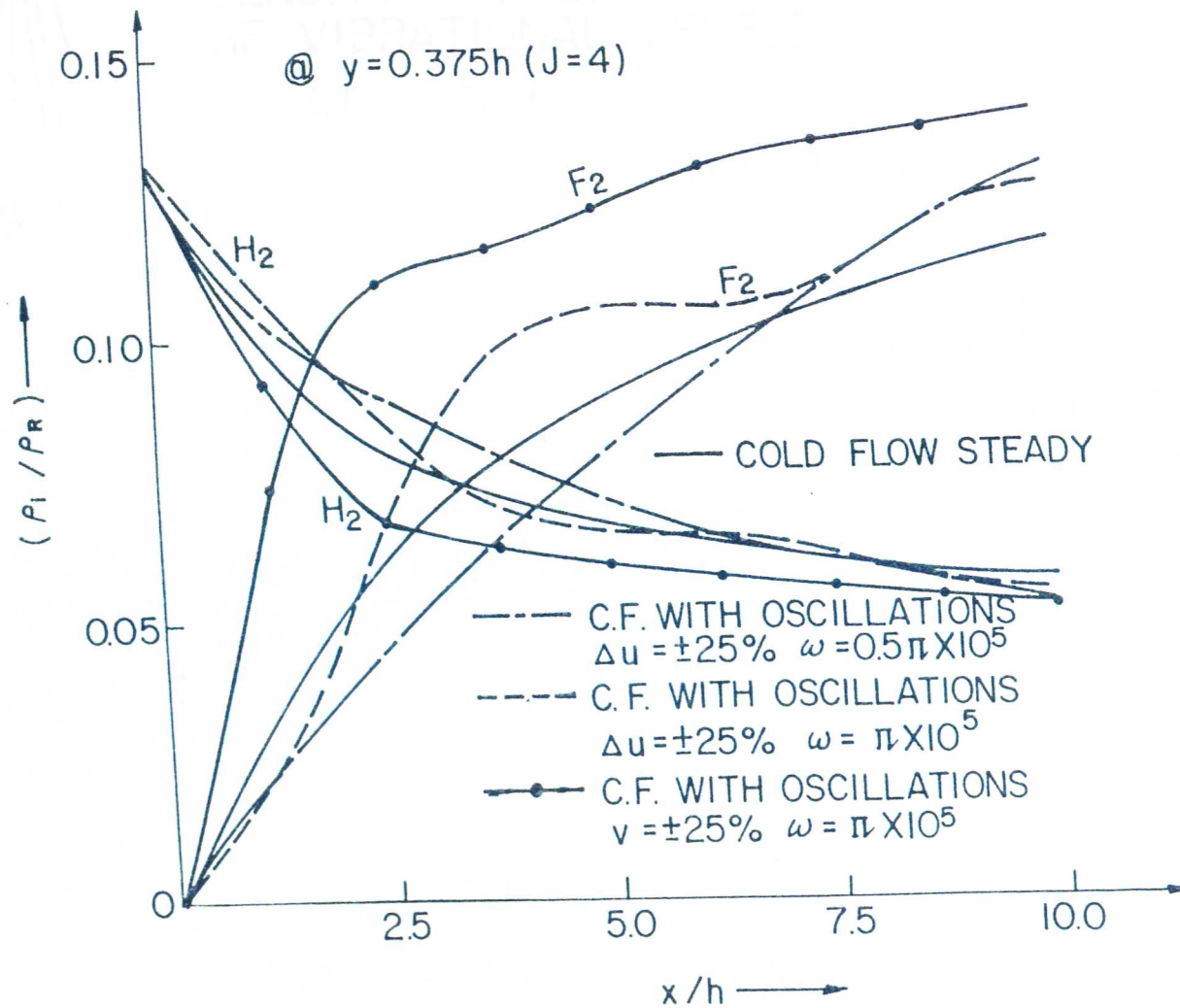


Fig. 51 -- Variations of species density in flow direction - comparison of steady and unsteady cases

Fig. 52

DENSITY PROFILES FOR VARIOUS
HF VIBRATIONAL LEVELS
AT $x/h = 5.0$

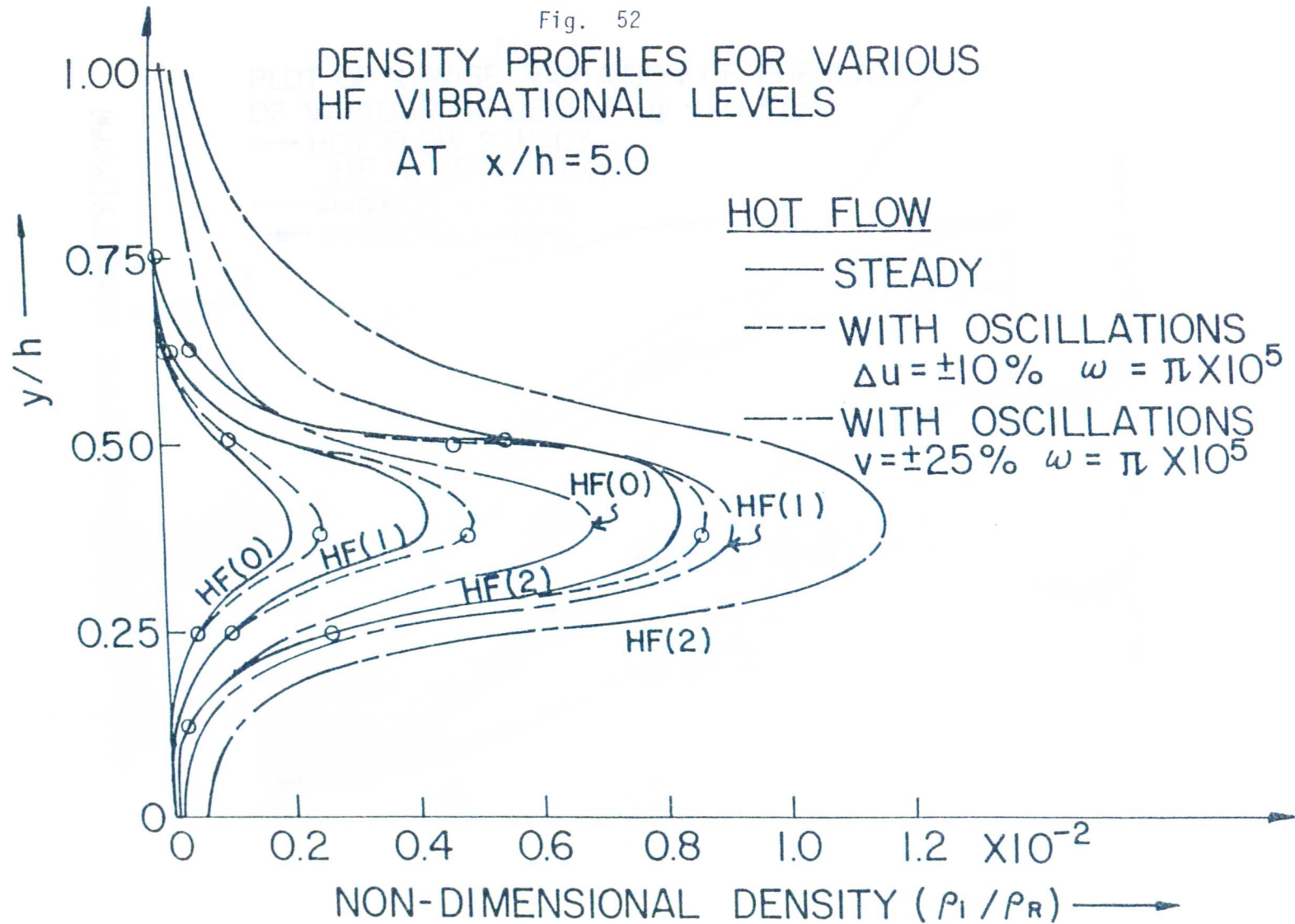


Fig. 53

PLOT OF X-WISE VARIATION OF POPULATIONS
OF VARIOUS HF LEVELS @ $y = 0.375h$

— HOT FLOW STEADY
HF W/ OSCILLATIONS

--- $\omega = \pi \times 10^5$, $v = 25\%$

● $\omega = \pi \times 10^5$, $\Delta u = \pm 10\%$

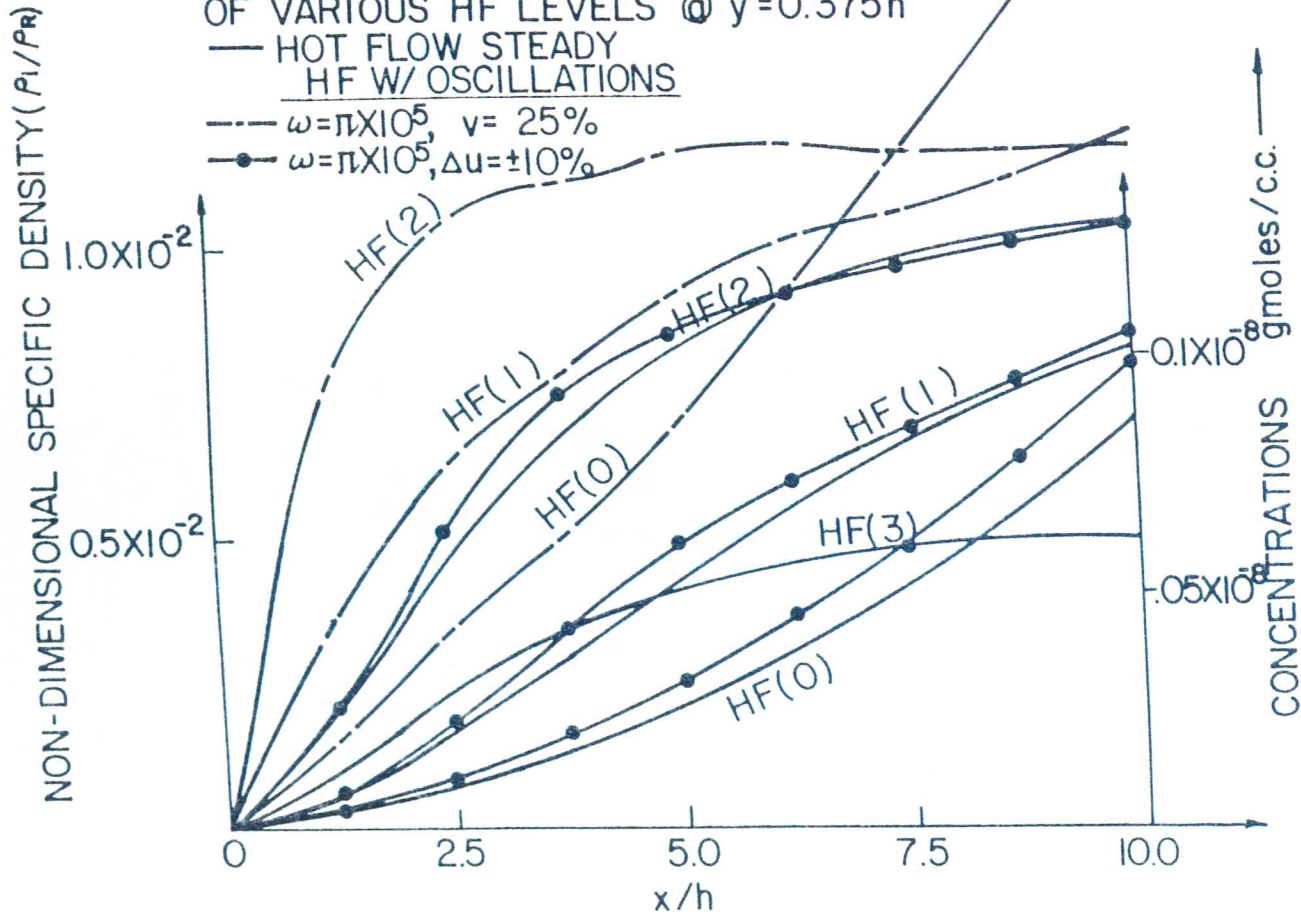


Fig. 55 -- F_2 density variation ρ $x/h = 10.0$ and $y/h = 0.375$ for sinusoidal fluctuations in v velocity

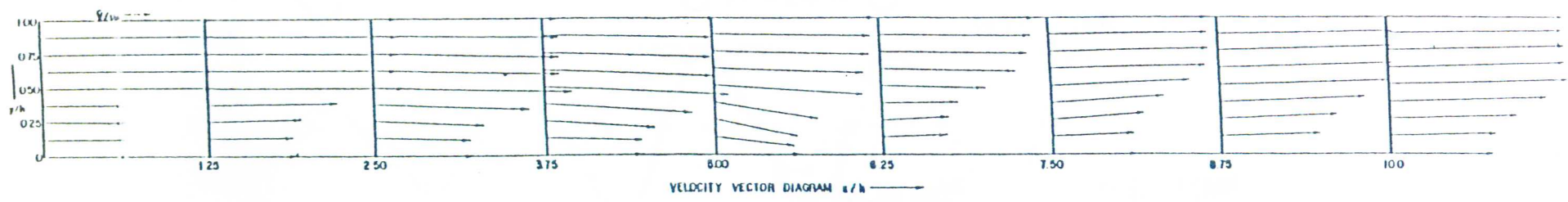


Fig. 54

u velocity fluctuations
 angular velocity $\omega = \pi \times 10^5$ rad/sec.
 amplitude $\Delta u = \pm 25\%$
 phase angle $\theta = 9^\circ$

147

Fig. 55 -- F_2 density variation @ $x/h = 10.0$ and $y/h = 0.375$ for sinusoidal fluctuations in v velocity

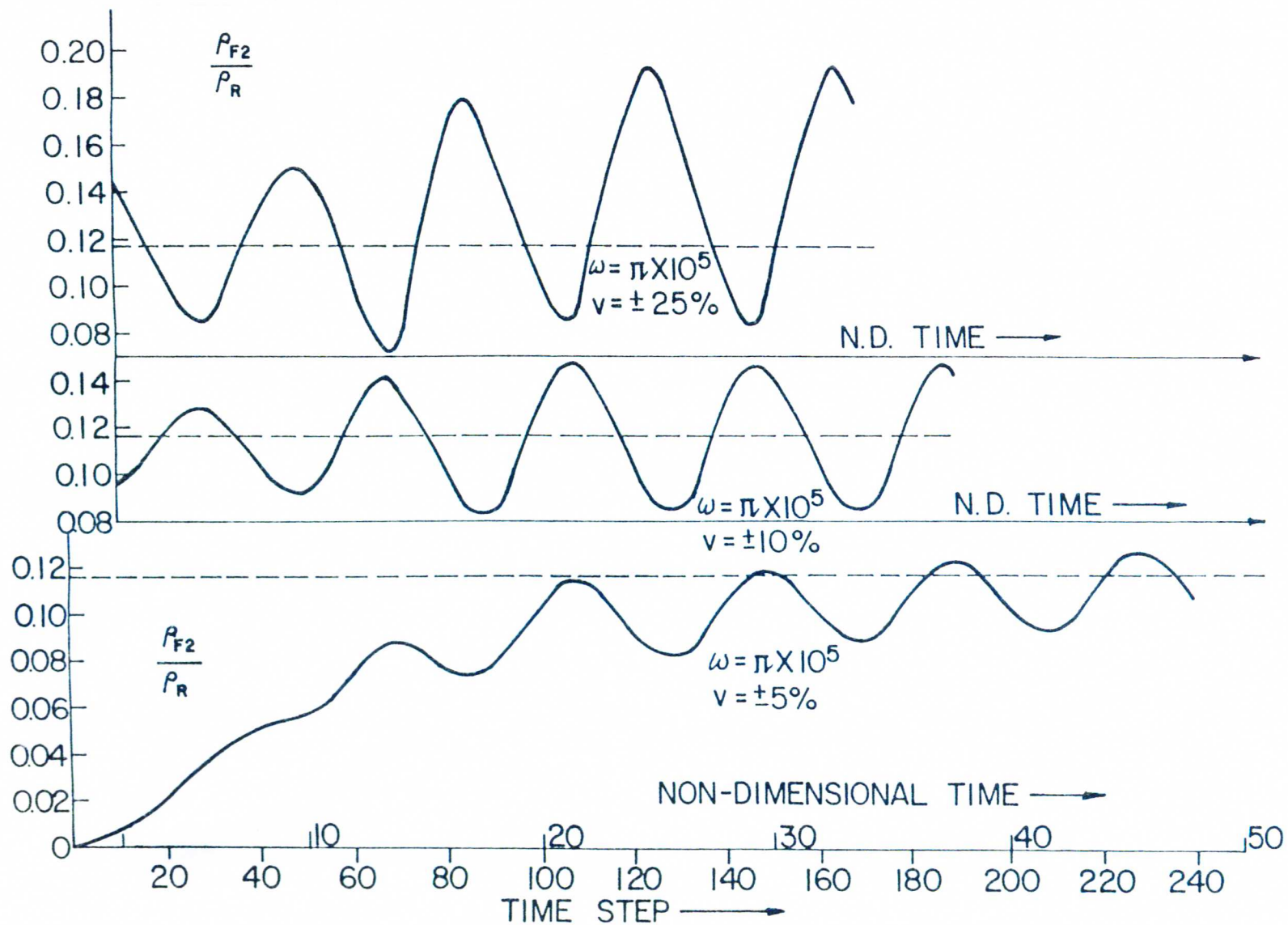
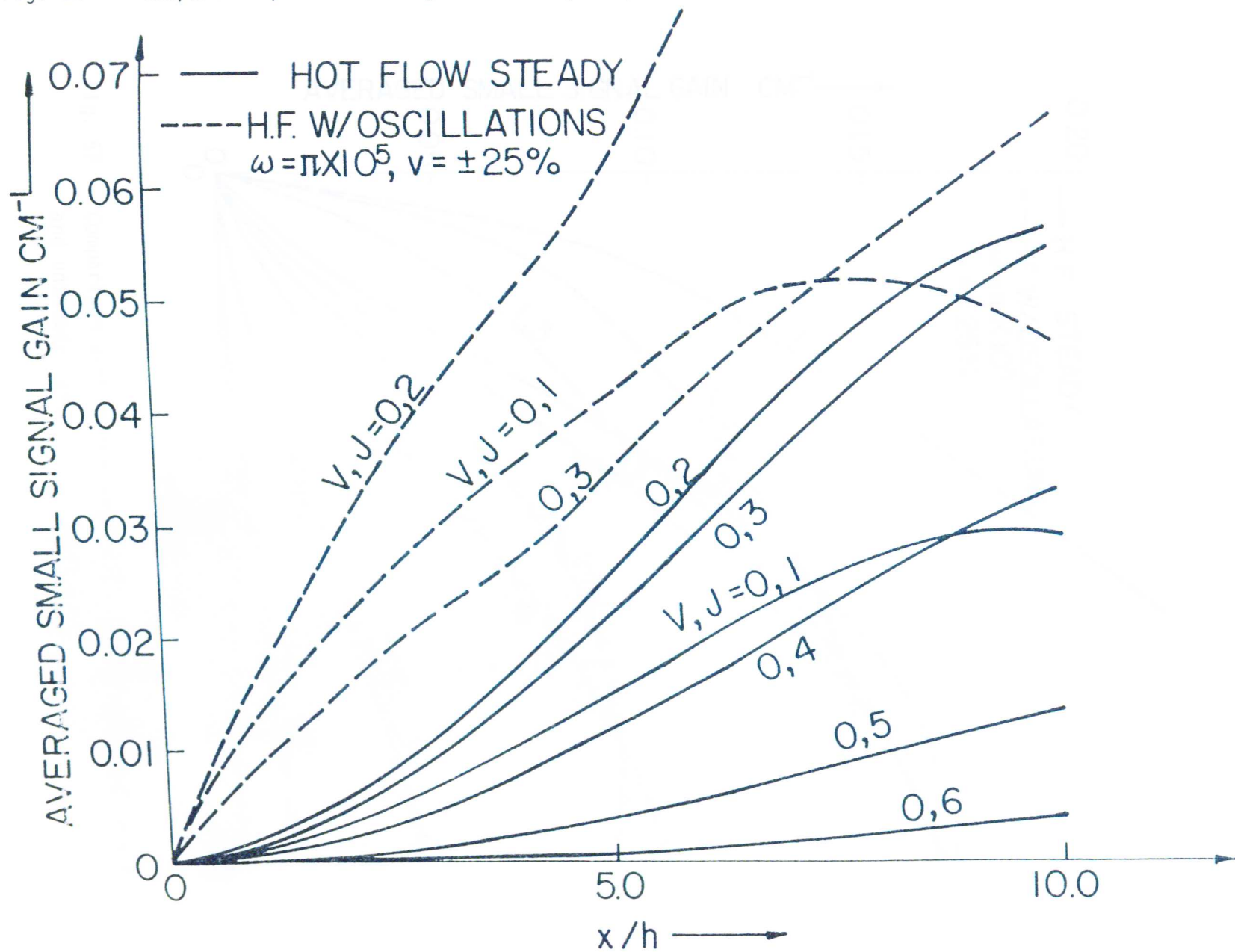


Fig. 56 -- Comparison plot of averaged small signal gains for steady and unsteady cases: 1 - 0 transition



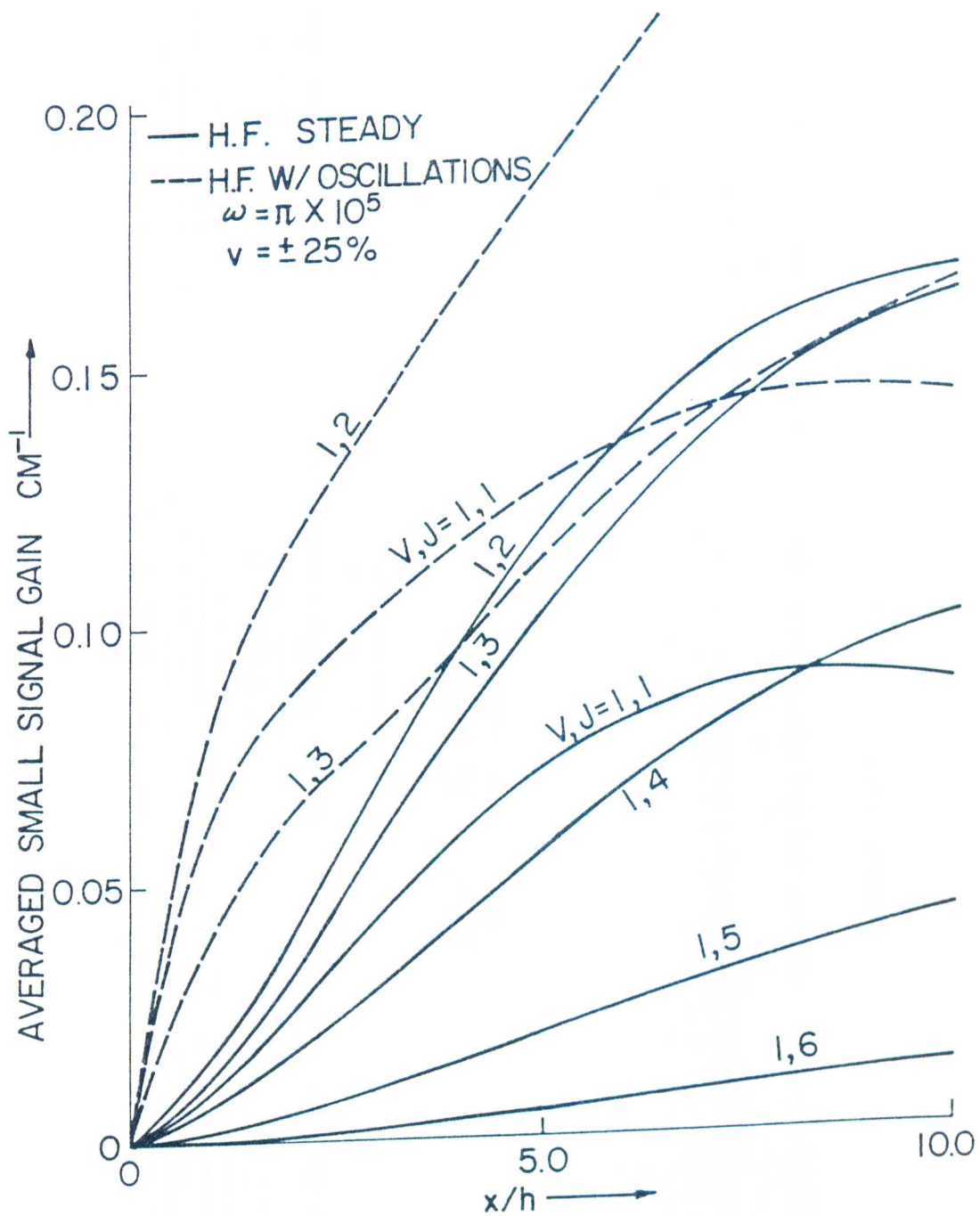
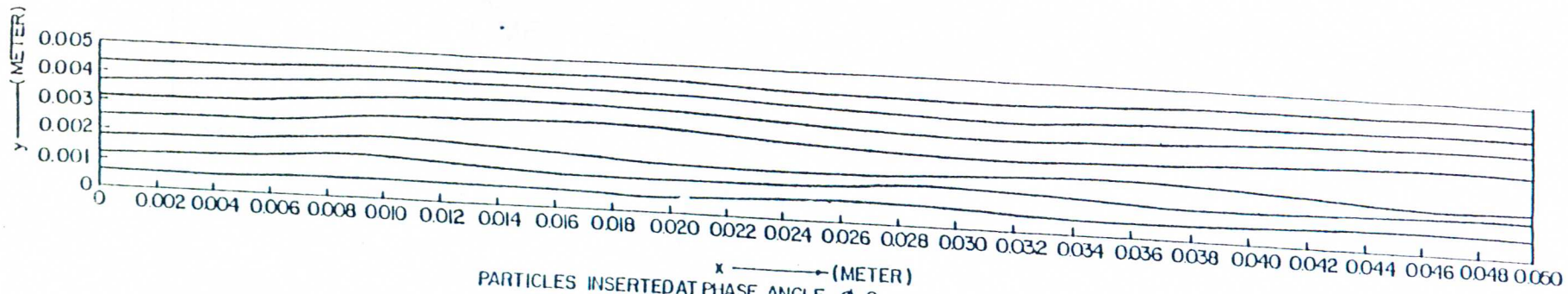


Fig. 57 -- Comparison plot of averaged small signal gains for steady and unsteady cases: 2-1 transition

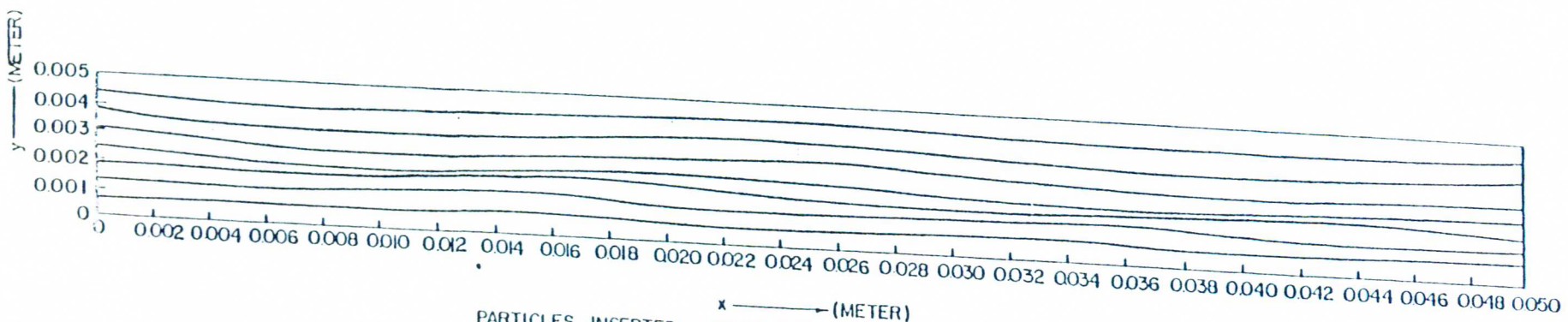


PARTICLES INSERTED AT PHASE ANGLE $\phi = 0$ or $v = 0$

(a)

PATHLINES OF INERT PARTICLES
 INSERTED AT INLET AFTER
 REPEATIVE STATE IS REACHED

Fig. 58



PARTICLES INSERTED
 PHASE ANGLE $\phi = \frac{\pi}{2}$ or $v = v_{MAX}$

(b)

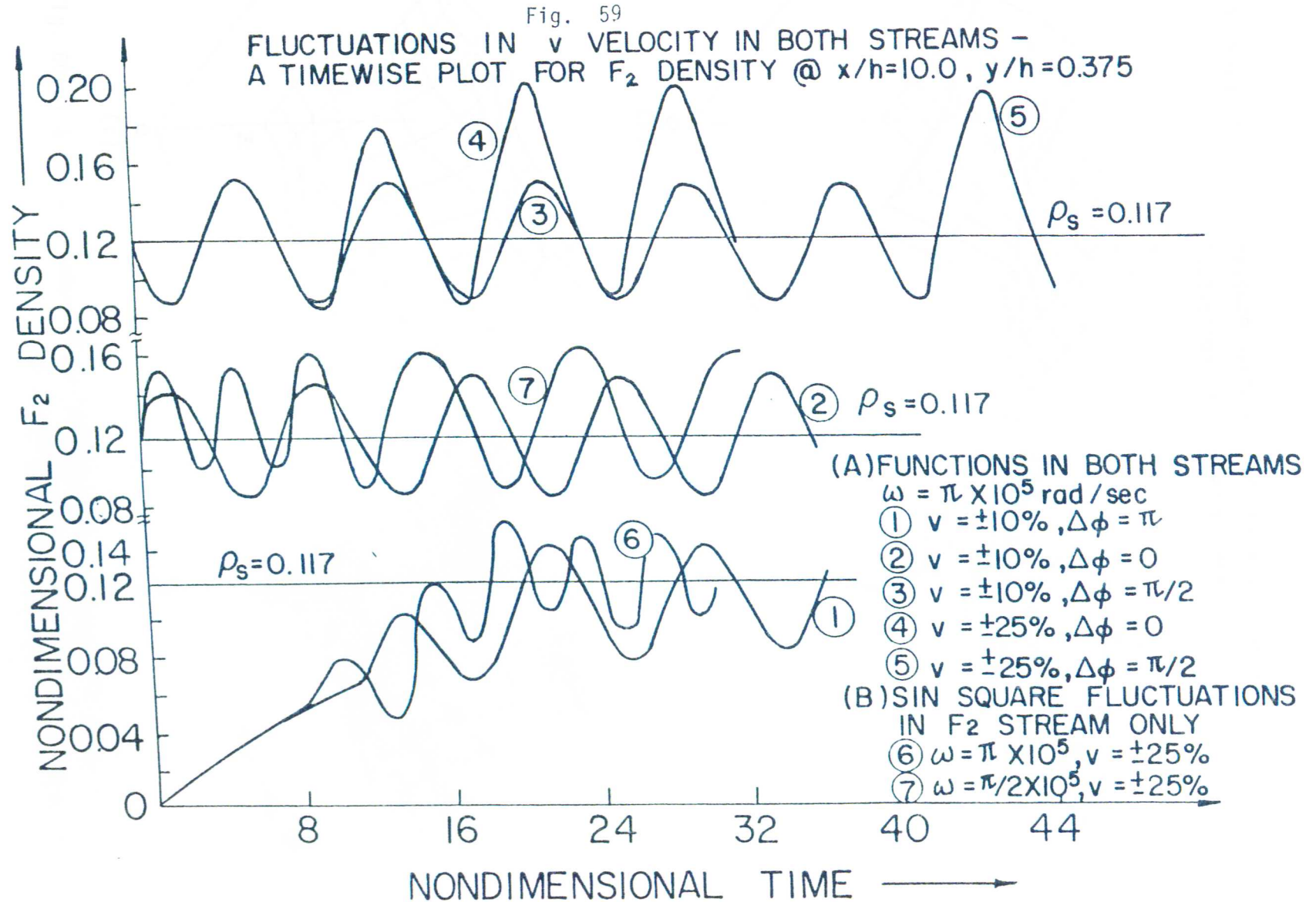


Fig. 60(a) & (b) -- Pressure surfaces for unsteady flow with v velocity fluctuations at different phase angles δ

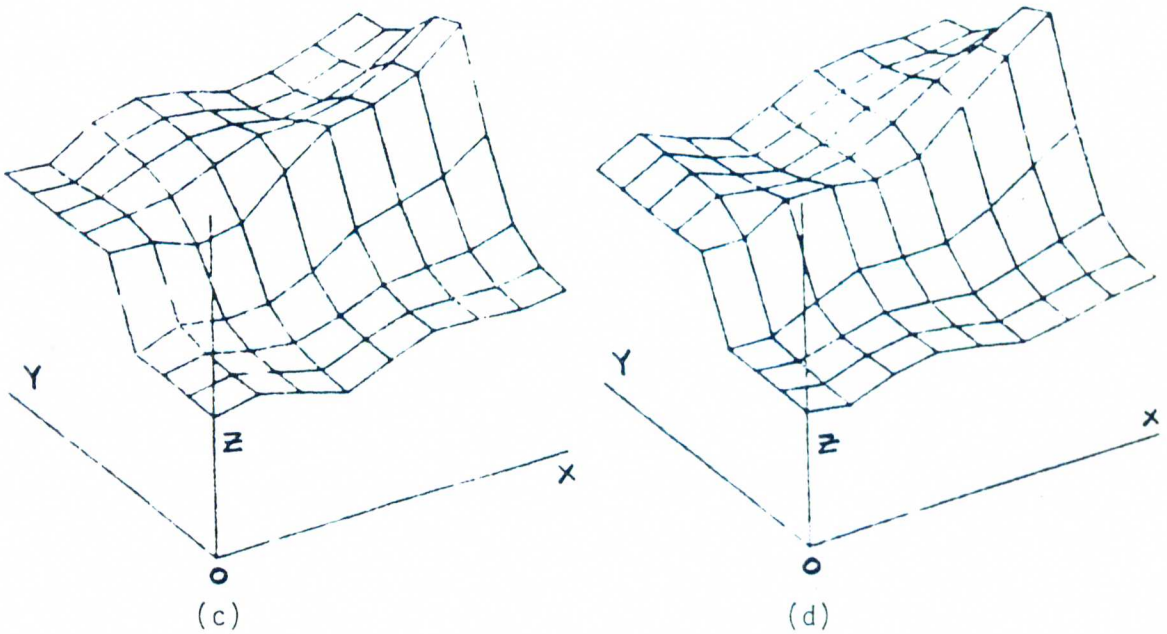
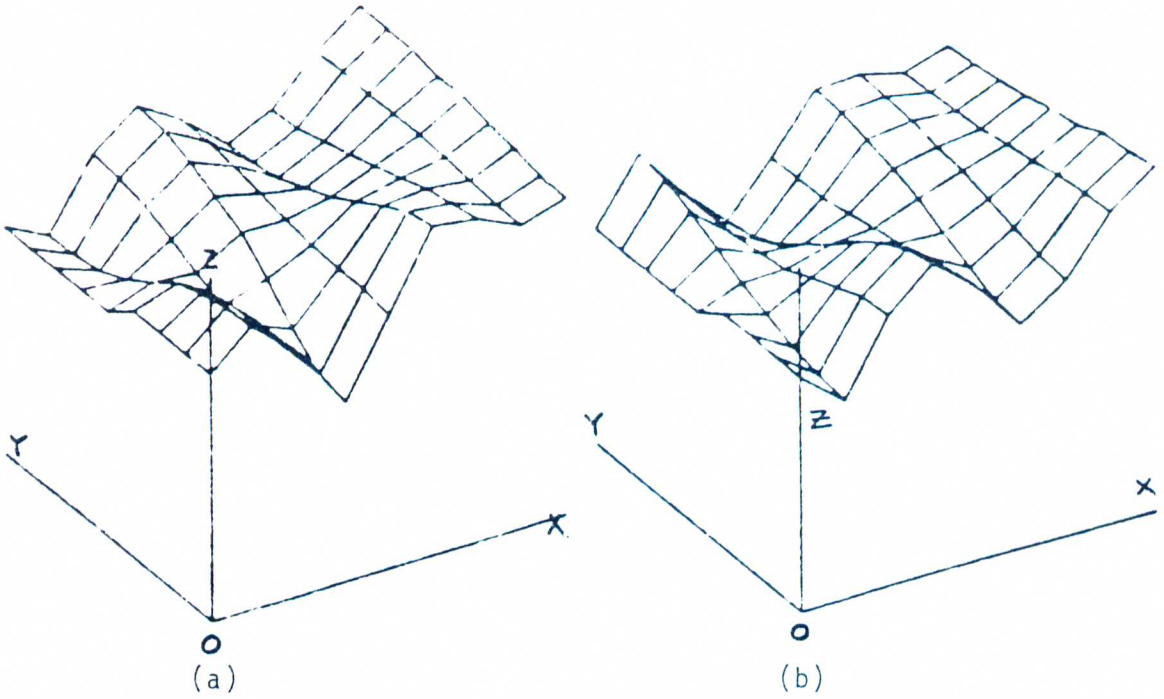


Fig. 60(c) & (d) -- Temperature surfaces for unsteady flow with v velocity fluctuations at different phase angles δ

Fig. 61(a) & (b) -- u velocity surfaces - plots at different phase angles δ of fluctuations

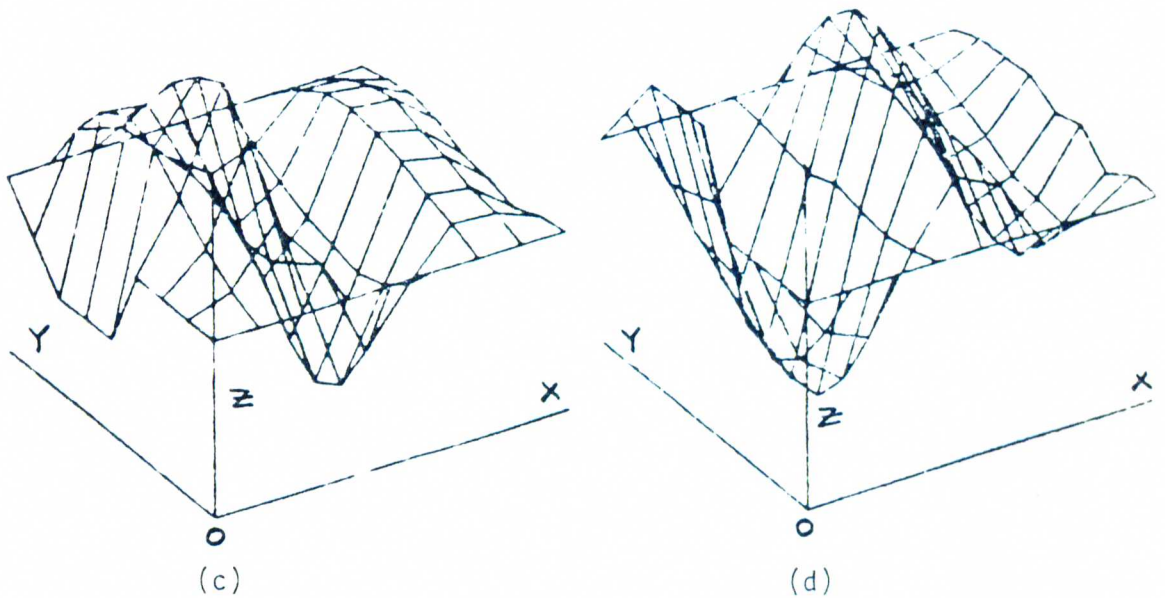
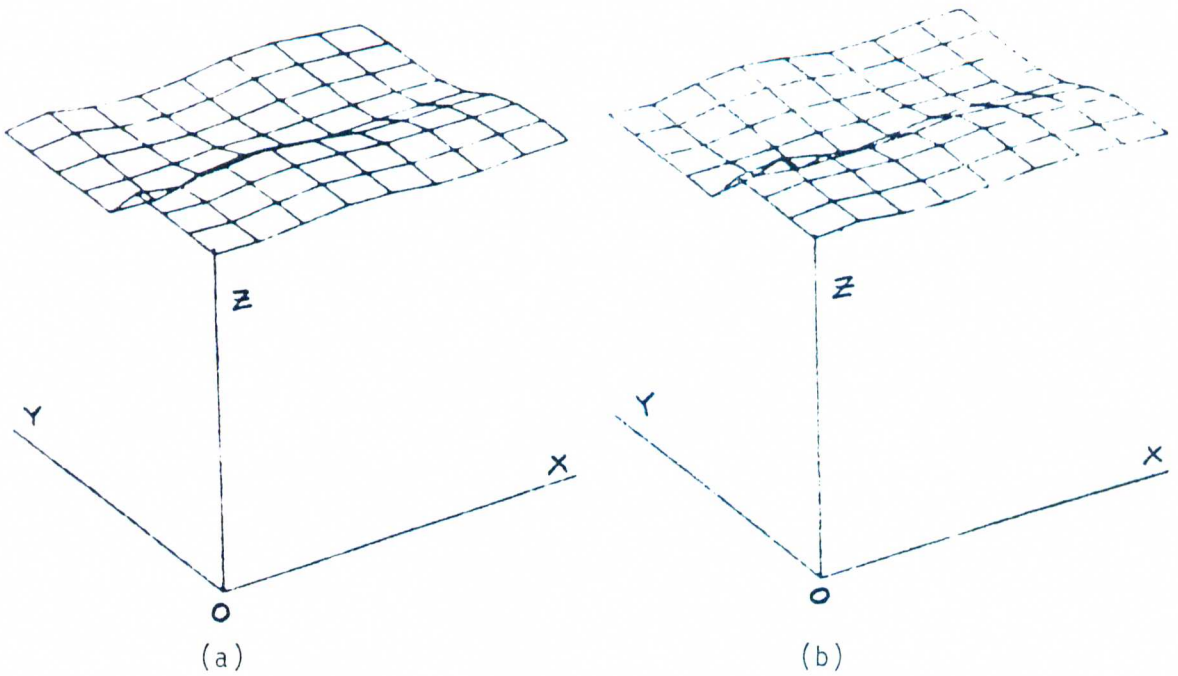
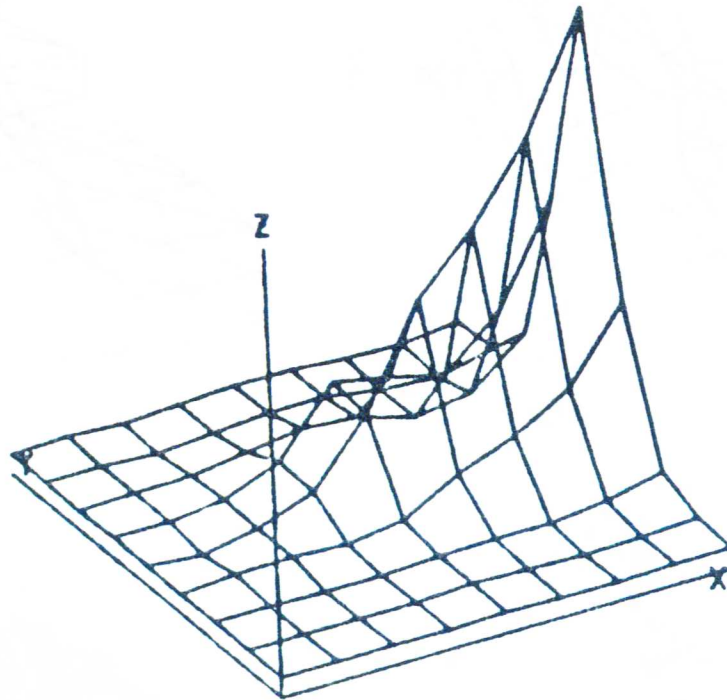


Fig. 61(c) & (d) -- v velocity surfaces - plots of different phase angles δ of fluctuations

Fig. 62 -- HF(0) density surface at the instant described by phase angle $\delta = 0^{\circ}$



VIEWING ANGLE
THETA = 60.0
PHI = 240.0
OPTIONS: A, U, S

DIMENSION
X: 1 STEP 1 UNTIL 9
Y: 1 STEP 1 UNTIL 9
Z: [.03
 .00]

REGION PLOTTED
1 STEP 1 UNTIL 9
1 STEP 1 UNTIL 9
[.03
, 0.00]

Fig. 63(a) & (b) -- HF(2) density surface at different phase angles

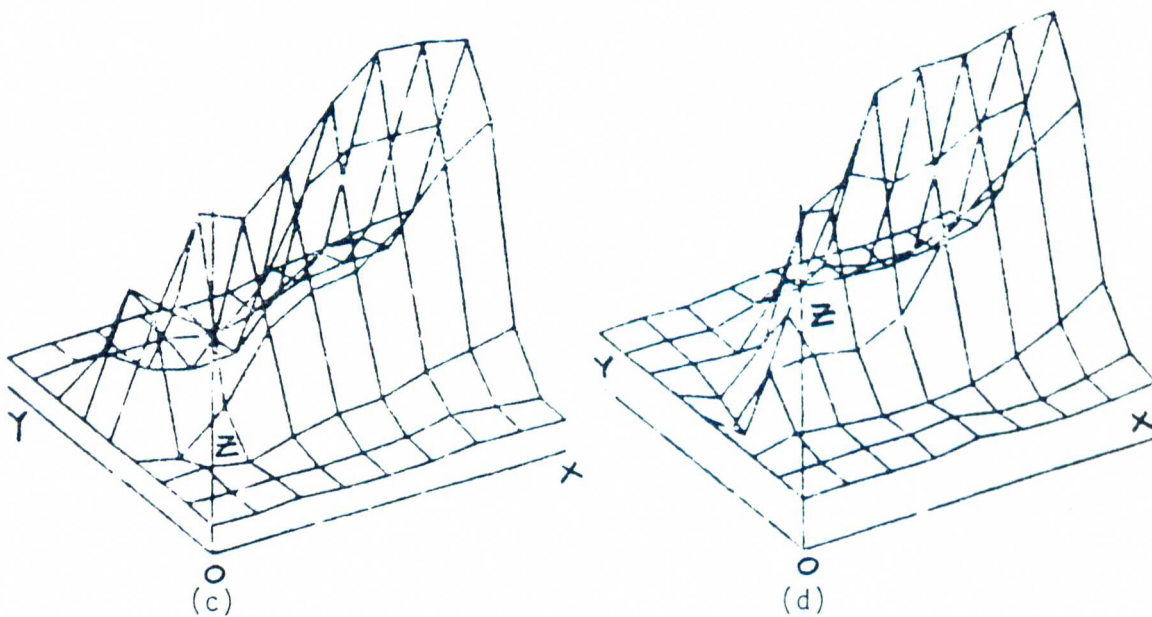
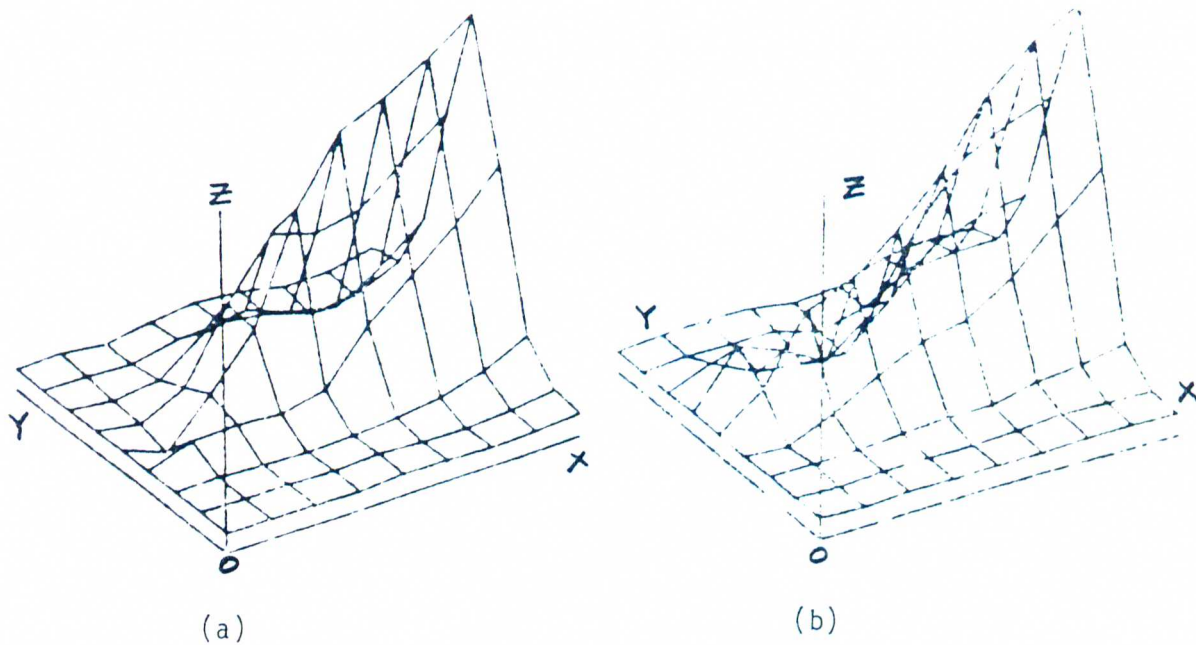


Fig. 63(c) & (d) -- HF(2) density surfaces at different phase angles

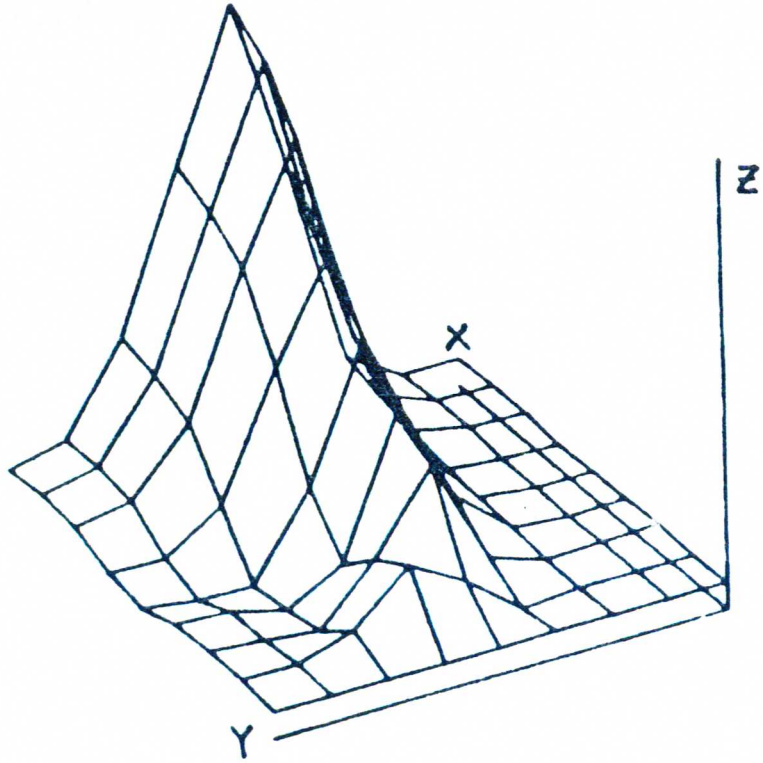
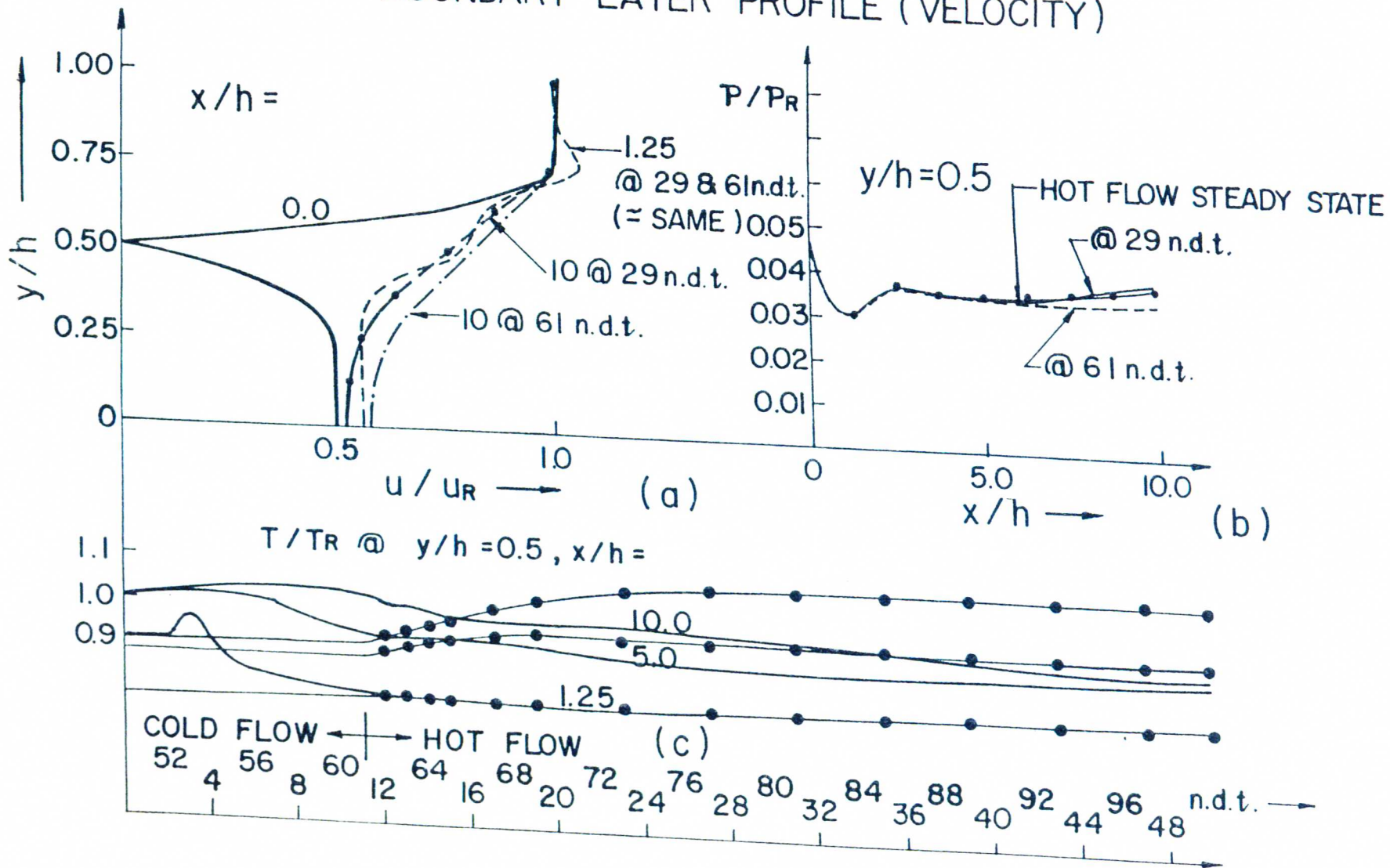


Fig. 64 -- HF(1) density surface for $\delta = 180^\circ$ as seen from a different viewing angle - $\theta = 60^\circ$ and $\phi = 150^\circ$

Fig. 65

BOUNDARY LAYER PROFILE (VELOCITY)



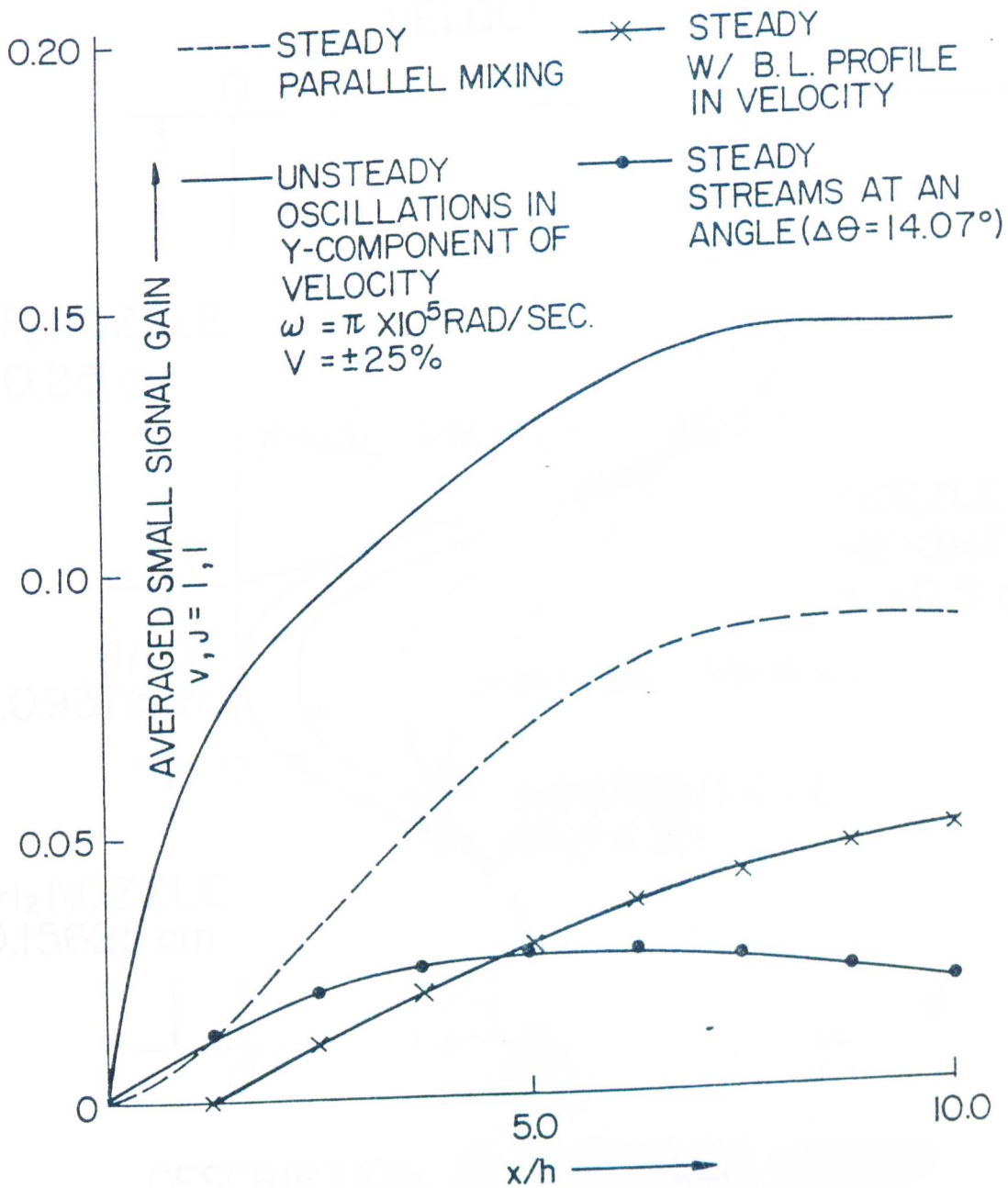
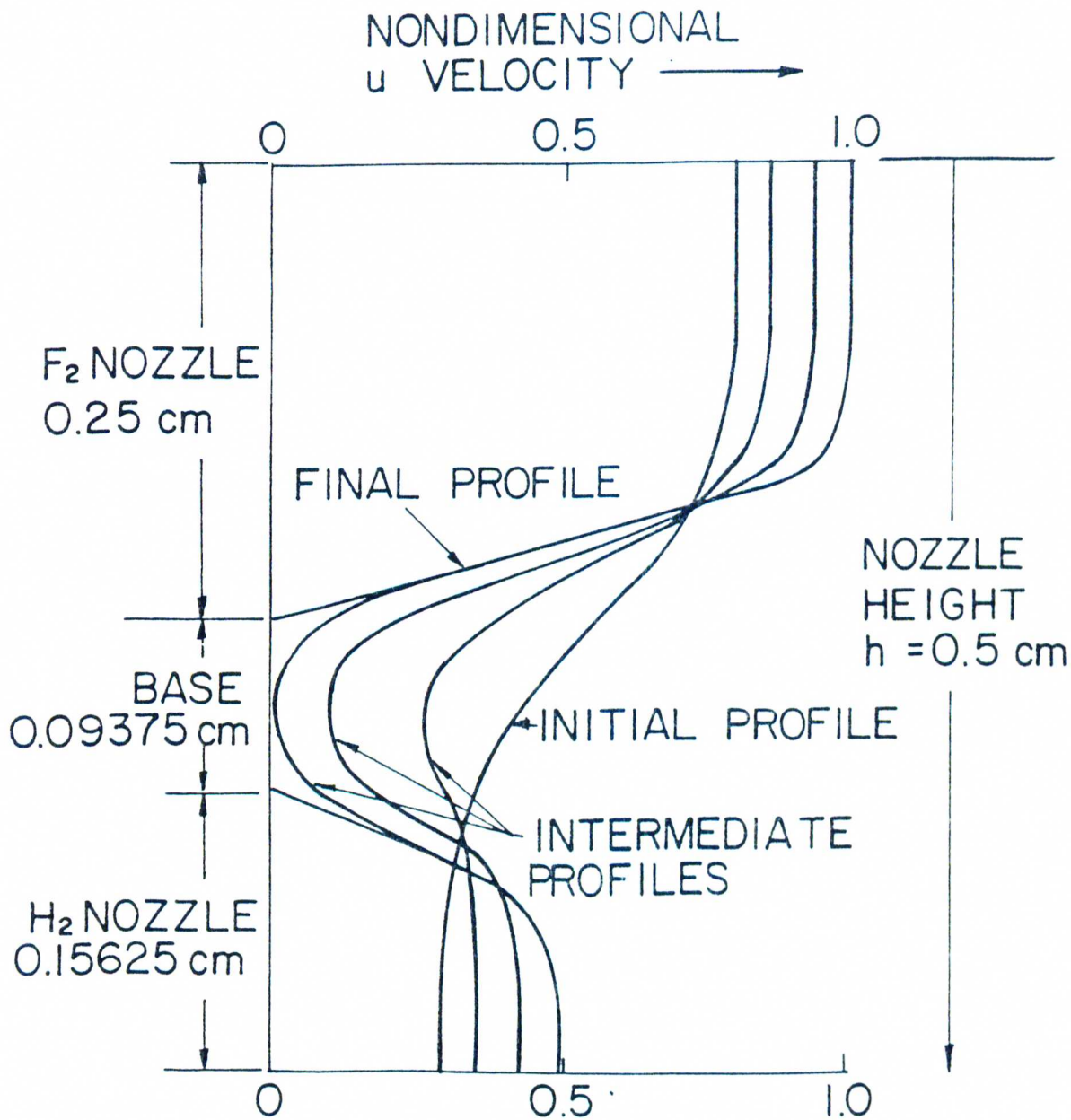


Fig. 66 -- Averaged small signal gain - a comparison plot



DESCRIPTION OF THE BASE REGION
AND SOME INLET PROFILES USED

Fig. 67

↑
PRESSURE
(NON-DIMENSIONAL)

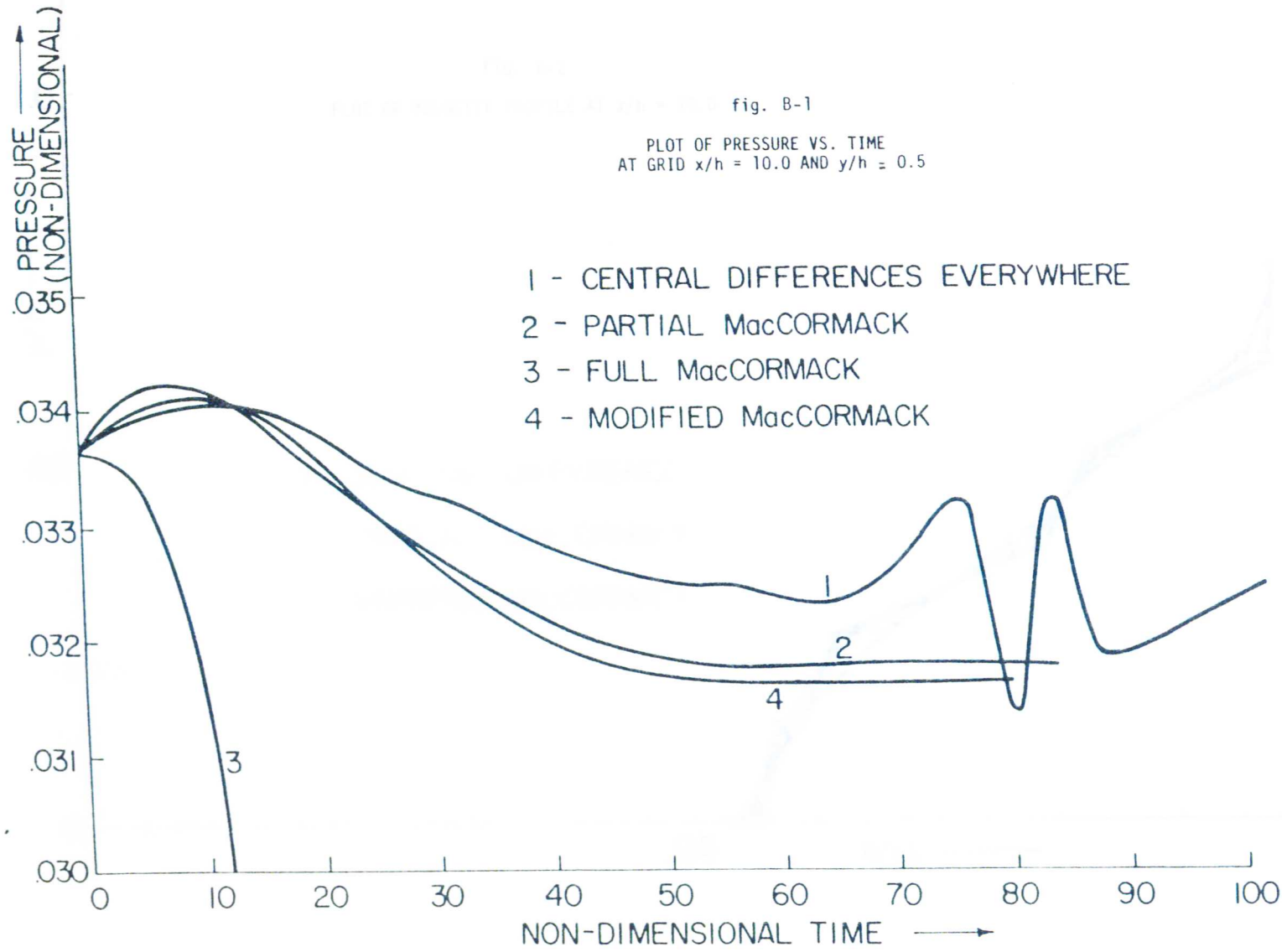
.035
034
033
032
031
030

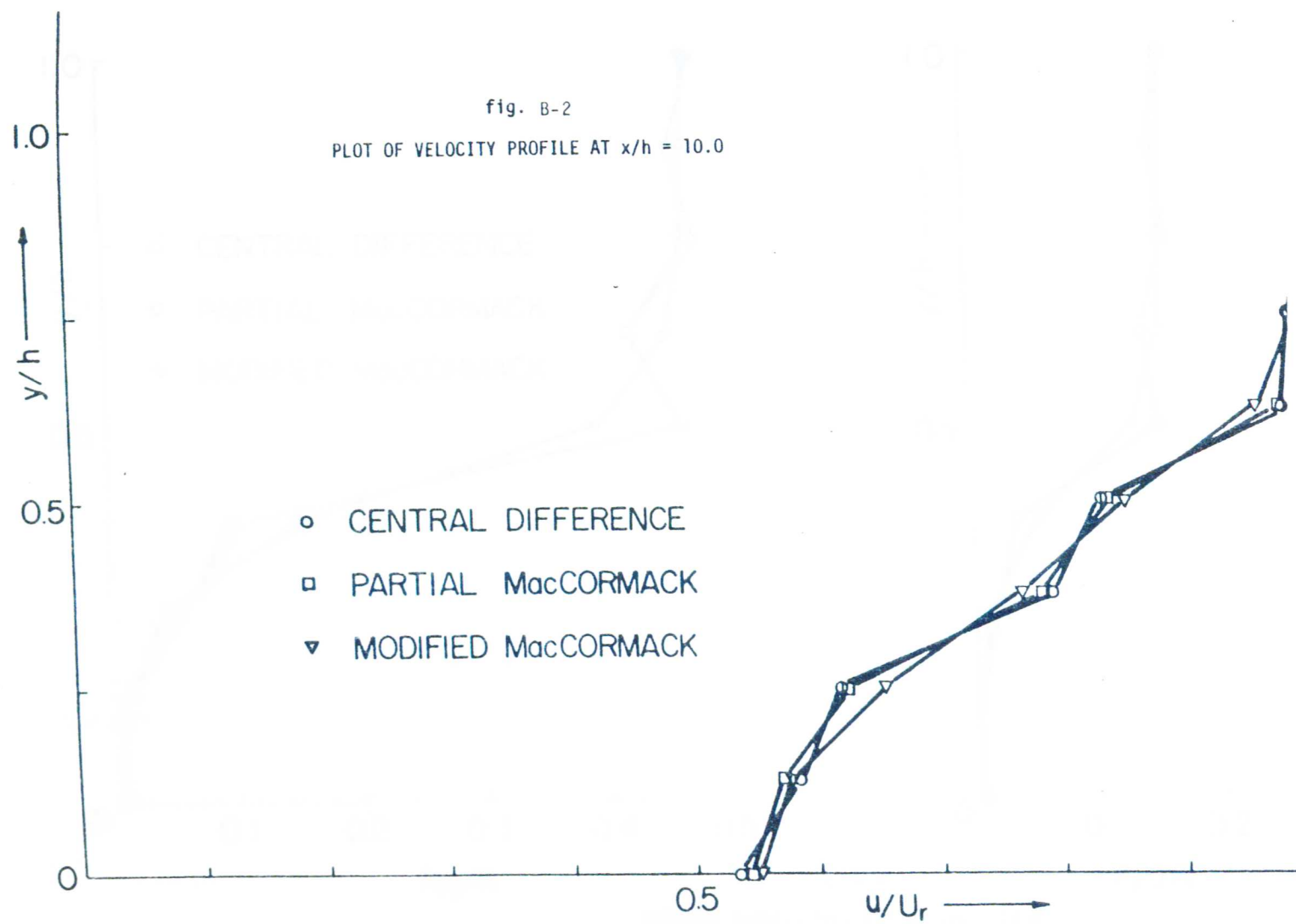
0 10 20 30 40 50 60 70 80 90 100

NON-DIMENSIONAL TIME →

- 1 - CENTRAL DIFFERENCES EVERYWHERE
- 2 - PARTIAL MacCORMACK
- 3 - FULL MacCORMACK
- 4 - MODIFIED MacCORMACK

fig. B-1
PLOT OF PRESSURE VS. TIME
AT GRID $x/h = 10.0$ AND $y/h = 0.5$





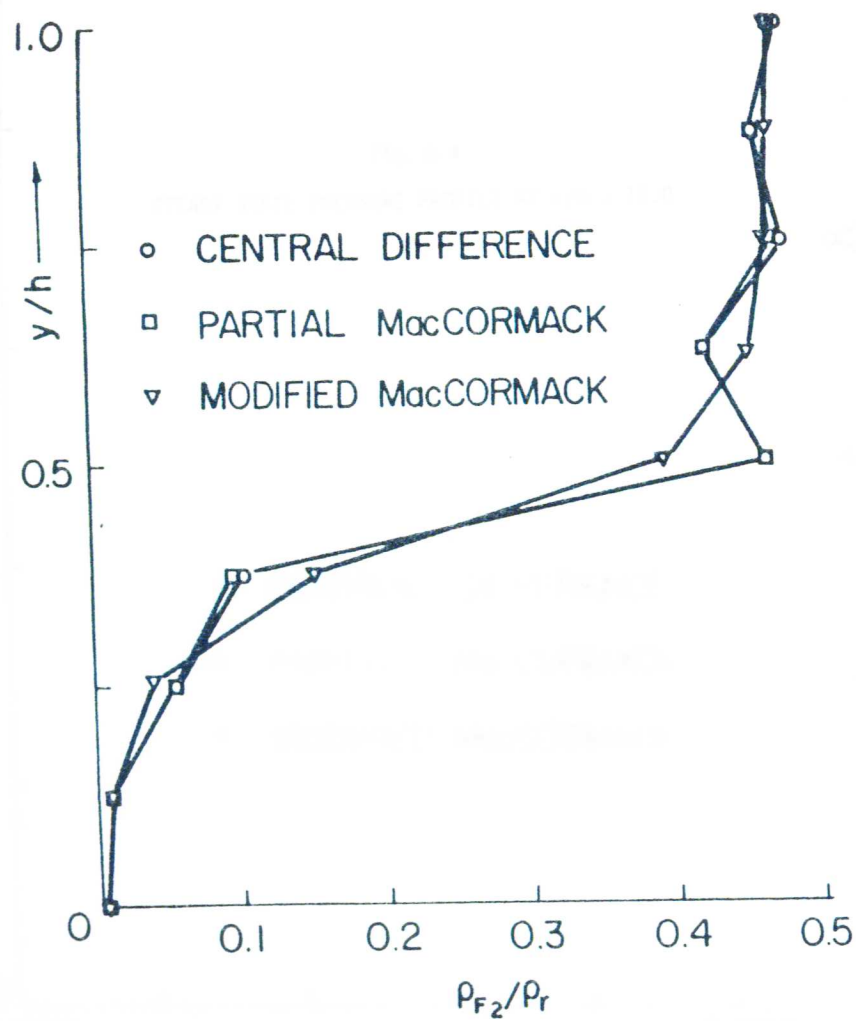
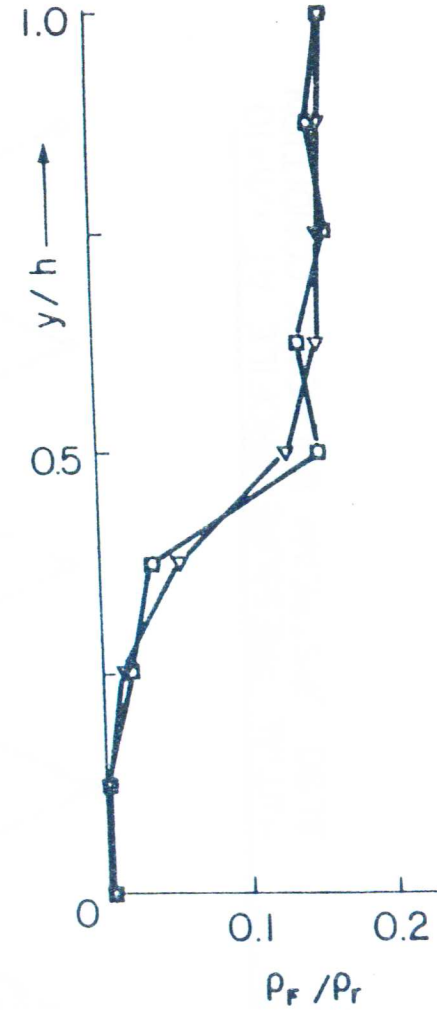
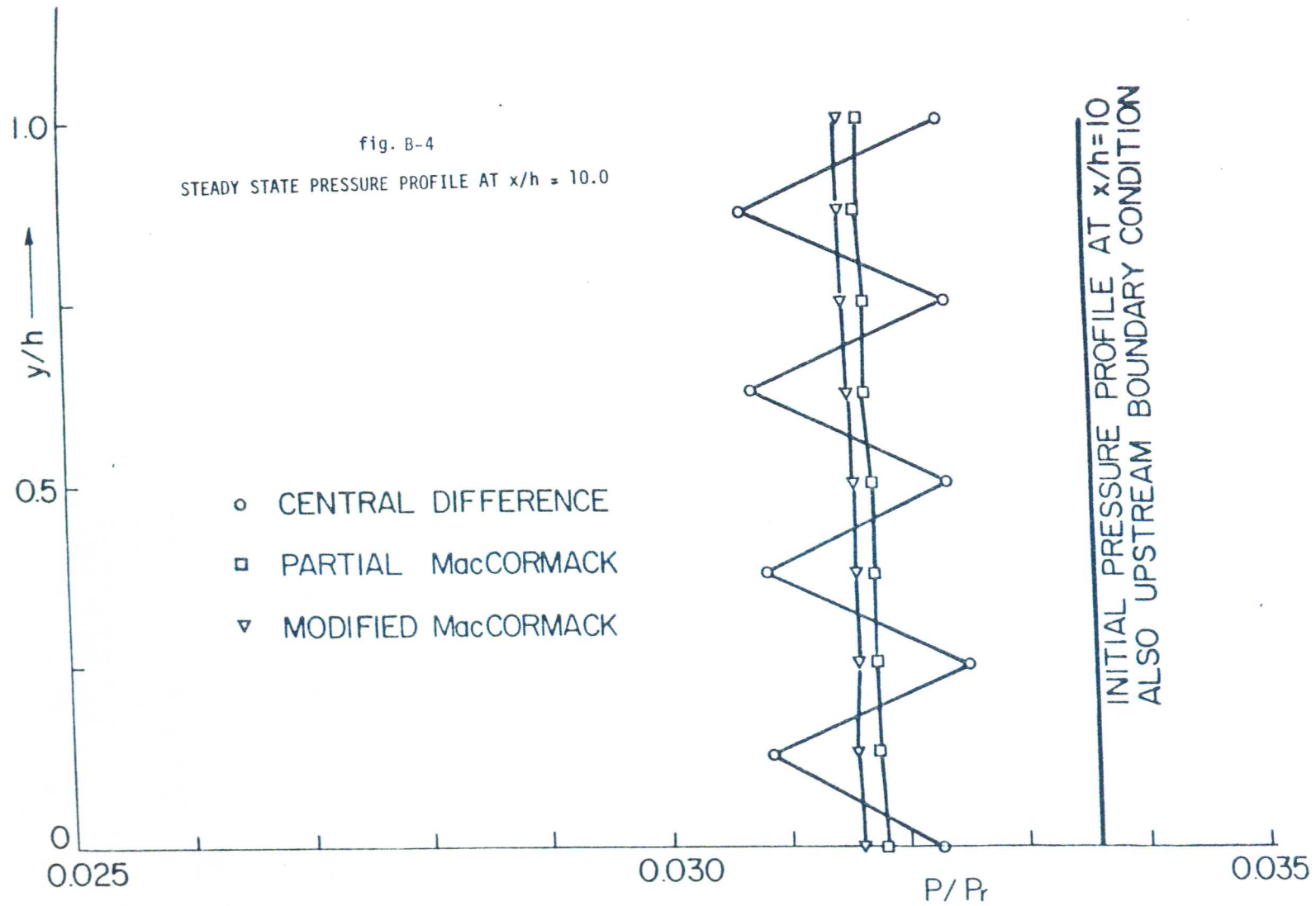


fig. B-3

SPECIFIC DENSITY PROFILES AT $x/h = 10.0$



CURRICULUM VITAE

Name: Ajay Prasannajit Kothari.

Permanent address: Nagin wadi, Idgah Road
Palanpur, Gujarat, India.

Degree and date to be conferred: Doctor of Philosophy, 1979.

Date of birth: November 22, 1949.

Place of birth: Dhanera, Gujarat, India.

Secondary education: Shri Vividhlakshi Vidyamandir,
Palanpur, Gujarat, India, May 1966.

Collegiate institutions attended	Dates	Degree	Date of Degree
M.S. University, Baroda	1966-67	Prep. Sc.	May 1967
St. Xavier's College, Ahmedabad	1967-68	F.Y. Sc.	May 1968
Wilson College, Bombay	1968-70	B. Sc.	May 1970
Univ. of Bombay, Bombay	1970-71	--	--
Univ. of Maryland, College Pk.	1971-73	(Special Student)	
Univ. of Maryland, College Pk.	1973-75	M.S.	August 1975
Univ. of Maryland, College Pk.	1975-79	Ph.D.	August 1979.

Major: Aerodynamics and Propulsion.

Minor(s): Physics, Mathematics.

Professional Publications:

Kothari, A. P. and Anderson, J. D., Jr., "Navier Stokes Solutions for Chemical Laser Flows," Technical Report AE75-6, Department of Aerospace Engineering, University of Maryland, June, 1975. Also AFOSR-TR-75-1447.

Kothari, A. P. and Anderson, J. D., Jr., "Navier-Stokes Solutions for Chemical Laser Flows: Cold Flows," AIAA Journal, Vol. 14, May 1976, pp. 702-703.

Kothari, A. P., Anderson, J. D., Jr., and Jones, E., "Navier Stokes Solutions for Chemical Laser Flows," AIAA Journal, Vol. 15, No. 1, Jan. 1977, pp. 92-100.

Kothari, A. P., Anderson, J. D., Jr., and Jones, E., "Navier Stokes Solutions for Chemical Laser Flows: Steady and Unsteady Flows," AIAA paper 79-0009, AIAA 17th Aerospace Sciences Meeting, January 1979, New Orleans, LA.

Professional positions held:

June 1974 to August 1979

Graduate Research Assistant, Department of Aerospace Engineering, University of Maryland, College Park, MD. 20742.

February 1973 to June 1974

Graduate Teaching Assistant, Department of Aerospace Engineering, University of Maryland, College Park, MD. 20742.